

https://dspace.org/

Numerical simulation of structural, electronic and optical properties of transition metal chalcogenides

Rugut, Elkana Kipkogei

2017

http://hdl.handle.net/10539/23602

Rugut, Elkana Kipkogei (2017) Numerical simulation of structural, electronic and optical properties of transition metal chalcogenides, University of the Witwatersrand, Johannesburg, <http://hdl.handle.net/10539/23602>

Downloaded from a DSpace repository. https://dspace.org/



NUMERICAL SIMULATION OF STRUCTURAL, ELECTRONIC AND OPTICAL PROPERTIES OF TRANSITION METAL CHALCOGENIDES

Presented by: Elkana Kipkogei Rugut
(1214396)

Supervised by: Prof Daniel Joubert
Dr Glenn Jones

A Dissertation submitted to the Faculty of Science
University of the Witwatersrand,
in partial fulfillment of the requirements for
the degree of master of science (Msc)
School of physics,
University of the Witwatersrand,

Johannesburg.

May 22, 2017

DECLARATION

This dissertation is my original work under supervision of Prof Daniel Joubert and Dr Glenn Jones and has not been presented for a degree in any other University. No part of this dissertation may be reproduced without prior written permission of the author and/or University of the Witwatersrand.



Elkana Kipkogei Rugut, 22^{nd} May 2017

ABSTRACT

Intensive study on structural, electronic and optical properties of bulk transition metal dichalcogenides and dipnictogenides (MX_2; where M = V, Nb and X = S, Se, Te, P) was undertaken. A relative stability test was done to determine the most stable ground state configuration via calculation of total ground state energy and volume which was fitted to the third order Birch-Murnaghan equation of state to extract lattice parameters. Cohesive energies of the above mentioned MX_2 compounds and their elemental solids were then computed from which formation energies were acquired based on their respective equations of reaction between reactants and product. Its significance was to aid in determining if a material is energetically stable.

Elastic constants were predicted from which mechanical properties i.e bulk, Young's and shear moduli and consequently Poisson's ratio were resolved by feeding the stiffness matrix onto online elastic tensor analysis tool which facilitated verification of their mechanical stability based on the well-known Born stability conditions which varies from one crystal system to another, at a later stage phonon dispersion curves were plotted after performing phonon calculation based on phonopy code to verify if the materials of concern are dynamically stable.

After a material had fulfilled all the above stability tests, its structural study was initiated using various functionals. Functional that described best the structural properties of each individual compound considered was then applied in exploring its electronic and optical properties whose motivation was to find out the most stable phase as well as gauge if these materials could be used in various fields that suits their mechanical and optical properties. Furthermore, from carefully calculated optical spectra, plasma frequencies were analyzed which indicated the possibility of applying a material in plasmonic related fields. In addition to above, other factors to be considered when selecting a given electrode material that are crucial for optoelectronics are good chemical and thermal stabilities, high transparency and excellent conductivity.

Dedication

I dedicate this work to my family

ACKNOWLEDGEMENTS

I thank God for gift of life and granting me sound health throughout the entire period of research. I am grateful to my loving parents, brothers and sisters for their overwhelming support and prayers. I wish to thank uncle Chris and his family for moral support. This study wouldn't have been complete without invaluable assistance of my supervisors. I owe my sincere thanks to Prof Daniel Joubert and Dr Glenn Jones for their immeasurable input and proffessional assistance. I won't forget to acknowledge my former supervisor Dr Kingsley Onyebuchi for his helpful ideas during initial stages of my research.

I am obliged to my mentors Prof George Amolo, Prof Nicholas Makau and Dr George Manyali for equipping me with basic concepts that laid a strong foundation not only in this study but making me a whole rounded person. I am grateful to Johnson Matthey for financial support under contract number JM6473 and the Centre for High Performance Computing for computational resources during the entire period of research. I do also appreciate my colleaques Mahmud, Moise, Kossi, Peter, Mirriam, Mahmoud, Esther, Ibrahim and Patrick for their insightful comments.

Contents

1 INTRODUCTION **1**
- 1.1 Chalcogenides . . . 2
- 1.2 Composition, structure and stacking of TMDs . . . 3

2 REVIEW OF TMDs **4**
- 2.1 Transition metal dipnictogenides . . . 4
- 2.2 Transition metal dichalcogenides . . . 5

3 THEORETICAL FRAMEWORK **8**
- 3.1 Density Functional Theory (DFT) . . . 8
- 3.2 Hohenberg-Kohn theorem . . . 9
- 3.3 Kohn-Sham equations . . . 10
- 3.4 Density functional theory methods . . . 12
- 3.5 Total exchange-correlation energy functionals . . . 13
- 3.6 Van der Waals interaction . . . 15
- 3.7 Many Body Perturbation Theory (MBPT) . . . 16
- 3.8 Green function and self-energy . . . 18
- 3.9 Polarizability and response function . . . 21
- 3.10 Hedin's equations . . . 22
- 3.11 GW approximation . . . 22
- 3.12 Bethe Salpeter Equation (BSE) . . . 23
- 3.13 Relationship between absorption coefficient and dielectric function of a material . . . 24
- 3.14 Microscopic frequency dependent dielectric function . . . 25
- 3.15 Optical transitions . . . 26
- 3.16 Plasmonic materials . . . 29

4 COMPUTATIONAL DETAILS **31**
- 4.1 Outline of calculation . . . 31
- 4.2 Work flow . . . 32
- 4.3 Convergence test . . . 34
- 4.4 Equation of state . . . 35
- 4.5 Phonons . . . 37
- 4.6 Cohesive and formation energy . . . 38
- 4.7 Ab initio calculation of elastic constants . . . 38
- 4.8 Optical constants . . . 39

5 RESULTS AND DISCUSSION **41**

5.1 Niobium diphosphide . . . 41
5.2 Vanadium diphosphide . . . 46
5.3 Vanadium diselenide (VSe_2) . . . 50
5.4 Vanadium disulphide (VS_2) . . . 56
5.5 Vanadium ditelluride (VTe_2) . . . 62
5.6 Niobium ditelluride ($NbTe_2$) . . . 67
5.7 Niobium disulphide . . . 73
5.8 Niobium diselenide . . . 80
5.9 Summary . . . 84

6 Conclusion and Future work **85**
6.1 Conclusion . . . 85
6.2 Future work . . . 85

References **101**

List of Figures

3.1 Convergence of the Drude plasma frequency squared of VSe_2 with respect to k-points at DFT level for both in-plane and out-of-plane . . . 27
3.2 Real part of dielectric function of VSe_2 at DFT . . . 28
3.3 Imaginary part of dielectric function of VSe_2 at DFT . . . 28
3.4 Real part of dielectric function of VSe_2 at BSE . . . 28
3.5 Imaginary part of dielectric function of VSe_2 at BSE . . . 28

4.1 Work flow . . . 33
4.2 An example of BZ . . . 34
4.3 cut-off energy convergence for trigonal VS_2 . . . 35

5.1 NbP_2 . . . 41
5.2 Ductile vs Brittle . . . 43
5.3 NbP_2 electronic Bands . . . 44
5.4 Electronic DOS . . . 44
5.5 NbP_2 phonon Bands . . . 44
5.6 Phonon DOS . . . 44
5.7 NbP_2 absorption coefficient . . . 45
5.8 NbP_2 reflectivity . . . 45
5.9 NbP_2 refractive index . . . 45
5.10 NbP_2 extinction coefficient . . . 45
5.11 Absorption coefficient within the visible range . . . 45
5.12 Reflectivity within the visible range . . . 45
5.13 Real part of dielectric function . . . 46
5.14 3D directional Young's modulus . . . 47
5.15 VP_2 electronic Bands . . . 48
5.16 Electronic DOS . . . 48
5.17 VP_2 phonon Bands . . . 48
5.18 Phonon DOS . . . 48
5.19 VP_2 absorption coefficient . . . 48
5.20 VP_2 reflectivity . . . 48
5.21 VP_2 refractive index . . . 49
5.22 VP_2 extinction coefficient . . . 49
5.23 Absorption coefficient within the visible range . . . 49
5.24 Reflectivity within the visible range . . . 49
5.25 Real part of dielectric function . . . 49
5.26 PBE+D2 . . . 50
5.27 PBE . . . 50

5.28 PBE+TS . . . 51
5.29 VSe_2 . . . 51
5.30 VSe_2 electronic Bands . . . 53
5.31 Electronic DOS . . . 53
5.32 VSe_2 phonon Bands . . . 53
5.33 Phonon DOS . . . 53
5.34 VSe_2 absorption coefficient . . . 54
5.35 VSe_2 reflectivity . . . 54
5.36 VSe_2 refractive index . . . 54
5.37 VSe_2 extinction coefficient . . . 54
5.38 Absorption coefficient within the visible range . . . 54
5.39 Reflectivity within the visible range . . . 54
5.40 Real part of dielectric function . . . 55
5.41 Relative stability . . . 56
5.42 Phase diagram . . . 57
5.43 PBE+D2 . . . 57
5.44 PBE . . . 57
5.45 PBE+TS . . . 58
5.46 VS_2 electronic Bands . . . 60
5.47 Electronic DOS . . . 60
5.48 VS_2 phonon Bands . . . 60
5.49 Phonon DOS . . . 60
5.50 VS_2 absorption coefficient . . . 60
5.51 VS_2 reflectivity . . . 60
5.52 VS_2 refractive index . . . 61
5.53 VS_2 extinction coefficient . . . 61
5.54 Absorption coefficient within the visible range . . . 61
5.55 Reflectivity within the visible range . . . 61
5.56 Real part of dielectric function . . . 61
5.57 Trigonal . . . 62
5.58 Monoclinic . . . 62
5.59 PBE+D2 . . . 63
5.60 PBE . . . 63
5.61 PBE+TS . . . 63
5.62 PBEsol . . . 63
5.63 VTe_2 electronic Bands . . . 65
5.64 Electronic DOS . . . 65
5.65 VTe_2 phonon Bands . . . 65
5.66 Phonon DOS . . . 65
5.67 VTe_2 absorption coefficient . . . 66
5.68 VTe_2 reflectivity . . . 66
5.69 VTe_2 refractive index . . . 66
5.70 VTe_2 extinction coefficient . . . 66
5.71 Absorption coefficient within the visible range . . . 66
5.72 Reflectivity within the visible range . . . 66
5.73 Real part of dielectric function . . . 67
5.74 PBE+D2 . . . 68
5.75 PBE . . . 68

5.76 PBE+TS . . . 68
5.77 PBEsol . . . 68
5.78 $NbTe_2$ electronic Bands . . . 70
5.79 Electronic DOS . . . 70
5.80 $NbTe_2$ phonon Bands . . . 70
5.81 Phonon DOS . . . 70
5.82 $NbTe_2$ absorption coefficient . . . 71
5.83 $NbTe_2$ reflectivity . . . 71
5.84 $NbTe_2$ refractive index . . . 71
5.85 $NbTe_2$ extinction coefficient . . . 71
5.86 Absorption coefficient within the visible range . . . 71
5.87 Reflectivity within the visible range . . . 71
5.88 Real part of dielectric function . . . 72
5.89 Relative stability . . . 73
5.90 PBE+D2 . . . 74
5.91 PBE . . . 74
5.92 PBE+TS . . . 74
5.93 NbS_2 electronic Bands . . . 77
5.94 Electronic DOS . . . 77
5.95 NbS_2 phonon Bands . . . 77
5.96 Phonon DOS . . . 77
5.97 NbS_2 absorption coefficient . . . 78
5.98 NbS_2 reflectivity . . . 78
5.99 NbS_2 refractive index . . . 78
5.100 NbS_2 extinction coefficient . . . 78
5.101 Absorption coefficient within the visible range . . . 78
5.102 Reflectivity within the visible range . . . 78
5.103 Real part of dielectric function . . . 79
5.104 Relative stability . . . 80
5.105 $NbSe_2$ electronic Bands . . . 82
5.106 Electronic DOS . . . 82
5.107 $NbSe_2$ phonon Bands . . . 82
5.108 Phonon DOS . . . 82
5.109 $NbSe_2$ absorption coefficient . . . 83
5.110 $NbSe_2$ reflectivity . . . 83
5.111 $NbSe_2$ refractive index . . . 83
5.112 $NbSe_2$ extinction coefficient . . . 83
5.113 Absorption coefficient within the visible range . . . 83
5.114 Reflectivity within the visible range . . . 83
5.115 Real part of dielectric function . . . 84

List of Tables

1.1 Polytypes of TMDs . . . 3

4.1 Non-spherical atom correction energies . . . 36

5.1 Structural and energetic properties of NbP_2 . . . 42
5.2 Calculated values of independent elastic coefficients . . . 42
5.3 Calculated B, E, G, ν and B/G . . . 42
5.4 Structural and energetic properties of VP_2 . . . 46
5.5 Calculated values of independent elastic coefficients . . . 47
5.6 Calculated B, E, G, ν and B/G . . . 47
5.7 Structural and energetic properties of VSe_2 . . . 52
5.8 Calculated values of independent elastic coefficients for VSe_2 . . . 52
5.9 Calculated B, E, G, ν and B/G . . . 52
5.10 crystal system information . . . 56
5.11 Stable hexagonal VS_2 . . . 58
5.12 Calculated values of independent elastic coefficients . . . 58
5.13 Calculated B, E, G, ν and B/G . . . 59
5.14 Structural and energetic properties VTe_2 . . . 63
5.15 Calculated values of independent elastic coefficients . . . 64
5.16 Calculated B, E, G, ν and B/G . . . 64
5.17 Structural and energetic properties of $NbTe_2$ . . . 68
5.18 Calculated values of independent elastic coefficients for $NbTe_2$ . . . 69
5.19 Calculated B, E, G, ν and B/G . . . 69
5.20 crystal system information . . . 73
5.21 Structural and energetic properties of NbS_2 . . . 75
5.22 Calculated values of independent elastic coefficients for NbS_2 . . . 75
5.23 Calculated B, E, G, ν and B/G . . . 76
5.24 crystal system information . . . 80
5.25 Structural and energetic properties of hexagonal $NbSe_2$ . . . 81
5.26 Calculated values of independent elastic coefficients . . . 81
5.27 Calculated B, E, G, ν and B/G . . . 81

1 Calculated eigenvalues in Gpa obtained from elastic constants calculation for all compounds considered in this study . . . 90
2 convergence of Drude plasma frequency squared with respect to k-points at DFT level in various directions . . . 91

1

INTRODUCTION

For about two decades, a lot of research has been focused on the study of graphene, a 2D honeycomb structure of carbon. Graphene is a layered material that has attracted much attention due to its unique and outstanding electrical, mechanical and optical characteristics [1–4]. Layered compounds are those that possess strong lateral chemical bonding in-plane but display weak van der Waals interaction between planes. Pristine graphene is a zero band gap semiconductor and its intrinsic inversion symmetry strongly suppresses the spin-orbit coupling. Hence, graphene cannot be used as a switching material in spin-based transistors.

Although graphene has an extremely high mobility of 15,000 $cm^2/(Vs)$ [5] and is easy to scale down, the absence of an inherent band-gap limits the potential for graphene to be used in logic circuits which is a drawback since many important applications in optics and transistor technology require a band gap. This led to vigorous research effort to functionalise it to achieve band gap manipulation. Graphene, while being fundamentally and technologically interesting for a variety of applications, is chemically inert and can only be made active by functionalization with desired molecules, which results in the loss of some of its exortic properties.

Recently, molybdenum disulphide and tungsten disulphide have emerged as competing materials for nano-electronics due to their interesting properties like the presence of a band gap, thermal stability upto 1100 °C and absence of dangling bonds [6]. This resulted in successful implementation of a monolayer MoS_2-based field effect transistor, with HfO_2 as a gate insulator. Molybdenum and tungsten disulphides have been synthesized but potential applications of these materials have been hampered by two serious drawbacks: their bandgap, a property essential for making transistors and other electronic devices, is too small, giving a low signal-to-noise ratio and they lack the ability to switch rapidly on and off.

MoS_2 and WS_2 being members of Transition Metal Dichalcogenides (TMDs) opened up research for other combinations of TMDs with the hope of getting one whose properties are comparable to those of graphene, MoS_2 and WS_2, as well as be in a position to ascertain if they can be applied in plasmonic related fields by launching an in-depth analysis of their optical spectra and constants i.e location of plasma frequency and index of refraction.

1.1 Chalcogenides

A chalcogenide is a chemical compound consisting of at least one chalcogen anion and at least one or more electropositive element. Although all group 16 elements of the periodic table are defined as chalcogens, the term chalcogenide is more commonly reserved for sulphides, selenides and tellurides rather than oxides. Depending on the ratio of transition metal atoms to chalcogen atoms, transition metal chalcogenides, dichalcogenides and trichalcogenides exists among others. In this study our focus was on layered transition metal dichalcogenides since they are analogous to graphene.

Generally, TMDs containing group 4 - 7 transition elements have a layered structure, while those with group 8 - 10 transition metals have non-layered stuctures. Each layer has a thickness of (6 - 7) Å, which consists of hexagonally packed layer of metal atoms bonded by weak van der Waals forces [7]. TMDs have attracted great attention from scientists because of their rich, unique as well as diverse properties that give rise to potential application in integrated circuits, energy storage i.e it is contended that edge planes of MoS_2 are active sites for hydrogen evolution reaction and is used in lithium batteries as anode, 2H-NbS_2 is applied as a catalyst for purification of petroleum [8] as well as being used as cathode materials in secondary batteries [9] and in humidity sensors [10, 11], transparent conducting electrodes [12] among others as well as their accessibility for easy synthesis using various chemical and physical methods [13–15].

Many metal ores exists as chalcogenides. Photoconductive chalcogenide glasses are used in xerography, metal dichalcogenide MoS_2, for example, being layered is employed as a common solid lubricant since it can withstand higher temperatures than graphite [16,17]. This is because weak non-covalent interactions between adjacent layers and the anisotropic character of TMD structures result in easy shearing of the layers even under high pressure leading to good lubricant properties which promotes its applicability in aerospace engineering fields. This not only acts as a supplement to liquid lubricants but also reduce friction arising from surface contacts as well as enhancing loading capability of heavy machinery.

They also exhibit other unique properties namely low resistance, excellent optical transmittance, chemical stabilities and high mechanical stability hence can be applied in photovoltaic devices. The various properties of TMDs arise from the filling of the non-bonding d-bands from the group 4 to group 10 species. When the orbitals are partially occupied, the TMDs display metallic properties, whereas when they are fully occupied, they display semiconducting ones [18]. TMDs exhibit a variable band gap between 0 eV and 2 eV depending on the elemental combination, the number of layers, and the presence or lack of a doping atom.

TMDs monolayers are atomically thin semiconductors. The discovery of graphene shows how new physical properties emerge when a bulk crystal of macroscopic dimensions is thinned down to one atomic layer (size sinking). Their monolayers have the following properties that are distinctly different from those of semimetal graphene; some TMDs i.e MoS_2, WS_2, $MoSe_2$, WSe_2 and $MoTe_2$ have direct band gap and can be used in electronics as transistors and in optics as emitters and detectors [19]. Also it is observed that as the number of layers decreases from bulk to monolayer limit, the indirect bandgap TMDs increases and becomes so large in the monolayers making them change from indirect to direct semiconductors. Materials with indirect optical bandgap requires a thick active layer for solar conversion and thus leads to costly fabrication of large area materials [20].

In addition, due to quantum confinement and surface effects, monolayer and few-layered TMDs exhibit a variety of exciting properties not seen in their bulk counterparts; TMDs monolayer crystal has no inversion center, which allows access to a new degree of freedom of charge carriers, namely the k-valley index and valleytronics [21], The strong spin-orbit coupling in TMDs monolayers leads to a spin orbit

splitting of hundreds of meV in the valence band and a few meV in the conduction band, which allows control of the electron spin by tuning the excitation laser photon energy [22], TMDs are highly anisotropic crystals that easily intercalate with organic molecules or alkali metal atoms or compounds [23].

Chalcogenides create a very stable binary compounds with transition elements forming layered crystalline structures especially with transition metals of group IV - VII. The work on TMDs monolayers is an emerging research and development field since the discovery of the direct bandgap and the potential applications of electron Valley Physics. Ultrathin TMDs include semiconductors with giant spin-orbit coupling and as a result they are considered to be complementary to graphene [24, 25].

1.2 Composition, structure and stacking of TMDs

TMDs have a general formula MX_2 where the transition metal and chalcogen have +4 and -2 oxidation states respectively. A single layer of TMDs can exhibit either trigonal prismatic (2H) or octahedral metal coordination phase (1T) that bears different properties depending on transition metal coordination and stacking sequence of multiple layers. Since each individual layer could possess any of the two coordination phases mentioned, it implies that many different polymorphic structures could exhibit the same TMD material resulting in a diverse variety of properties.

Most commonly encountered polymorphs of TMDs are tetragonal (1T) of point group D_{3d}, hexagonal (2H) of point group D_{3h} and rhombohedral (3R) of point group C_{3v} where the given digits shows the number of X-M-X units in the unit cell [26]. The 2H phase has AbA BaB stacking sequence whereby chalcogen atoms overlap along the z-axis with the metal atoms of the adjacent layer. On the other hand, 1T phase exhibit AbC AbC stacking sequence due to symmetry whereas 3R have BcB CaC AbA stacking sequence in unit cell where metal and chalcogen atoms are shifted. It is worth noting that these materials can undergo phase transition i.e through alkali intercalation which completely alters their electronic properties.

Relative stability between different phases (H and T) is greatly affected by the two parameters: the thickness of layers and temperature. Damien *et al.* [27] noted that stacking sequence can break the inversion symmetry of bilayer TMDs allowing an additional pathway for tuning optical, electronic and spintronic properties of TMDs. Bandaru [28] proposed a simplified nomenclature shown in Table 1.1 that is applicable to different phases of TMDs.

Table 1.1: Polytypes of TMDs

Phase	Space group symmetry	Metal co-ordination	Stacking sequence
1T	P3m1	octahedral	AbC
$2H_a$	P63/mmc	Trigonal prismatic	BcBAcA
$2H_b$	P63/mmc	Trigonal prismatic	BcBAbA
$2H_c$	P63/mmc	Trigonal prismatic	BaBAbA
3R	R_3m	Trigonal prismatic	BcBCaCAbA

Since TMDs exhibit different stacking sequence despite some belonging to the same point group, they exhibit different electrical, mechanical, physical and optical properties [29].

2

REVIEW OF TMDs

In this section we briefly discuss what has already been explored about the materials of interest. The layered TMDs have been the subject of many recent studies. To flashback, structures and properties as of four decades ago have been reviewed by Wilson and Yoffe [30]. Electronic properties were more recently reviewed by Yoffe [31]. Lieth and Terhell [32], Balchin [33] and Levy [34] have summarized preparation and crystal growth procedures. Hullinger [35] as well has compiled extensive structural information of these materials.

2.1 Transition metal dipnictogenides

2.1.1 Niobium diphosphide (NbP_2)

Little information is known about NbP_2 compared to other well studied compounds in the periodic table. Hullinger in 1964 [35] reported only the lattice parameters as derived from powder diffraction patterns which is our only source of experimental information. He noted that NbP_2 is monoclinic and isomorphous to tantalum diarsenide ($TaAS_2$). Recall that phosphorus can never exist as a free element on earth since it is highly reactive. It is mainly obtained from phosphate rock (calcium phosphate) and is normally stored under water in chemical laboratories. NbP_2 is formed by reacting phosphorus and niobium under inert atmospheric conditions or vacuum because of reactive nature of phosphorus.

2.1.2 Vanadium diphosphide (VP_2)

Vanadium-phosphorus system was first explored by Zumbusch and Biltz [36]. They explored various concentrations: $VP_{0.6}$, $VP_{0.8}$, $VP_{1.0}$ and $VP_{1.2}$. Hullinger also studied VP_2 alongside NbP_2 using diffraction patterns as well. In 1975, Margaret *et al.* prepared VP_2 crystals using chemical transport method where they used iodine as transport agent. Red phosphorus used in their reaction was 99 % pure and vanadium metal was 99.95 % as per their supplier. The main impurities (in parts per million) were Fe 200, P 125, Ca 60, Cr 50 and Mn 50. They synthesized VP_2 by heating red phosphorus and vanadium metal flakes in evacuated and sealed silica tubes at 800 °C for three days. From their analysis, phosphides of vanadium, niobium and tantalum (VP_2, NbP_2 and TaP_2) are structurally similar [37]. VP_2 belongs to the $NbAS_2$-type structure of space group C2/m.

2.2 Transition metal dichalcogenides

2.2.1 Vanadium diselenide (VSe_2)

F. Levy and Y. Froidevaux [34] studied VSe_2 when they were exploring compounds of $V_xTi_{1-x}Se_2$ and $Ta_xTi_{1-x}Se_2$ at various concentration levels and environmental conditions. For VSe_2, they did crystal growth at two different temperatures. First, they did their experiments at a range of (650 - 700) °C sublimation temperature and (500 - 650) °C growth temperature. In the second instance, they did their experiments at a fixed temperature of 900 °C and 800 °C for sublimation and growth respectively. In both cases, they used iodine too as in the case of VP_2 as transport agent and selenium was supplied in excess to ensure the best stoichiometry of the growth crystals was attained. Growth time was between 30 - 350 hours. They concluded that layered selenides of titanium, tantalum and vanadium ($TiSe_2$, 1T-$TaSe_2$ and VSe_2) are rather easy to alloy and to grow as single crystal by chemical transport technique and crystallizes only in stable octahedral coordination of cations. G. Wiegers [38] reported that VSe_2 behaves as a d-band metal and at about 110 K, it shows anomalous properties which are attributed to charge density waves.

2.2.2 Vanadium ditelluride (VTe_2)

Bronsema *et al.* [39] prepared $V_{1+x}Te_2$ by heating mixture of elemental solids in evacuated quartz ampoules at 1000 K for a week after which the samples were slowly cooled. As the case of VSe_2, powder diffraction showed that in addition to $V_{1+x}Te_2$, also elemental tellurium was present corresponding to tellurium-rich limit of the homogeneity range. The observed diffraction pattern was complex due to simultaneous occurrence of distortion of the $Cd(OH)_2$-type structure of vanadium ditelluride in three equivalent directions which can be attributed to its anisotropy. They noted that it is difficult to grow single crystals of $V_{1+x}Te_2$ by vapour transport.

2.2.3 Vanadium disulphide (VS_2)

Among all the compounds considered in this study, VS_2 has been explored more by a number of researchers. It was first studied by Murphy *et al.* [40] in 1977. They analyzed various concentrations of ternary compound composed of lithium, vanadium and sulphur whose chemical representation is given by Li_xVS_2 ($0 \leq x \leq 1$). The series of Li_xVS_2 was prepared by oxidation of $LiVS_2$ with iodine in acetonitrile according to equation below;

$$LiVS_2 + \frac{1}{2}(1-x)I_2 \longrightarrow Li_xVS_2 + (1-x)LiI \tag{2.2.1}$$

This oxidation was rapid and quantitative at room temperature. All Li could be removed from $LiVS_2$ in a matter of minutes depending on stirring rate because of the heterogeneous nature of the reaction. The highly coloured I_2 solution became colourless upon completion of reaction. The VS_2 prepared by this method was stable in air or in Ar to 300 °C, beyond which sulphur loss occur.

They concluded that the compound was hexagonal (CdI_2-type) and transition was observed in magnetic susceptibility at $\sim$ 305 K. No change was observed in x-ray patterns above or below this transition temperature. VS_2 has attracted research interest due to its intrinsic magnetism and potential application as high performance functional nanomaterial. Zhang *et al.* [41] reported that below room temperature,

both bulk and monolayer VS_2 prefer to exhibit hexagonal (H) structure instead of trigonal (T) structure. At room temperature, although H monolayer VS_2 remains stable than T-VS_2, the bulk T-VS_2 becomes more stable than H-VS_2. Changing slab thickness or temperature leads to phase transition between H and T. Few layered ultrathin VS_2 nanosheets have been exfoliated showing high conductivity and 2D permeable channels, with great promise for applications in fabrication of planar qausi-two dimensional supercapacitors.

Recently, VS_2 has been synthesized successfully paving way to realization of TMD based spintronic [42]. Feng *et al.* proposed that vanadium disulphide nanosheets with quasi-two dimensional electronic structure is a very promising material for high moisture responsiveness. Sensitivity of moisture responsiveness normally relies on interval structures of the grain boundaries, as well as the electropositivity of exposed metal atoms, which greatly influence electrical response triggered by moisture stimuli. In this perspective, 2D planar structures with large specific surface area could largely enrich the number of edge-exposed atoms and active intervals to absorb water molecules [43].

2.2.4 Niobium disulphide (NbS_2)

Fisher and Sieko [44] prepared samples with stoichiometries near NbS_2 from the elements by reacting them at 950 °C followed by quenching from an annealing temperature of 750 °C. Stoichiometry of the products depended on pressure of excess sulphur during annealing. In the range of $0 < x < 0.18$ for $Nb_{1+x}S_2$ only two phases were observed, stoichiometric line phase corresponding to the 2H polytype NbS_2 and a non-stoichiometric phase corresponding to 3R-$Nb_{1+x}S_2$. For $0.07 < x < 0.18$, only the 3R polytype was obtained.

Superconducting transition temperatures, determined by Meissner flux expulsion indicated that 2H-NbS_2 superconducts with a transition temperature of 6.3 K. 3R-$Nb_{1+x}S_2$ does not superconduct above 1.7 K. They noted that susceptibility of 2H-NbS_2 was about twice as great and showed a slight linear increase as the temperature was decreased. They reported existence of four phases of niobium disulphide namely 2H-NbS_2 and 3R-$Nb_{1+x}S_2$ (both being stoichiometric) and 2H-$Nb_{1+x}S_2$ and 3R-$Nb_{1+x}S_2$ (non-stoichiometric). They believed that nonstoichiometry was accommodated by excess niobium atoms in the gap between the sandwiches.

2.2.5 Niobium ditelluride ($NbTe_2$)

Single crystals of $NbTe_2$ were grown by Nitshe *et al.* [45] using an iodine carrier with suitable gradient between hot and cold ends of the evacuated quartz tube. This could also be done by vapour phase transport method using iodine gas as transport agent as in the case of other TMDs. $NbTe_2$ single crystals obtained by Neha *et al.* [46] were shiny black and opaque. Its crystal structure is monoclinic with the space group C2/m. From their diffraction results, $NbTe_2$ has good crystallinity as supported by its well-defined sharp diffraction lines. $NbTe_2$ is one of typical TMDs that shows charge density waves [47]. Its experimental value of electrical resistivity and diamagnetic susceptibility have been reported by Shoichi *et al.* [48] for high quality single crystals. Erdogam and Kirby [49] did Raman scattering measurements of layered $NbTe_2$ and from their analysis, it indicated no evidence of phase transition for temperatures between 80 K and 420 K.

2.2.6 Niobium diselenide ($NbSe_2$)

Kershaw *et al.* [50] reported that $NbSe_2$ crystallizes in the P6/mmc space group. Single crystals were grown by chemical transport method using iodine or bromine as the transport agent. They determined crystallographic parameters of $NbSe_2$ on powder samples with a Norelco diffractometer using monochromatic radiation (AMR-202 Focusing monochromator). From their resistivity curves, $NbSe_2$ showed metallic behaviour. Superconducting transition for $NbSe_2$ as measured on single crystals took place at 7 K which was in agreement with the value reported by Revolinsky *et al.* [51].

Brixner [52] indicated that $NbSe_2$ behaves as a metal because there is a free electron available for the conduction band. 2H-$NbSe_2$ has AbA stacking sequence. Electronic and mechanical anisotropy in $NbSe_2$ and other TMDs arises from relatively weak van der Waals bonding between adjacent chalcogenide layers and its bonding permits intercalation of Lewis bases [53, 54]. Lee *et al.* [55] reported that as temperatures of 2H-$NbSe_2$ is increased, the sign of Hall coefficient changes at 26 K from n-type to p-type. This behaviour was indeed unusual in that the sign of Hall coefficient was positive at room temperature while Seebeck coefficient was negative. Jerome [56] did analysis of the effect of hydrostatic pressure on superconductivity of $NbSe_2$ and noticed that superconducting transition temperature of the layer crystal niobium diselenide increases from 6.9 K to 8.5 K upon application of 17 kbar hydrostatic pressure.

3

THEORETICAL FRAMEWORK

In this section, we discuss the fundamental theories supporting this study both at ground state and excited state. Density functional theory and its methods; Kohn-Sham equations; total energy functionals; exchange and correlation energy functionals and van der Waals interaction principally helps us exploit the ground state properties whereas many-body perturbation theory; GW Approximation and Bethe Salpeter Equations provide excited state properties. In addition, plasmonic materials are reviewed in a nutshell in order to relate between the obtained optical data and possible application.

3.1 Density Functional Theory (DFT)

Computer simulations are becoming most convenient tools used to explore features of possible representational structures in order to understand systems and their behaviour. A successful application of DFT to a materials problem involves three distinct steps. At initial stage, an engineering problem is translated into a computable atomistic model, thereafter, the required physicochemical properties are computed and at a later stage, laboratory experiments are carried out to validate simulation results. Computer simulation is represented as running the model of a system used to explore and gain new insights into new technology and to estimate its performance [57].

Hohenberg and Kohn wrote a paper in 1964 [58] that marked the dawn of modern DFT. They displayed that a special role can be assigned to density of particles in the ground state of quantum many-body system. Density can be considered as a 'basic variable' i.e all properties of the system can be considered to be unique functionals of ground state density. The Hamiltonian (H) is determined by the ground state density [59]. In principle, the wavefunction (ψ) of any state is determined by solving Schrödinger equation with this Hamiltonian [60]. For a single electron moving in a potential *V(r)*, Schrödinger equation becomes;

$$H\psi = E\psi, \tag{3.1.1}$$

where E is eigenvalue of the system, substituting Hamiltonian, H in equation (3.1.1) gives;

$$\left[\frac{-\hbar^2}{2m}\nabla^2 + V(r)\right]\psi(r) = E\psi(r). \tag{3.1.2}$$

If there is more than one electron (i.e many-body problem), then Schrödinger equation can be expressed

as;

$$\left[\sum_{i}^{N}\left(\frac{-\hbar^2}{2m}\nabla^2+V(r_i)\right)+\sum_{i<j}U(r_i,r_j)\right]\psi\left(r_1,r_2,\ldots,r_N\right)=E\psi\left(r_1,r_2,\ldots,r_N\right), \tag{3.1.3}$$

where N is the total number of electrons and $U(r_i,r_j)$ is the electron-electron interaction. One specifies the system by choosing $V(r)$, substitutes it to the Schrödinger equation, solves that equation for the ψ and then calculate observables [61–64]. One among the observables that are calculated this way is the particle density. If we express potential $V(r)$ in terms of electron density;

$$\hat{V}=\int d^3rV(r)\hat{n}(r), \tag{3.1.4}$$

equation (3.1.4) gives expectation value of $\hat{V}$;

$$\langle\psi|\hat{V}|\psi\rangle=\int d^3rV(r)\hat{n}(r). \tag{3.1.5}$$

From the above equations we can write charge density as;

$$n(r_i)=\langle\psi|\hat{n}(r_i)|\psi\rangle=N\int d^3r_2\int d^3r_3\ldots\int d^3r_N\psi^*\left(r_1,r_2,\ldots,r_N\right)\psi\left(r_1,r_2,\ldots,r_N\right). \tag{3.1.6}$$

3.2 Hohenberg-Kohn theorem

Hohenberg-Kohn theorem tries to formulate density functional theory as an exact theory of many body systems. If we consider a collection of arbitrary number of electrons enclosed in a large box whose motion is influenced by mutual coulomb repulsion and some external potential V(r). Its Hamiltonian can then be expressed as;

$$H=T+V+U=\frac{1}{2}\int\nabla\psi^*(r)\nabla\psi(r)dr+\int V(r)\psi^*(r)\psi(r)dr+\frac{1}{2}\int\frac{1}{|r-r'|}\psi^*(r)\psi^*(r')\psi(r')\psi(r)drdr'. \tag{3.2.1}$$

Electronic density in ground state n(r) is a functional of V(r) and is given by;

$$n(r)\equiv\langle\psi|\psi^*(r)\psi(r)|\psi\rangle. \tag{3.2.2}$$

For simplicity, we assume that ground state ψ is non-degenerate suggesting that two or more different states of a system cannot give the same value of energy upon measurement. We then apply *reductio ad absurdum* (a proof by contradiction) to show that V(r) is a unique functional of n(r).

If we assume that there also exist another ground state ψ' that gives rise to the same electron density n(r); unless $V'(r)$ - V(r) = constant; ψ' cannot be equal to ψ since they in principle satisfy different Schrödinger equations. If we denote ground state energies and Hamiltonian associated with ψ and ψ' by E, E$'$ and H, H$'$ respectively, we obtain via minimization of ground state the following expressions;

$$H=T+U_{el}+V_{ext}\Rightarrow H\psi=E\psi, \tag{3.2.3}$$

and

$$H'=T+U_{el}+V'_{ext}\Rightarrow H'\psi'=E'\psi'. \tag{3.2.4}$$

From variational principle; starting from E $'$ we get;

$$E^{'} = \langle \psi^{'} | H^{'} | \psi^{'} \rangle < \langle \psi | H^{'} | \psi \rangle, \tag{3.2.5}$$

assuming E$'$ is the ground state energy. Therefore;

$$\langle \psi | H^{'} | \psi \rangle = \langle \psi | H - V_{ext}(r) + V^{'}_{ext}(r) | \psi \rangle = E + \int dr \;\; n(r) \left[V^{'}_{ext}(r) - V_{ext}(r) \right], \tag{3.2.6}$$

intergrating primed and unprimmed parameters in the above equation yields;

$$E^{'} < E + \int dr \;\; n(r) \left[V^{'}_{ext}(r) - V_{ext}(r) \right]. \tag{3.2.7}$$

Also starting from E, we get;

$$E = \langle \psi | H | \psi \rangle < \langle \psi^{'} | H | \psi^{'} \rangle = E^{'} + \int dr \;\; n^{'}(r) \left[V_{ext}(r) - V^{'}_{ext}(r) \right], \tag{3.2.8}$$

by above assumption, n(r) = n$'$(r), where n$'$(r) is another ground state charge arising from another Hamiltonian (H$'$) and whose ground state energy is (E$'$) resulting in;

$$E < E' + \int dr \;\; n(r) \left[V_{ext}(r) - V^{'}_{ext}(r) \right]. \tag{3.2.9}$$

Adding equation (3.2.7) and (3.2.9) leads to the contradictory inequality;

$$E + E^{'} < E + E^{'}. \tag{3.2.10}$$

From equation (3.2.10), it is clear that two different ground state wavefunctions cannot lead to the same ground state charge density [57, 58]. Moreover, this proof can also be extended to degenerate ground states where more than one ground state exists.

3.3 Kohn-Sham equations

Hohenberg-Kohn theorem gives the possibility of using the ground state density to calculate properties of the system but it does not provide a way of finding the ground state density. Kohn-Sham (K-S) equations becomes handy in filling this gap. Ansatz made by Kohn and Sham provide a way to make useful approximate ground state functionals for real systems of many electrons. In their approach, we can replace the original many-body problem by an auxilliary independent particle problem with an ansatz that in principle leads to exact calculations of properties of many-body systems using independent particle methods. Two assumptions are made in K-S ansatz: that the exact ground state density can be represented by the ground state density of an auxilliary system of non-interacting particles and that auxilliary Hamiltonian is chosen to have usual kinetic operator and an effective local potential $V_{eff}(r)$, acting on an electron at point r. To derive K-S equations, we have to consider the ground state energy as a functional of the charge density (ρ).

$$E[\rho(r)] = T[\rho(r)] + \int \rho(r) V(r) dr + E_{ee}, \tag{3.3.1}$$

where the first expression on the right hand side of equation (3.3.1) denotes kinetic energy, second term stands for interaction with external potential including electron nuclei interaction and the last term represents electron-electron interaction which can be expressed in the form [65];

$$E_{ee}[\rho(r)] = \frac{1}{2}\int \frac{\rho(r)\rho(r^{'})}{|r-r^{'}|}drdr^{'} + E_{xc}[\rho(r)]. \tag{3.3.2}$$

The first term in right hand side of equation (3.3.2) denotes electron-electron electrostatic interaction and the second one, non-classical exchange correlation energy. Kohn and Sham derived a set of single particle Schrödinger equation by re-introducing wavefunctions (ψ_i) and its conjugate (ψ_i^*) [66] which are related to charge density in the following way;

$$\rho(r) = \sum_{i=1}^{n} \psi_i^*(r)\psi_i(r), \tag{3.3.3}$$

where n represents the number of electrons. Kinetic energy is given by;

$$T[\rho(r)] = \frac{-\hbar^2}{2m}\sum_{i}^{n}\langle\psi_i|\nabla^2|\psi_i\rangle. \tag{3.3.4}$$

If the wavefunctions are required to be orthonormal [67];

$$\int \psi_i^*(r)\psi_j(r)dr = \delta_{ij} = \begin{cases} 0 & \text{if} \quad i \neq j \\ 1 & \text{if} \quad i = j \end{cases}, \tag{3.3.5}$$

then we can define a functional of wavefunctions as;

$$\Omega[\psi_i] = E[\psi_i(r)] - \sum_i \sum_j \epsilon_{ij}\int \psi_i^*(r)\psi_j(r)dr, \tag{3.3.6}$$

in which ϵ_{ij} are lagrange multipliers to ensure that the wavefunctions are orthonormal. Minimization of $\Omega[\psi_i]$ with respect to $\psi_i^*(r)$ gives Kohn-Sham equations [68];

$$\left[\frac{-\hbar^2}{2m}\nabla^2 + V_{eff}(r)\right]\psi_i(r) = \epsilon_i\psi_i(r). \tag{3.3.7}$$

Effective potential $[V_{eff}(r)]$ and its component, exchange-correlation potential $[V_{xc}(r)]$ are related via the following expression;

$$V_{eff}(r) = V(r) + \int \frac{\rho(r^{'})}{|r-r^{'}|}dr^{'} + V_{xc}(r), \tag{3.3.8}$$

where

$$V_{xc}(r) = \frac{\delta E_{xc}}{\delta\rho(r)}. \tag{3.3.9}$$

Kohn-Sham method treats kinetic energy exactly leaving $\mathrm{E}_{xc}[\rho(r)]$ to be approximated. This is valid for several reasons; $T[\rho(r)]$ is typically a very large part of the energy while $\mathrm{E}_{xc}[\rho(r)]$ is smaller part, $T[\rho(r)]$ is largely responsible for density oscillations of the shell structure which are accurately described by the Kohn-Sham method and $\mathrm{E}_{xc}[\rho(r)]$ is somewhat better suited to the local and semi-local approximations than $T[\rho(r)]$. This signify that if the universal functional $\mathrm{E}_{xc}[\rho(r)]$ is known, then the exact ground state energy and density of many body electron problem could be found by solving K-S equations for independent particles.

3.4 Density functional theory methods

There are basically three types or categories of DFT methods namely local density approximation, generalized gradient approximation, hybrid functionals and meta-GGA.

3.4.1 Local Density Approximation (LDA)

LDA assumes that the density of molecule is uniform throughout the molecule. The exchange correlation energy at each point in the system is assumed to be the same as that of uniform electron gas of the same density. This approximation was originally introduced by Kohn and Sham and holds for a slowly varying density. Using this approximation, the exchange-correlation energy for density $\rho(r)$ is given by;

$$E_{xc}^{LDA} = \int \rho(r)\epsilon_{xc}(\rho)dr, \tag{3.4.1}$$

where $E_{xc}(\rho)$ is the exchange-correlation energy per particle of uniform electron gas of density ρ. The exchange-correlation potential is expressed as;

$$V_{xc}^{LDA}[\rho(r)] = \frac{\delta E_{xc}^{LDA}}{\delta\rho(r)} = \epsilon_{xc}(\rho) + \rho(r)\frac{\partial\epsilon_x(\rho)}{\partial\rho}. \tag{3.4.2}$$

For practical use of LDA in calculations, it is necessary to determine the exchange-correlation energy for a uniform electron gas of a given density. By splitting $E_{xc}(\rho)$ into exchange and correlation potentials gives;

$$\epsilon_{xc}(\rho) = \epsilon_x(\rho) + \epsilon_c(\rho). \tag{3.4.3}$$

3.4.2 Generalized Gradient Approximation (GGA)

GGA accounts for non-uniformity of the electron density. While LDA approximates the energy of the true density by energy of a local constant density, it fails in situations where density undergoes rapid changes such as in molecules. An improvement on this can be made by considering the gradient of the density, which is known as generalized gradient approximation. It can be expressed mathematically as;

$$E_{xc} = E_{xc}[\rho(r), \nabla\rho(r)]. \tag{3.4.4}$$

This can lead to a large improvement over LDA results with accuracy approaching that of correlated wavefunction methods such as MP2 (second order Moller-Plessett perturbation theory) and in some cases surpassing. Although there is only one LDA, several different parametrizations of GGA such as PW91, PBE, RPBE and WC exist.

3.4.3 Hybrid functionals

Hybrid methods attempt to incorporate some of more useful features from *ab initio* methods with some of the improvements of DFT mathematics. A hybrid exchange-correlation functional is usually constructed as a linear combination of the Hartree-Fock exact exchange functional;

$$E_x^{HF} = -\frac{1}{2}\int\int \psi_i^*(r_1)\psi_j^*(r_1)\frac{1}{r_{12}}\psi_i(r_2)\psi_j(r_2)dr_1dr_2. \tag{3.4.5}$$

Parameters determining the weight in each individual functional are specified by fitting the functional's predictions to experimental or accurately calculated thermochemical data. Examples of hybrid functionals are: B3LYP (Becke 3 term correlation functional; Lee, Yang and Parr exchange functional) that is commonly used method by computational chemistry practitioners and MPW1K (Modified Perdew-Wang one parameter hybrid for Kinetics).

3.4.4 Meta-GGA

Meta-GGA is a modified form of GGA that incorporates non-interacting kinetic energy density, local density and the gradient of the local density [69]. Tran and Blaha [70] proposed that meta-GGA gives better band gaps comparable to experimental for a broad range of materials. Morever, it is computationally economical way of computing band gaps as compared to other techniques such as GW. As the case of Hybrid functionals, several flavours of meta-GGA fuctionals exist such as modified Becke-Johnson (mBJ) exchange potential, strongly constrained and appropriately normed (SCAN) semilocal density function and 'made simple' (MS) functionals, just to mention a few [71].

3.5 Total exchange-correlation energy functionals

Let's consider $E[\rho]$ as sum of several terms. The basic principle as per Kohn and Sham is to identify those terms that are known exactly, define others in some convenient way and then put our attention to the remaining unknown terms. In this derivation, we will only consider closed shell ('spin-unpolarized') system for simplicity. The total energy of the system is given by;

$$E[\rho] = T_s[\rho] + V[\rho] + U[\rho] + E_{xc}[\rho]. \tag{3.5.1}$$

Kinetic energy of a hypothetical system of non-interacting electrons can be written as;

$$T_s[\rho] = -\frac{1}{2}\sum_{k}^{Occ}\int \phi_k^*(r)\nabla^2\phi_k(r), \tag{3.5.2}$$

parameter $\sum_k^{Occ}$ signify that each term in the sum must be included as many times as there are electrons occupying the orbital $\phi_k(r)$. Total ground state density is exactly equal to $\rho(r)$, $\phi_k(r)$ are Kohn-Sham orbitals occupied by these electrons whereas $\phi_k^*(r)$ is its conjugate [72]. Electron density can then be expressed as;

$$\rho(r) = \sum_{k}^{Occ}|\phi_k(r)|^2. \tag{3.5.3}$$

Electrostatic energy functional $V[\rho]$ of the electron density interacting with external potential V(r) is given by;

$$V[\rho] = \int \rho(r)V(r)dr, \tag{3.5.4}$$

whereas electrostatic energy functional of $\rho(r)$ interacting with itself is given by;

$$U[\rho] = \frac{1}{2}\int dr_1 \int dr_2 \frac{\rho(r_1)\rho(r_2)}{|r_1 - r_2|}. \tag{3.5.5}$$

$E_{xc}[\rho]$ incorporates everything else that is not exactly defined and is referred to as exchange-correlation energy. This is the only unknown term in equation (3.5.1). K-S method packages all unknown functionals into the exchange-correlation energy functional. This enables us to approximate smaller part of energy (exchange-correlation part) rather than approximating total energy functional [73];

$$|E(\rho)| > |E_{xc}(\rho)|. \tag{3.5.6}$$

Initial step of solving exchange-correlation energy functional involves disintergrating $E_{xc}[\rho]$ into two parts, one large and one small. This is done in such a way that the larger part can be defined and computed exactly. This is analogous to breaking down total energy into its components. The two resultant parts are namely exchange and correlation energy functionals.

$$E_{xc}[\rho] = E_x[\rho] + E_c[\rho], \tag{3.5.7}$$

where $E_x[\rho]$ is the exchange energy functional that is exactly defined and $E_c[\rho]$ the correlation energy functional that is to be approximated and is analogous to equation (3.4.3). For spin-unpolarized systems where K-S orbital is doubly occupied, the exchange part is expressed as;

$$E_x^{exact}[\rho] = -\sum_{(k,l=1)}^{\frac{N}{2}} \int dr_1 \int dr_2 \frac{\phi_k(r_1)\phi_k^*(r_2)\phi_l^*(r_1)\phi_l(r_2)}{|r_1 - r_2|}. \tag{3.5.8}$$

Function $E_x^{exact}[\rho]$ is an implicit functional of density that depends on ρ through the K-S orbitals. If we consider atoms and molecules near equilibrium geometries, correlation energy is roughly an order of magnitude smaller than exchange energy.

$$|E_x^{exact}[\rho]| \gg |E_c[\rho]|. \tag{3.5.9}$$

This helps us to narrow down and approximate only $E_c[\rho]$ which is relatively small but important bit of total energy. At this point we have to recall the concept of exchange and correlation holes. Exchange-correlation energy can be defined as;

$$E_{xc}[\rho] = \frac{1}{2} \int dr_1 \rho(r_1) \int dr_2 \frac{\rho_{xc}(r_1, r_2)}{|r_1 - r_2|}, \tag{3.5.10}$$

where $\rho_{xc}(r_1, r_2)$ is exchange-correlation hole density. Implying that exchange-correlation energy represents coulombic interaction between an electron at r_1 and the surrounding exchange-correlation hole charge. Hole charge at r_2 is not static but depends on the current position of electron r_1. As before, exchange-correlation hole is sub-divided into exchange and correlation holes.

$$\rho_{xc}(r_1, r_2) = \rho_x(r_1, r_2) + \rho_c(r_1, r_2), \tag{3.5.11}$$

so we can then re-write the exchange functional as;

$$E_x[\rho] = \frac{1}{2} \int dr_1 \rho(r_1) \int dr_2 \frac{\rho_x(r_1, r_2)}{|r_1 - r_2|}, \tag{3.5.12}$$

and the analogous expression for correlation functional as;

$$E_c[\rho] = \frac{1}{2} \int dr_1 \rho(r_1) \int dr_2 \frac{\rho_c(r_1, r_2)}{|r_1 - r_2|}. \tag{3.5.13}$$

By comparing equation (3.5.8) and (3.5.13), the exact exchange hole for spin-unpolarized system is given by;

$$\rho_{xc}(r_1, r_2) = -\frac{2}{\rho(r_1)} \sum_{k,l=1}^{\frac{N}{2}} \phi_k(r_1)\phi_k^*(r_2)\phi_l^*(r_1)\phi_l(r_2). \tag{3.5.14}$$

$\frac{N}{2}$ comes in because we are considering closed shell system where Kohn-Sham orbital is doubly occupied. By giving up exact exchange in favour of approximations, it introduces an error into $E_x[\rho]$. Fortunately, this error is cancelled out by similar opposite-sign error in the approximation for $E_c[\rho]$. This has led to success for exchange-correlation functionals [74, 75].

3.6 Van der Waals interaction

Van der Waals interaction is a weak intermolecular force found in almost all organic liquids and solids. Solids held together by Van der Waals bonds are characterized by low melting point and are softer than those that are held together by strong ionic, covalent and metallic bonds. Although van der Waals (vdW) forces are much weaker than covalent or ionic interactions, they are crucial for cohesion of layered materials [76]. They are weak but always attractive, purely quantum forces that exists between every two (or more) fragments of matter and thus become important for large and realistic systems. Van der Waals interactions balance with electrostatic and exchange repulsion interactions and together they control for example packing of crystals, orientation of molecules on surfaces, formation of aggregates and structures of deoxyribonucleic acid (DNA) among others. For us to treat van der Waals interactions within DFT, we can divide the molecular system into atomic fragments and apply a pairwise approximation. Total energy of a system can be expressed in the following way in order to incorporate vdW interactions;

$$E_{DFT-disp} = E_{KS-DFT} + E_{disp}, \tag{3.6.1}$$

where E_{KS-DFT} is the normal self-consistent Kohn-Sham energy and E_{disp} is dispersion correction.

Grimme DFT-D2 method [77] entails adding a semi-empirical dispersion potential to the conventional Kohn-Sham DFT energy in which empirical dispersion correction is given by;

$$E_{disp} = -S_6 \sum_{i=1}^{N-1} \sum_{j=i+1}^{N} \frac{C_6^{ij}}{R_{ij}^6} f_{dmp}(R_{ij}), \tag{3.6.2}$$

where N stands for number of atoms, f_{dmp} is the damping function, C_6^{ij} (basically geometric mean of C_6^i and C_6^j) is coefficient that describes strength of interaction between atoms and R_{ij} is the distance between i and j atoms, N is the number of atoms in the system and -S_6 is the global scaling parameter that is dependent on DFT functional used i.e for PBE (S_6 = 0.75), BLYP (S_6 = 1.2) and B3LYP (S_6 = 1.05). In order to avoid near-singularities for small interatomic distances, a damping function (f_{dmp}) must be employed;

$$f_{dmp}(R_{ij}) = \frac{1}{1 + e^{-d(R_{ij}/R_r - 1)}}, \tag{3.6.3}$$

where R_r is the sum of atomic vdW radii.

On the other hand dispersion term used in Tkatchenko and Scheffler method (TS) [76] is formally identical to that of Grimme DFT-D2, however in TS method, dispersion coefficients and damping function are charge-density dependent. As a result, it is able to account for variations in vdW contribution

of atoms due to their local chemical environment. This method is based on the idea that accurate interatomic C_6 (dipole-dipole) dispersion coefficients can be calculated using a London-type formula from rescaled atomic dispersion coefficients and polarizabilities. Its dispersion correction for a material under periodic boundary condition can be expressed as;

$$E_{disp} = -\frac{1}{2}\sum_{A=1}^{N}\sum_{B=1}^{N}\sum_{L}{}' \frac{C_{6AB}}{R_{AB,L}^{6}} f_{dmp}(R_{AB,L}), \tag{3.6.4}$$

where the summations are over all atoms N and all translations of the unit cell L = (l_1, l_2, l_3), the prime indicates that A $\neq$ B for L = 0.

Damping function ensures that C6/R^6 term contributes to E_{disp} only for distances that are longer than typical bonding distance in order to avoid bogus interaction. If we rescale corresponding quantities calculated for free atoms based on proportionality between atomic volumes and polarizabilities (α) we obtain;

$$\alpha_A^{TS} = \frac{V_A^{eff}}{V_A^{free}} \alpha_A^{free}. \tag{3.6.5}$$

The term $\frac{V_A^{eff}}{V_A^{free}}$ is ratio of effective volume occupied by atom in solid/molecular environment to volume of free non-interacting atom.

From the above equation (3.6.5), we can then express effective dispersion coefficients of free atoms and atoms in molecules by applying proportionality as;

$$C_{6AA}^{TS} = \left[\frac{V_A^{eff}}{V_A^{free}}\right]^2 C_{6AA}^{free}, \tag{3.6.6}$$

which we can then rationalize by applying London dispersion formula. The combination rule that determines strength of dispersion interaction between different atoms can be expressed as;

$$C_{6AB} = \frac{2C_{6AA}C_{6BB}}{\left[\frac{\alpha_B}{\alpha_A}C_{6AA} + \frac{\alpha_A}{\alpha_B}C_{6BB}\right]}. \tag{3.6.7}$$

C_{6AA} and C_{6BB} gives strength of interaction when atom A and atom B are interacting among themselves whereas C_{6AB} gives strength of interaction when interacting with each other.

For non-overlapping electron densities, fermi-type damping function is used to eliminate spurious interaction at too short distances.

$$f_{dmp}(r^{AB,L}) = \frac{1}{1 + exp\left[-d\left(\frac{r^{AB,L}}{S_R R_{AB}^{eff}}\right) - 1\right]}. \tag{3.6.8}$$

In this method, S_R is specific for a given choice of exchange-correlation functional used whereas parameter *d* is fixed at 20. For PBE (S_R=0.94) and R_{AB}^{eff} is the sum of atom-in-molecule vdW radii.

3.7 Many Body Perturbation Theory (MBPT)

MBPT provides a convenient framework for calculation of electronic excitations. Electronic structure of materials and its response to an external perturbation are crucial for many experiments. What

experimentalists do is probe a system via bombardment, look at the response, change a parameter and start the process again. This is applicable in many spheres of life like; deformation of molecules upon absorption of radiation in cancer research, defect creation in nuclear waste, design of more efficient solar cells among others. To study electronic excitation spectrum of a solid, one performs photoemission experiments where photons with a certain energy are used as projectiles to knock out electrons.

During direct photoelectron spectroscopy a photon with energy $\hbar\omega$ impinges on the sample and ejects an electron whose kinetic energy can be measured. Binding energy of this electron is given by difference between kinetic and photon energy [78];

$$E_i = E_{kin} - \hbar\omega.$$

Expressing binding energy in the above form suggests that electrons are independent though in reality, they are correlated through the coulomb interaction and the ejection of an electron is always a many-body process.

Alternatively, binding energy, is equal to the difference between the total energy of a system of the N-particle ground state ψ_o^N and the energy of (N-1) particles ψ_i^{N-1} that remains after emission.

$$E_i = E_o^N - E_i^{N-1}. \tag{3.7.1}$$

In inverse photoemission/photoelectron spectroscopy, electrons are injected into the sample and the energy of the emitted photon measured. This results to an increase in electron number from N to N+1. Binding energy for inverse photoelectron spectroscopy is given by;

$$E_i = E_i^{N+1} - E_o^N. \tag{3.7.2}$$

Photo-absorption experiments can also help us measure the difference between the ground-state and excited state of N-particle system by measuring the energy of a photon that is absorbed by the system. The minimum energy difference of this process is called the optical or neutral gap and is given by;

$$\tilde{\Delta} = E_{total}^{exc}(N) - E_{total}^{gs}(N). \tag{3.7.3}$$

There also exist a scenario whereby if one ionizes the system in a photo-emission experiment, the absorbed photon can gain enough energy that propels it to leave the system. From the known energy of the photon and the measured energy of the escaping electron, we can determine its ionization potential (I);

$$I = E_{total}(N-1) - E_{total}(N). \tag{3.7.4}$$

From the data obtained from inverse photo-emission experiment we can also measure electron affinity (A);

$$A = E_{total}(N) - E_{total}(N+1). \tag{3.7.5}$$

The difference between ionization potential and electron affinity is defined as the fundamental gap (Δ);

$$\Delta = I - A. \tag{3.7.6}$$

There also exists a relationship between the chemical hardness of a material and fundamental gap, chemical hardness is twice the fundamental gap (2Δ). Nevertheless, orbital energy difference of a system can be expressed as;

$$\Delta = E_{HOMO} - E_{LUMO}, \tag{3.7.7}$$

where HOMO and LUMO are acronyms for highest occupied and lowest un-occupied molecular orbitals respectively. Optical gap ($\tilde{\Delta}$) is less than fundamental gap (Δ) by the binding energy of the resulting exciton in photo-absorption experiment [79, 80].

3.8 Green function and self-energy

This is suitable approach for studying excited-state properties of a material. To calculate Green function one requires the self-energy operator which is non-local and energy dependent. GW is derived systematically from many-body pertubation theory. If we measure kinetic energy of photoemitted electron along a certain direction **k** during photoemission experiment and apply the law of conservation of not only energy but also momentum, we obtain excitation spectrum E(**k**) of a solid [81].

$$\omega = K.E + E(\mathbf{k}). \tag{3.8.1}$$

From sudden approximation of photoemitted/probing electron proposed by Hedin and Lundqvist in 1969, spectrum is directly related to single-particle Green function provided the limit of kinetic energy is large enough.

$$iG(x,x^{'}) = \pm\langle N|T\left[\hat{\psi}(x)\hat{\psi}^{\dagger}(x')\right]|N\rangle, \tag{3.8.2}$$

for $t > t^{'}$ it bears the positive sign and negative for $t < t^{'}$, the above equation can then be simplified to give;

$$iG(x,x^{'}) = \begin{cases} \langle N|\hat{\psi}(x)\hat{\psi}^{\dagger}(x')|N\rangle, & \text{(electon, for } t > t'\text{)} \\ \langle -N|\hat{\psi}(x)\hat{\psi}^{\dagger}(x')|N\rangle, & \text{(hole, for } t^{'} > t\text{)} \end{cases},$$

where |N⟩ is the exact N-electron ground state, $\hat{\psi}(x)$ is a field operator in the Heisenberg representation which annihilates an electron at $x = (\mathbf{r}, t)$ and T is the time ordering operator. Physical interpretation of the Green function is that for $t^{'} > t$, it is the probability that a hole created at x will propagate to $x^{'}$ and for $t > t^{'}$, it is the probability that an electron added at $x^{'}$ will propagate to x.

Consequently, Green function describes photoemission processes and can give us information about one-electron excitation spectrum, expectation value of any single particle operator in the ground state and the ground state energy of a system [82]. Field operator can be used to express Heisenberg equation of motion as;

$$i\frac{\partial\hat{\psi}(x)}{\partial t} = \left[\hat{\psi}(x), \hat{H}\right], \tag{3.8.3}$$

where

$$\hat{H} = \int d^3r\hat{\psi}^{\dagger}(x)h_0(x)\hat{\psi}(x) + \frac{1}{2}\int d^3rd^3r'\hat{\psi}^{\dagger}(x)\hat{\psi}^{\dagger}(x')v(\mathbf{r}\text{-}\mathbf{r}'), \tag{3.8.4}$$

which gives equation of motion for Green function as;

$$\left[i\frac{\partial}{\partial t} - h_0(x)\right]G(x,x^{'}) - \int dx^{''}M(x,x^{''})G(x^{''},x^{'}) = \delta(x-x^{'}), \tag{3.8.5}$$

where h_0 is the sum of local external potential and kinetic energy operator and sum of self-energy and hartree potential gives mass operator (M) which can be defined as;

$$\int dx_1M(x,x_1)G(x_1,x^{'}) = -i\int d^3r_1v(\mathbf{r}\text{-}\mathbf{r}_1)\times\langle N|T\left[\hat{\psi}^{\dagger}(\mathbf{r}_1,t)\hat{\psi}(\mathbf{r}_1,t)\hat{\psi}^{\dagger}(\mathbf{r}_1,t)\hat{\psi}(\mathbf{r}^{'},t^{'})\right]|N\rangle. \tag{3.8.6}$$

The quantity on the right hand side of equation (3.8.6) gives a special case of a two-particle Green function (G_2);

$$G_2(1,2,3,4) = (i)^2\langle N|T\left[\hat{\psi}(1)\hat{\psi}(3)\hat{\psi}^{\dagger}(4)\hat{\psi}^{\dagger}(2)\right]|N\rangle. \tag{3.8.7}$$

For simplicity, we express ($\mathbf{r}_1$, t_1) as 1 and the same applies to co-ordinates 2, 3 and 4. If we apply the trick proposed by Schwinger in his functional derivative method to evaluate self-energy, we introduce time varying field ϕ(**r**,t) that will be used to evaluate self-energy [83]. This field will later be set to zero after obtaining self-energy. We can therefore express this field in Dirac notation as;

$$|\psi_D(\mathbf{r},t)\rangle = \hat{U}(t,t_0)|\psi_D(\mathbf{r},t_0)\rangle|, \tag{3.8.8}$$

where time development operator, $\hat{U}$ is expressed as;

$$\hat{U}(t,t_0) = T\exp\left[-i\int_{t_o}^{t} d\tau\hat{\phi}(\tau)\right], \tag{3.8.9}$$

and

$$\hat{\phi}(\tau) = \int d^3r\phi(\mathbf{r},\tau)\hat{\psi}_D^{\dagger}(\mathbf{r},\tau)\hat{\psi}_D(\mathbf{r},\tau). \tag{3.8.10}$$

Operators in Dirac and Heisenberg representation are related through the following equation;

$$\hat{\phi}(\mathbf{r},t) = \hat{U}^{\dagger}(t,0)\hat{\psi}_D^{\dagger}(\mathbf{r},t)\hat{U}(t,0). \tag{3.8.11}$$

Field operator ($\hat{\psi}_D$) should satisfy the following condition;

$$\frac{\partial\hat{\psi}_D}{\partial t} = \left[\hat{\psi}_D, \hat{H}(\phi=0)\right]. \tag{3.8.12}$$

We can then write Green function as;

$$iG(1,2) = \frac{\langle N^0|T\left[\hat{U}(\infty,-\infty)\hat{\psi}_D(1)\hat{\psi}_D^{\dagger}(2)\right]|N^0\rangle}{\langle N^0|\hat{U}(\infty,-\infty)|N^0\rangle}. \tag{3.8.13}$$

If we differentiate G in the above equation w.r.t ϕ, we obtain;

$$\frac{\delta G(1,2)}{\delta\phi(3)} = G(1,2)G(3,3^{\dagger}) - G_2(1,2,3,3^{\dagger}). \tag{3.8.14}$$

Applying equation (3.8.14) above for G_2 in equation (3.8.5) to define M, the term GG gives Hartree potential (V^H) which is related to M and Σ by;

$$\Sigma = M - V^H. \tag{3.8.15}$$

We can then re-arrange equation of motion for Green function to be;

$$\left[i\frac{\partial}{\partial t} - H_0(x)\right]G(x,x') - \int dx''\Sigma(x,x'')G(x'',x') = \delta(x-x'). \tag{3.8.16}$$

V^H, H_0, ψ and h_0 are related by;

$$H_0 = h_0 + V^H + \phi, \tag{3.8.17}$$

by applying identity gives;

$$\frac{\delta(G^{-1}G)}{\delta\phi} = G^{-1}\frac{\delta G}{\delta\phi} + \frac{\delta G^{-1}}{\delta\phi}G = 0, \tag{3.8.18}$$

implying that $\frac{\delta G}{\delta \phi} = -G\frac{\delta G^{-1}}{\delta \phi}G$, we can then evaluate $\frac{\delta G^{-1}}{\delta \phi}$ by using equation (3.8.16) as;

$$G^{-1} = i\frac{\partial}{\partial t} - H_0 - \Sigma, \tag{3.8.19}$$

to give;

$$\Sigma(1,2) = i\int d3d4G(1,3^{\dagger})\omega(1,4)\Gamma(3,2,4), \tag{3.8.20}$$

where Γ is vertex function. Screen (W) and bare (v) coulomb potential and inverse dielectric function (ϵ^{-1}) are related by;

$$W(1,2) = \int d3\epsilon^{-1}(1,3)v(3-2). \tag{3.8.21}$$

Inverse dielectric matrix measures the screening in the system [84] and is obtained as in classical theory by considering the change δV in the average potential due to a small variation $\delta\phi$ in the external potential and is given by $\epsilon^{-1}(1,2) = \frac{\partial V(1)}{\partial \phi(2)}$ where V is the sum of Hartree and external potential, $V = V^H + \phi$; vertex function can then be expressed as [85];

$$\begin{aligned}\Gamma(1,2,3) = -\frac{\delta G^{-1}(1,2)}{\delta V(3)} = \delta(1-2)\delta(2-3) + \frac{\delta\Sigma(1,2)}{\delta V(3)} \\ = \delta(1-2)\delta(2-3) + \int d(4567)\frac{\delta\Sigma(1,2)}{\delta G(4,5)}G(4,6)G(7,5)\Gamma(6,7,3).\end{aligned} \tag{3.8.22}$$

The derivative $\frac{\delta\Sigma}{\delta V}$ can be expressed as $(\frac{\delta\Sigma}{\delta G})/(\frac{\delta G}{\delta V})$ by applying chain rule which yields;

$$\frac{\delta\Sigma}{\delta V} = -G(\delta G^{-1}/\delta V)G. \tag{3.8.23}$$

Using above mentioned identity and definition of vertex function, we can fourier transform equation (3.8.16) with ϕ set to zero to obtain;

$$\left[\omega - H_0(\mathbf{r})\right]G(\mathbf{r},\mathbf{r}',\omega) - \int d^3r''\Sigma(\mathbf{r},\mathbf{r}'',\omega)G(\mathbf{r}'',\mathbf{r}',\omega) = \delta(\mathbf{r}-\mathbf{r}'). \tag{3.8.24}$$

From Dyson equation, if we want to calculate a given parameter X, we can derive a linear expression relating known parameter X_0 and X through kernel Y to give;

$$X = X_0 + X_0YX. \tag{3.8.25}$$

In this analogy, if G_0 is the Green function corresponding to $\Sigma = 0$, then we can have its Dyson equation as;

$$G = G_0 + G_0\Sigma G, \tag{3.8.26}$$

where the first term $G_0(1,2)$ is a direct propagation from point 1 to 2 without exchange-correlation interaction and Σ contains all possible exchange-correlation interactions with the system that an electron can move from 1 to 2. G_0 correspond to $H_0 = H^{Hartree} + V^{xc}$, hence we can re-arrange equation 3.8.26 as;

$$G = G_0 + G_0\Delta\Sigma G. \tag{3.8.27}$$

where $\Delta\Sigma = \Sigma - V^{xc}$ and V^{xc} is some local and energy-independent exchange-correlation potential.

3.9 Polarizability and response function

Total potential (V_{tot}) of a system can be expressed as the sum of external potential (V_{ext}) that arises from perturbation upon exposing a system to a photon and induced potential ($V_{induced}$).

$$V_{tot} = V_{ext} + V_{induced}. \tag{3.9.1}$$

As a solution to boson equation, we can express equation (3.9.1) as;

$$\delta V_{ind} = v\delta\rho, \tag{3.9.2}$$

where ρ is the induced charge. Dielectric function can be expressed as;

$$\epsilon = \frac{\delta V_{ext}}{\delta V_{tot}} = \frac{\delta(V_{tot} - V_{ind})}{\delta V_{tot}}, \tag{3.9.3}$$

which can be simplified as;

$$\epsilon = 1 - \frac{v\delta\rho}{\delta V_{tot}}. \tag{3.9.4}$$

Inverse dielectric function is given by;

$$\epsilon^{-1} = \frac{\delta V_{tot}}{\delta V_{ext}} = 1 + \frac{v\delta\rho}{\delta V_{ext}}. \tag{3.9.5}$$

However, linear response which gives change in total potential upon change in time varying field can be written as;

$$\chi = \frac{\delta\rho}{\delta V_{ext}} \Longrightarrow \epsilon^{-1} = 1 + v\chi. \tag{3.9.6}$$

Alternatively, we can express dielectric function using induced and total potential as;

$$\epsilon = \frac{\delta V_{ext}}{\delta V_{tot}} = \frac{\delta V_{tot} - \delta V_{ind}}{\delta V_{tot}}, \tag{3.9.7}$$

which can be simpilified to give;

$$\epsilon = 1 - \frac{v\delta\rho}{\delta V_{tot}}. \tag{3.9.8}$$

Polariability (P) which gives the change in the charge density upon a change in total (external + induced) field can be expressed as [81];

$$P = \frac{v\delta\rho}{\delta V_{tot}}, \tag{3.9.9}$$

$$\therefore \epsilon = 1 - vP. \tag{3.9.10}$$

Inverting equation (3.9.10), we obtain;

$$\epsilon^{-1} = [1 - vP]^{-1}. \tag{3.9.11}$$

Comparing equation (3.9.6) and (3.9.11) yields;

$$\chi = P + Pv\chi, \tag{3.9.12}$$

which can be re-arranged to give;

$$\chi = \frac{P}{1 - Pv}. \tag{3.9.13}$$

Equation (3.9.13) gives information of how a given system will respond when perturbed, which is the basis of optical excitation.

3.10 Hedin's equations

Hedin's equations are used to relate self energy (Σ), screened coulomb interaction (W), interacting Green function (G), non-interacting Green function (G_0), polarizability (P), vertex function (Γ) and bare coulomb potential (v) using a set of Dyson equations that are applied in GW approximation [86]. These equations are;

$$\Sigma(1,2) = i\int d(34)G(1,3^{\dagger})W(1,4)\Gamma(3,2,4). \tag{3.10.1}$$

$$G(1,2) = G_0(1,2) + \int d(34)G_0(1,3)\Sigma(3,4)G(4,2). \tag{3.10.2}$$

$$\Gamma(1,2,3) = \delta(1-2)\delta(2-3) + \int d(4567)\frac{\delta\Sigma(1,2)}{\delta G(4,5)}G(4,6)G(7,5)\Gamma(6,7,3). \tag{3.10.3}$$

$$W(1,2) = v(1,2) + \int d(34)v(1,3)P(3,4)W(4,2). \tag{3.10.4}$$

3.11 GW approximation

Hartree-Fock hamiltonian (h_{HF}) is given by;

$$h_{HF} = h + V_{ex}, \tag{3.11.1}$$

where exchange potential is expressed as;

$$V_{ex}(\mathbf{r},\mathbf{r}';\omega) = \frac{1}{|\mathbf{r}\text{-}\mathbf{r}'|}\frac{i}{2\pi}\int e^{i\delta\omega'}G_0(\mathbf{r},\mathbf{r}';\omega)d\omega'. \tag{3.11.2}$$

Zero-order Green function given by $G_0(\mathbf{r},\mathbf{r}';\omega)$ can be written as;

$$G_0(\mathbf{r},\mathbf{r}';\omega) = \sum_i \frac{\psi_i(\mathbf{r})\psi_i^*(\mathbf{r}')}{\omega - \varepsilon_i + i\delta sgn(\varepsilon_i - \mu)}, \tag{3.11.3}$$

where signum function (sgn) of a real number$(\varepsilon_i - \mu)$ is defined as;

$$sgn(\varepsilon_i - \mu) = \begin{cases} -1 & \text{if } (\varepsilon_i - \mu) < 0 \\ 0 & \text{if } (\varepsilon_i - \mu) = 0 \\ 1 & \text{if } (\varepsilon_i - \mu) > 0 \end{cases}.$$

As a comparison, Kohn-Sham (h_{KS}) and GW (h_{GW}) hamiltonians can be expressed as;

$$h_{KS} = h + V_{xc} \qquad\qquad h_{GW} = h + \Sigma_{GW}, \tag{3.11.4}$$

which can be written explicitly as;

$$\Sigma_{GW}(\varepsilon_i - \mu) = \frac{i}{2\pi}\int e^{i\delta\omega'}G(\mathbf{r},\mathbf{r}';\omega)W(\mathbf{r},\mathbf{r}';\omega-\omega')d\omega'. \tag{3.11.5}$$

Equation (3.11.5) can also be obtained if we fourier transform equation (3.10.4) from time to energy variables. We can then evaluate correlation part of self-energy for non-interacting G_0 as;

$$Im\Sigma^c(\mathbf{r},\mathbf{r}';\omega \leq \mu) = \pi \sum_{kn}^{occ} \psi_{kn}(\mathbf{r})\psi^*_{kn}(\mathbf{r}')Im\Sigma^c(\mathbf{r},\mathbf{r}';\varepsilon_{kn}-\omega)\theta(\varepsilon_{kn}-\omega), \tag{3.11.6}$$

and

$$Im\Sigma^c(\mathbf{r},\mathbf{r}';\omega > \mu) = -\pi \sum_{kn}^{unocc} \psi_{kn}(\mathbf{r})\psi^*_{kn}(\mathbf{r}')ImW^c(\mathbf{r},\mathbf{r}';\omega-\varepsilon_{kn})\theta(\omega-\varepsilon_{kn}), \tag{3.11.7}$$

where W^c is the difference between screened and bare coulomb interaction ($W^c = W - v$). This difference can be given in spectral representation as;

$$W^c(\mathbf{r},\mathbf{r}';\omega) = \int_{-\infty}^{0} d\omega' \frac{D(\mathbf{r},\mathbf{r}';\omega')}{\omega-\omega'-i\delta} + \int_{0}^{\infty} d\omega' \frac{D(\mathbf{r},\mathbf{r}';\omega')}{\omega-\omega'+i\delta}, \tag{3.11.8}$$

where D is proportional to imaginary part of W and defined to be antisymmetric in ω;

$$D(\mathbf{r},\mathbf{r}';\omega) = -\frac{1}{\pi} ImW^c(\mathbf{r},\mathbf{r}';\omega')sgn(\omega), \tag{3.11.9}$$

$$D(\mathbf{r},\mathbf{r}';-\omega) = -D(\mathbf{r},\mathbf{r}';\omega). \tag{3.11.10}$$

If $\Gamma(\mathbf{r},\mathbf{r}';\omega) = -\frac{1}{\pi} Im\Sigma^c(\mathbf{r},\mathbf{r}';\omega)sgn(\omega-\mu)$, then we can represent spectral function of correlation part of self-energy as;

$$\Sigma^c(\mathbf{r},\mathbf{r}';\omega) = \int_{-\infty}^{\mu} d\omega' \frac{\Gamma(\mathbf{r},\mathbf{r}';\omega')}{\omega-\omega'-i\delta} + \int_{\mu}^{\infty} d\omega' \frac{\Gamma(\mathbf{r},\mathbf{r}';\omega')}{\omega-\omega'+i\delta}. \tag{3.11.11}$$

We can further express real part of Σ^c as sum of two of its components, that is screened-exchange (SEX) term and coulomb-hole (COH) term as;

$$Re\Sigma = \Sigma_{SEX} + \Sigma_{COH}, \tag{3.11.12}$$

through which

$$Re\Sigma_{SEX}(\mathbf{r},\mathbf{r}';\omega) = -\sum_{i}^{occ} \psi_i(\mathbf{r})\psi^*_i(\mathbf{r}')ReW(\mathbf{r},\mathbf{r}';\omega-\varepsilon_i), \tag{3.11.13}$$

and

$$Re\Sigma_{COH}(\mathbf{r},\mathbf{r}';\omega) = \sum_{i} \psi_i(\mathrm{r})\psi^*_i(\mathbf{r}')P\int_{0}^{\infty} \frac{D(\mathbf{r},\mathbf{r}';\omega')}{\omega-\varepsilon_i-\omega'}. \tag{3.11.14}$$

$Re\Sigma_{COH}$ gives interaction energy of the quasi-particle with induced potential due to screening of electrons around it.

3.12 Bethe Salpeter Equation (BSE)

In Solid State Physics, BSE formalism is used to describe the electron-hole pair (i.e the exciton), which can be created when a system absorbs a photon. Ultimate goal of BSE is to determine a value of the microscopic dielectric function, which directly relates to some measurable quantity. It is aimed at determining absorption and electron-energy loss spectra which correctly describes important excitonic

effects [87]. This is attained by solving BSE for the two particle correlation function L that describes electron-hole interaction.

$$L(1,2,3,4) = -G_2(1,2,3,4) + G(1,3)G(2,4), \tag{3.12.1}$$

where G is one-particle Green function and G_2 is a two-particle Green function. Polarizability function is given by; $P(1,2) = -iL(1,2,1^{\dagger},2^{\dagger})$ and dielectric function, $\varepsilon(w) = 1 - vP(\omega)$. The two-particle Green function G_2 describes the propagation of two particles, L_o is the disconnected part that consists of two one-particle Green function.

$$L_o = iG(1,3)G(4,2). \tag{3.12.2}$$

L and L_o which stands for interacting and non-interacting two-particle correlation functions respectively, are related through the following expression;

$$L(1,2,3,4) = L_o(1,2,3,4) - G_2(1,2,3,4). \tag{3.12.3}$$

Since L satisfies a Dyson-like equation [88] then;

$$L(1,2,3,4) = L_o(1,2,3,4) + \int d5678 L_o(1,2,5,6)\left[v(5,7)\delta(5,6)\delta(7,8) + \chi(5,6,7,8)\right] L(7,8,3,4). \tag{3.12.4}$$

The standard approximation for interaction kernel, χ is given by;

$$\chi = \frac{i\delta\Sigma(5,6)}{\delta G(7,8)}. \tag{3.12.5}$$

Practically, BSE can be solved by diagonalizing a two-particle excitonic Hamiltonian which provides information about the excitonic eigenstates and eigenvalues as follows;

$$H^{2p,exc}_{(vc)(v'c')} A^{v'c'}_{\lambda} = E^{exc}_{\lambda} A^{v'c'}_{\lambda}. \tag{3.12.6}$$

Valence states are indicated by the indices $v, v^{'}$ while $c, c^{'}$ are used for conduction bands. If we consider only the resonant part of the excitonic Hamiltonian by allowing only positive frequency transitions to mix, we obtain macroscopic dielectric function which can be expressed as [89];

$$\varepsilon_M(w) = 1 - \lim_{q\to 0} v_o(q) \sum_{\lambda} \frac{|\Sigma(n_1,n_2)\langle n_1| \exp^{-iq.r} |n_2\rangle A^{(n_1n_2)}|^2}{E^{exc}_{\lambda} - w - i\eta}, \tag{3.12.7}$$

where $A^{(n_1n_2)}_{\lambda}$ and E^{exc}_{λ} are the eigenvectors and eigenvalues respectively, of the (resonant) two-particle Hamiltonian. Label n_i represents a couple of band and wave vector indices whereas Σ stands for self-energy.

3.13 Relationship between absorption coefficient and dielectric function of a material

Absorption coefficient determines how deep into a material light of a particular wavelength can penetrate before it is absorbed [90]. In a material with a low absorption coefficient, light is only poorly absorbed

and if the material is thin enough, it will appear transparent to that wavelength. Materials with higher absorption coefficients are more readily to absorb photons, which excite electrons into the conduction band [91]. The absorption coefficient (α) is related to the extinction coefficient (k) by the formula;

$$\alpha = \frac{4\pi k}{\lambda}. \tag{3.13.1}$$

Dielectric function of a material describes the electrical and optical properties verses frequency, wavelength or energy. It describes the polarisation and absorption properties of the material and is given by the following equation;

$$\sqrt{\varepsilon} = n + ik, \tag{3.13.2}$$

where n is refractive index and k the extinction coefficient as already stated. Frequency, wavelength and velocity of light are related by the formula $c = f\lambda$. If we substitute wavelength, equation (3.13.1) yields;

$$\alpha = \frac{4\pi k f}{c}. \tag{3.13.3}$$

After obtaining dielectric function that describes the interaction of photon with matter at the BSE level, we analyze it using well-known equations that relates the real and imaginary part of dielectric function in order to extract optical constants such as the absorption coefficient, extinction coefficient, refractive index, reflectivity and plasma frequency that in turn helps us determine if the materials under this study could be used in solar cell designs, opto-electronic devices, plasmonic applications to mention but a few.

3.14 Microscopic frequency dependent dielectric function

Total charge and current of a system can be expressed as the sum of external and induced quantities. Microscopic frequency dependent longitudinal dielectric constant $\epsilon_L(rr^{'},\omega)$ can be defined as;

$$\nabla . \int dr^{'} \epsilon_L(rr^{'},\omega) E^{tot}(r^{'},\omega) = 4\pi\rho^{ext}(r^{'},\omega). \tag{3.14.1}$$

where E^{tot} is the total external field and $\rho^{ext}(r^{'},\omega)$ is the external charge. The quantity on the right hand side of equation (3.14.1) can be written as;

$$4\pi\rho^{ext}(r^{'},\omega) = \nabla . E^{ext}(r^{'},\omega). \tag{3.14.2}$$

Substituting equation (3.14.2) onto equation (3.14.1) gives;

$$\int dr^{'} \epsilon_L(rr^{'},\omega) E^{tot}(r^{'},\omega) = E^{ext}(r^{'},\omega) + \nabla \times F(r^{'},\omega), \tag{3.14.3}$$

where $F(r^{'},\omega)$ is an arbitrary vector. For slowly varying external fields, inverse dielectric function $\epsilon^{-1}(r^{'},\omega)$ is given by;

$$E^{tot}(r^{'},\omega) = \int dr^{'} \epsilon^{-1}(r^{'},\omega) \left[E^{ext}(r^{'},\omega) + \nabla \times F(r^{'},\omega) \right]. \tag{3.14.4}$$

For cubic crystals $\left\langle \epsilon^{-1} \nabla \times F \right\rangle_0 = 0$ giving;

$$E^{tot}(q,\omega) = \epsilon_L^{-1}(q,\omega) E^{ext}(q,\omega), \tag{3.14.5}$$

implying that;

$$\epsilon_L(q,\omega) = \left\langle\left\langle \epsilon_L^{-1}(rr',\omega)\right\rangle\right\rangle_0^{-1}. \tag{3.14.6}$$

Equation (3.14.6) can be generalized as;

$$\epsilon_L(q,\omega) \neq \left\langle\left\langle \epsilon_L^{-1}(rr',\omega)\right\rangle\right\rangle_0^{-1}. \tag{3.14.7}$$

The difference between equation (3.14.6) and equation (3.14.7) is due to the local field effects that is connected to the absence of the continuous translation invariance present in the homogenous electron gas. If we impose the condition for plasma oscilation in the solid onto equation (3.14.6) we obtain;

$$\epsilon_L(q,\omega_p(q)) = Re\left[\epsilon_L(q,\omega_p(q))\right] + iIm\left[\epsilon_L(q,\omega_p(q))\right] = 0, \tag{3.14.8}$$

where $\omega_p(q)$ is the plasma frequency. Practically, a well-defined plasma oscilation occurs if $Re\left[\epsilon_L(q,\omega_p(q))\right] = 0$ and $Im\left[\epsilon_L(q,\omega_p(q))\right] << 1$. The latter condition implies that damping of the plasma is small.

3.15 Optical transitions

There are two kinds of photonic transitions namely interband transition and intraband transition. In the former, an electron makes a transition to a state in a different band whereas in the later, an electron makes a transition to a state in the same band. Intraband transition occurs only in metals, for semiconductors and insulators only the interband transition accounts for all possible transitions because every band is either fully occupied or fully unoccupied hence eliminating intraband transitions. For metallic systems, there exists a non-vanishing probability that an electron can be excited from one state below the Fermi level to a state above the Fermi level both belonging to one and the same band. Interband contribution to dielectric function which can further be split into direct and indirect transitions can be expressed as;

$$\epsilon_{inter}(\omega) = \epsilon_{inter}^{(1)}(\omega) + i\epsilon_{inter}^{(2)}(\omega), \tag{3.15.1}$$

is obtained directly from first principle calculations. The imaginary part of the dielectric function for interband transition is calculated by the following formula [92]:

$$\epsilon_{inter}^{(2)}(\omega) = \frac{e^2\hbar^2}{8\pi^3\epsilon_0 m_0^2}\sum_{m>n}\int \frac{\{f(E_{nk}) - f(E_{mk})\}\times|\langle mk|\hat{p}|nk\rangle|^2}{E_{mk,nk}\left(E_{mk,nk}^2 - \hbar^2\omega^2\right)}, \tag{3.15.2}$$

where f is the Fermi-Dirac distribution, $\hat{p}$ is the momentum operator and $E_{mk,nk} = E_{mk} - E_{nk}$ which is the energy difference between single-particle Bloch state. The real part is obtained from the Kramers-Kronig relation as [93];

$$\epsilon_{inter}^{(1)}(\omega) = 1 + \frac{2}{\pi}P\int_0^\infty \frac{\epsilon^{(2)}(\omega'')\omega'}{\omega'^2 - \omega^2 + i\eta}d\omega', \tag{3.15.3}$$

where P is the principal value of the integral and η is the small complex shift (CSHIFT) used to smoothen the spectrum. On the other hand, the intraband contribution is given by;

$$\epsilon_{intra}(\omega) = \epsilon_{intra}^{(1)}(\omega) + i\epsilon_{intra}^{(2)}(\omega) \tag{3.15.4}$$

which is calculated based on equation (3.15.5) and (3.15.6) below that depends on photon energy (ω), location of plasma frequency (ω_p) and the inverse of lifetime (γ) [94]. For the real part of dielectric function, intraband contribution is given by;

$$\epsilon^{(1)}_{intra}(\omega) = 1 - \frac{\omega_p^2}{\omega^2 + \gamma^2} \tag{3.15.5}$$

For the imaginary part of dielectric function, intraband contribution is given by;

$$\epsilon^{(2)}_{intra}(\omega) = \frac{\gamma\omega_p^2}{\omega^3 + \omega\gamma^2}. \tag{3.15.6}$$

Plasma frequency is expressed as [92];

$$\omega_p^2 = \frac{e^2}{8\pi^3\hbar^2\epsilon_0}\sum_n \int \left(\frac{\partial E_{nk}}{\partial K}\right)^2 \delta(E_{nk} - E_F)d^3k, \tag{3.15.7}$$

in which, E_{nk} is the energy eigenvalue of the Bloch state at n^{th} band at k point and E_F is the Fermi-level.

3.15.1 Drude term contribution to dielectric function at DFT level

All compounds studied in this work were found to be metallic hence Drude contribution was extracted. We will take a case study of in-plane dielectric function of VSe_2 since spectral behaviour in x-axis is similar to that in y-axis in order to give a brief outline of the process involved in incorporating intraband term to total part of dielectric function. From equation (3.15.7), plasma frequency depends primarily on the k-point among other parameters hence convergence was done though it was somehow challenging to obtain converged values of Drude plasma frequency. For VSe_2, in-plane Drude plasma frequency squared at DFT level is 16.095 eV when k-point grid of 16 16 7 whose k-point density is 16000 was found to have converged with respect to $\omega_D^2(eV)^2$ as shown in Figure 3.1 as well as summarized in Appendix B.

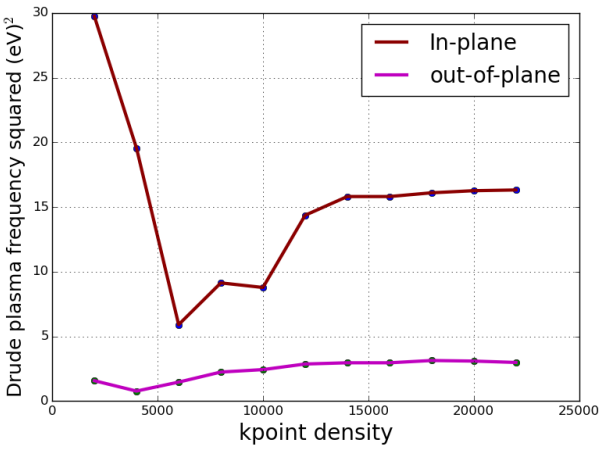


Figure 3.1: Convergence of the Drude plasma frequency squared of VSe_2 with respect to k-points at DFT level for both in-plane and out-of-plane

The converged value of $\omega_D^2(eV)^2 = 16.095$ eV for the in-plane was then substituted onto equation (3.15.5) and (3.15.6) with an inverse lifetime (γ) set to 0.01 eV in order to obtain intraband contribution to both real and imaginary part of dielectric function of VSe_2 as shown below. From equation (3.15.6), intraband contribution to dielectric function becomes infinite at $\omega = 0$ hence was excluded.

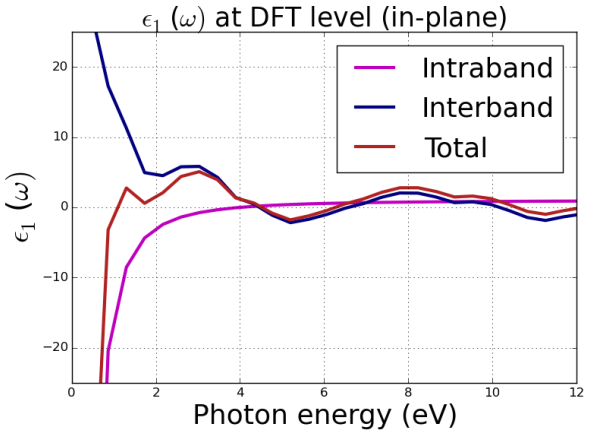


Figure 3.2: Real part of dielectric function of VSe_2 at DFT

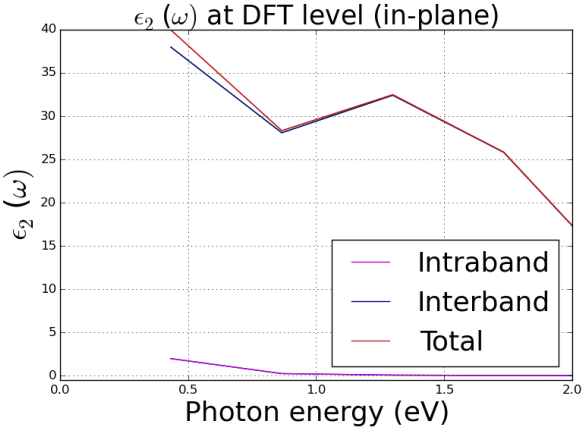


Figure 3.3: Imaginary part of dielectric function of VSe_2 at DFT

3.15.2 Drude term contribution to dielectric function at BSE level

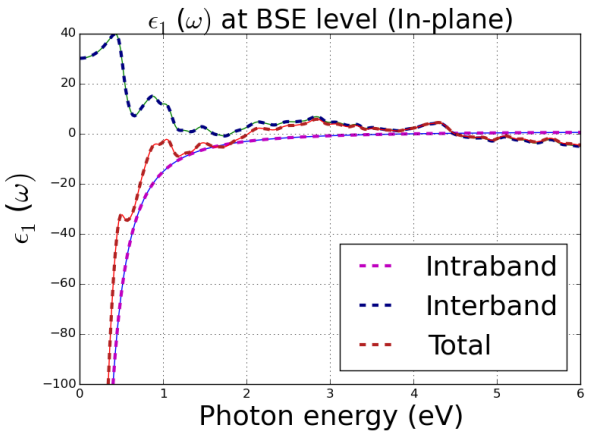


Figure 3.4: Real part of dielectric function of VSe_2 at BSE

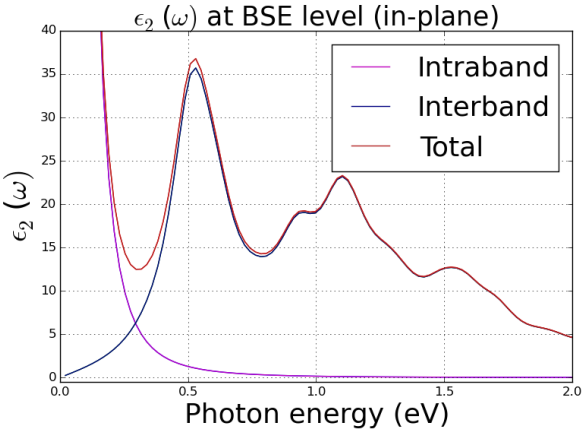


Figure 3.5: Imaginary part of dielectric function of VSe_2 at BSE

A point to note is that at very low photon energy ($0 < \omega \leq 1eV$) for imaginary part and ($0 < \omega \leq 3eV$) for real part of dielectric function at BSE level shown in Figure 3.4 and 3.5; it is evident that intraband contribution is important for better description of optical behaviour of metallic systems. In higher energy ranges, its contribution is negligible. Different energy ranges were considered for real and imaginary part of dielectric function in order to enhance clarity on the magnitude of contribution of intraband to total dielectric function.

It is also worth noting that technically, it is not possible to extract Drude intraband plasma frequency at BSE level in VASP. Hence, ω_D obtained after careful convergence at DFT level was applied in extracting intraband contribution to dielectric function at BSE level as an approximation with the condition that $\omega_D(DFT) \approx \omega_D(BSE)$ imposed. From literature, it is well known that DFT fails to give good optical results, hence in this study all optical constants i.e refractive index, absorption coefficient, extinction coefficient and reflectivity were analyzed at BSE level.

3.16 Plasmonic materials

A plasma is a medium with equal concentration of positive and negative charges, of which atleast one charge type is mobile [95]. This mobile charge is free to move in response to applied field and on average, is almost electrically neutral. This implies that ion and electron densities are nearly equal. Resolution in optical imaging systems is limited by the diffraction limit [96], a limit that arises because the near-field or evanescent components of the optical field that are needed to resolve sub-wavelength spatial information are not collected by the usual lens or mirror systems of optics. This is where plasmonics become necessary.

Plasmonics is a field that incorporate optics onto nanotechnology [97]. As already mentioned, optics does not naturally fit onto the nanometer world because of the fact that the diffraction limit hinders the length scales that can be probed to an order of several hundred nanometers [98]. Plasmonics help miniaturize optical components and integrate them on-chip while leveraging on the large bandwidth of light. Plasmonic devices generally require metallic components which possess abundant electrons. Plasmonics has seen an exponential growth, due mainly to the sheer diversity of applications, from optical cloaking to superlensing as well as single molecule surface enhanced raman spectroscopy, parasite therapy and optical circuits with high speed optical switching [99]. Plasmonic materials may also revolutionize the lighting industry by making light emitting diodes bright enough to compete with incandescent bulbs [100]. LEDs have several advantages over incandescent and fluorescent lamps, including high reliability, long lifetime and high efficiency.

A characteristic frequency at which the material changes from a metallic to a dielectric response is called the plasma frequency (ω_p), at this frequency the real part of dielectric function vanishes to zero [101].

From connection between optical and electrical properties of a solid through conductivity tensor, transparent materials are expected to be reasonably poor electrical conductors while highly reflecting materials are expected to be reasonably good electrical conductors [101]. On the other hand, there is a possibility that a material can have its plasma frequency just below the visible frequencies. This implies that it will be a good electrical conductor yet transparent at visible frequencies [102]. It is important to mention that there exist a relationship between steepness of the dip at plasma frequency and relaxation time, the longer the relaxation time, the sharper the plasma structure.

Relaxation time is basically the amount of time in which electrons are accelerated before undergoing next collision. In an experimental set up, relaxation time is affected by purity, crystal quality of metal and temperature [102]. In metals, plasma frequencies are typically in the visible to ultra-violet for high density metals. For low density metals and doped semiconductors, it is in the infrared or far-infrared. Metals are opaque and highly reflective below the plasma frequency and become transparent above ω_p [102].

The following are conditions to be fulfilled by a metal in order to be used as a plasmonic material. It should have high plasma frequency of about 9 eV, low total damping rate Γ that translates to high mean

relaxation time of conduction electrons (for silver, $\Gamma = 0.02$) and it should show high chemical stability in many enviroments. Cost, figure-of-merit (which is given by the expression $[Re(\epsilon_m)]^2/Im(\epsilon_m)$ where ϵ_m is the permittivity of the plasmonic material [103]), as well as ease of processing and feasibility of integration should also be put into consideration. Silver, gold, copper and aluminium are used in most plasmonic applications. Silver and copper are known to degrade in air whereas gold is stable in air [104]. However, copper forms a native oxide layer in air whereas silver is sensitive to sulfidation and tarnishes to form a layer of silver sulfide, which results in an increase in optical loss. This automatically transform to large values of the imaginary part of dielectric function.

Generally, metals often degrade upon exposure to air or oxygen or even humidity and this might pose additional problems in their plasmonic integration. In real materials, the plasma frequency is shifted from the bare plasma frequency due to screening by interband transitions, which are single particle excitations from the valence to conduction bands (screened plasma frequency in silver is 3.8 eV compared to the bare plasma frequency value of 9.6 eV) [99]. We can express the dielectric function of a material according to Drude model as;

$$\epsilon(\omega) = \epsilon_1(\omega) + i\epsilon_2(\omega) = \epsilon_{int} - \frac{\omega_p^2}{\omega(\omega + i\Gamma)}, \tag{3.16.1}$$

where ϵ_{int} is the contribution due to interband transitions and is unity for perfectly free electron gas, damping factor $\Gamma = \frac{1}{\tau}$ where τ is the mean relaxation time of conduction electrons, ω_p is plasma frequency. For bulk plasma, plasma frequency is defined as;

$$\omega_p^2 = \frac{4\pi n e^2}{m^\star}, \tag{3.16.2}$$

where n is the conduction electron density, $m^\star$ is the effective optical mass of conduction electrons and e is charge of an electron. The above expression can further be re-written as;

$$\omega_p^2 = \frac{n e^2}{\epsilon_0 m^\star}. \tag{3.16.3}$$

Optical performance of a metal for many plasmonic applications is dictated by relative position of plasma frequency [105]. One of the limiting factors in all plasmonics is loss, which arises due to many processes such as radiative damping, electron confinement, structural imperfections and metal heating losses [106].

4

COMPUTATIONAL DETAILS

4.1 Outline of calculation

All calculations were performed using the VASP code [107] that is based on density functional theory which solves Kohn-Sham equations using projector augmented wave method. In this formulation, the interaction between ions and electrons is described using a soft pseudopotential [108] which allows energy convergence with relatively small number of plane waves. The generalized gradient approximation in the scheme of Perdew-Burke-Ernzerhof was adopted for the exchange correlation functional. Ionic relaxation was done using conjugate gradient minimization method [109], to minimize the Hellman-Feynman forces among the constituent atoms. Grimme DFT-D2 [77] and Tkatchenko-Scheffler [110] method long range van der Waals corrections were used to account for inter-layer attraction in layered systems. The cut-off energy for the plane wave basis and self-consistent convergence criteria threshold were set at 700 eV and 1×10^{-8} eV respectively [111]. A k-point density of 1000 per atom in the reciprocal space was used ensure k-point convergence unless otherwise stated. This means for a material that had 3 atoms in the unit cell i.e VSe_2, the number of divisions for k-points was 3000.

Phonon dispersion curves were obtained using linear response method and some done using finite displacement method as implemented in PHONOPY code [112]. To obtain accurate optical properties, a three-stage calculation was done. In the first stage, a DFT calculation was performed, which enabled us to obtain the electronic structure of materials of interest by solving Kohn-Sham equations. In the second stage, a GW calculation based on input from the DFT calculation was undertaken, from which quasi-particle energies were computed. At this stage the Kohn-Sham exchange correlation potential (V_{xc}) was effectively replaced by energy dependent electron self-energy. Self-consistent GW_0 calculation was done in which only G (Green function) was iterated keeping W (screened coulomb interaction) fixed at its initial DFT value. In the third stage, a Bethe-Salpeter Equation (BSE) calculation that was based on GW data was performed to determine optical absorption spectra which considers excitonic effects. At this level of approximation, electron-hole interactions are included in order to improve the description of optical properties.

4.2 Work flow

As stated above, this study was carried out using VASP which is an acronym for Vienna Ab initio Simulation Package developed by George Kresse and co-workers in Vienna, Australia [113–115]. Input files of materials of interest are INCAR (a central input file of VASP that determines what is to be calculated and how it should be done); KPOINTS (determines the k-points setting) and POSCAR (contains ionic positions). They were obtained from materials project database and carefully manipulated to adopt the above mentioned criteria of cut-off energy and k-point grid density. POTCAR files (that contains pseudopotentials) were later generated from existing POSCAR using pymatgen tool [116]. Volume optimization was then carried out in which the initial structure was subjected to uniform scaling resulting in thirteen volumes. At each volume, partial relaxation was done, whereby, atomic positions and cell shapes were allowed to relax at a constant volume [117]. By fitting the obtained data of volume and total energy onto third order Birch-Murnaghan equation of state [118], we deduced the energetically favoured ground state structure of each compound of interest. Cohesive and formation energy were then obtained for relaxed ground state structure as well as full set of lattice constants in addition to volume of the cell.

After determining the preferred ground state polymorph, careful mechanical study was initiated to compute elastic constants whereby the resulting stiffness matrix was then fed onto the online elastic tensor analysis tool [119] to extract mechanical properties data of the compound at hand. These include; eigenvalues, Poisson's ratio, bulk, shear and Young's modulus. They were established from three averaging schemes namely Voight, Reuss and Hill. Born stability criterion were then cross checked to confirm its mechanical stability. Phonon studies were done using PHONOPY code, in conjuction with VASP to predict if only hard modes or both hard and soft modes exist in the material which enables one to check its dynamical stability. For polymorphs that met the energy stability test based on cohesive and formation energy, dynamical stability test based on phonons and mechanical stability test based on elastic constants; band structure calculations were done to gauge if the material is metallic, semiconducting or insulating. Further, GW and BSE computation was carried out at the end to get better description of the complex dielectric function, which enabled extraction of optical constants based on Kramer-Kronig relations [120]. Figure 4.1 is a schematic diagram showing step by step computation from DFT to BSE.

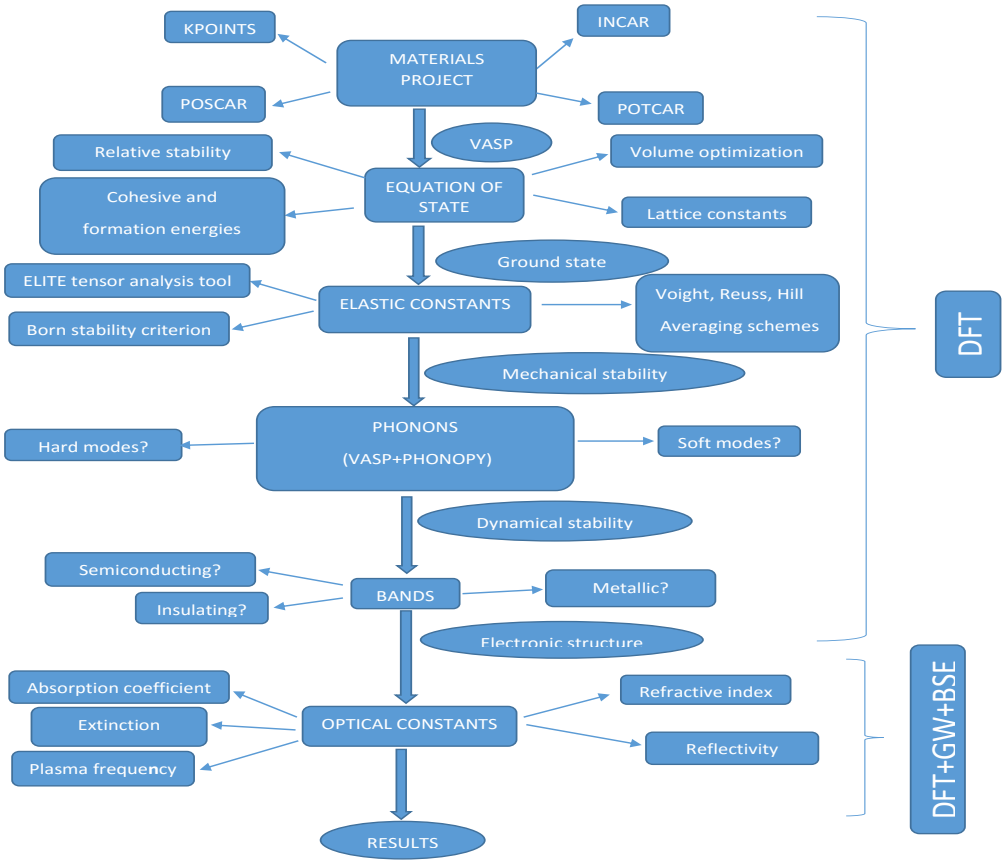


Figure 4.1: Work flow

4.3 Convergence test

This is a procedure used in computer simulation to establish an appropriate value of parameter under study. It is achieved by increasing its value until the result stops changing. It is a feature applicable to plane wave basis set where accuracy of computed results is controlled by a single parameter as compared to localised basis set. Convergence of the total ground state electronic energy and other energy-related parameters in VASP or any other computational code depends on two parameters namely the cut-off energy used to fix the number of plane waves in the basis set and k-spacing (k-points). Spending some time to investigate these two parameters could lead to an overall increase in computational efficiency without compromising the accuracy of the obtained numerical results.

4.3.1 K-points convergence

The objective of k-points convergence is to find a sufficiently dense mesh for integrating the first Brillouin zone. The latter is defined to be the Wigner-Seitz primitive cell of the reciprocal lattice or simply a set of points in the *k* space that can be reached from the origin without crossing any Bragg plane [121]. Reciprocal lattice gives information about periodicity of lattice in reciprocal units. Reciprocal space is often used than real space in diffraction to characterize materials. This is because diffraction occurs in inverse proportion to the spacing between objects causing diffraction. The Figure 4.2 shows Brillouin zone (BZ) of hexagonal VS_2 along high symmetry points (Γ-M-K-Γ-A-L-H-A-L-M-K-H), where a*, b* and c* represent reciprocal lattice vectors.

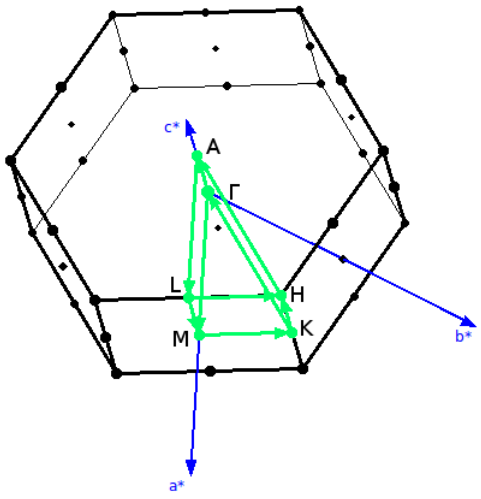


Figure 4.2: An example of BZ

The first Brillouin zone is often used to depict all of the Bloch states without redundancy for periodic medium. Brillouin zone was sampled using Monkorst Pack method [122]. For hexagonal structures, Gamma (Γ) centered grid was used due to symmetry consideration. Appropriate grid size was used depending on the nature of the structure at hand. This study involved metallic systems, hence required an order of magnitude more k-points than semi-conducting and insulating counterparts [123]. A point to note is that all optical calculations were done using Gamma centered grids for both hexagonal and non-hexagonal structures.

4.3.2 Cut-off energy convergence

Cut-off energy is an arbitrary minimal value of energy. We always have to ensure cut-off energy is high enough to give accurate computational results. However, as the case of k-points, there is an optimum point beyond which further change in cut-off energy brings about no appreciable change in parameter under study. An example of cut-off energy convergence with respect to some elastic coefficients for trigonal VS_2 is shown in Figure 4.3. It is noticeable that cut-off energy below 600 eV was insufficient to obtain converged values of elastic coefficients.

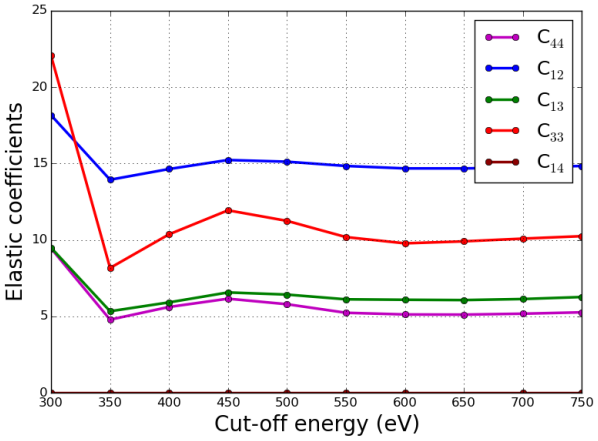


Figure 4.3: cut-off energy convergence for trigonal VS_2

4.4 Equation of state

Equation of state is a constitutive expression that gives a mathematical relationship between two or more state variables associated with a material i.e its internal energy, volume, pressure, temperature etc. It is applicable in describing properties of solids, fluids and even mixtures of fluids where we invoke an appropriate mixing rule. Generally, it is semi-empirical in nature. In our study, we applied third order Birch-Murnaghan equation of state [118] that is based on Taylor series expansion of pressure in terms of an Eulerian strain (f); internal pressure is a measure of how the internal energy of a system changes when it expands or contracts at constant temperature. It is a partial derivative of internal energy with respect to volume at constant temperature [124]. At absolute zero the entropy of a system is constant, so that the thermodynamic identity ∂E = -P∂V is the change in energy accompanying a change ∂V in volume [125], which can be re-arranged as;

$$P = -\frac{\partial E}{\partial V}. \tag{4.4.1}$$

If we apply chain rule, we can rewrite pressure as;

$$P = -\left(\frac{\partial E}{\partial f}\right)\left(\frac{\partial f}{\partial V}\right), \tag{4.4.2}$$

that can be written in terms of bulk modulus and Eulerian strain as;

$$P(f) = 3B_o f\left(1+2f\right)^{\frac{5}{2}}\left[1+\frac{3}{2}\left(B_o^{'}-4\right)f+\ldots\right]. \tag{4.4.3}$$

Eulerian strain is expressed in terms of reference and equilibrium volume as;

$$f = \frac{1}{2}\left[\left(\frac{V}{V_o}\right)^{\frac{-2}{3}} - 1\right]. \tag{4.4.4}$$

Substituting equation (4.4.4) onto equation (4.4.3) we obtain;

$$P(V) = \frac{3}{2}B_o\left[\left(\frac{V_o}{V}\right)^{\frac{7}{3}} - \left(\frac{V_o}{V}\right)^{\frac{5}{3}}\right]\left\{1 + \frac{3}{4}\left(B_o^{'} - 4\right)\left[\left(\frac{V_o}{V}\right)^{\frac{2}{3}} - 1\right]\right\}, \tag{4.4.5}$$

where V, V_o, B_o and $B_o^{'}$ are reference volume, equilibrium volume, bulk modulus and derivative of bulk modulus with respect to pressure respectively.

Bulk modulus is proportional to the curvature of the equation of state at the equilibrium volume together with its derivative are higher order derivatives of energy function and are related through;

$$B_o = -V\left(\frac{\partial P}{\partial V}\right)_{V=V_o} = V\left(\frac{\partial^2 E}{\partial V^2}\right)_{V=V_o}, \tag{4.4.6}$$

$$B_o^{'} = \left(\frac{\partial B_o}{\partial P}\right)_{V=V_o} = \frac{\partial}{\partial P}\left(V\frac{\partial^2 E}{\partial V^2}\right)_{V=V_o}. \tag{4.4.7}$$

Bulk modulus is a coefficient of elasticity of a substance that is expressed as the ratio between pressure that acts to change the volume of the substance and the fractional change in volume produced [126] whereas $B_o^{'}$ is a dimensionless parameter. As a norm, in *ab initio* study we often express energy as a function of volume. This is attained by intergrating equation (4.4.5) with respect to volume, which yields;

$$E(V) = E_o + \frac{9V_oB_o}{16}\left\{\left[\left(\frac{V_o}{V}\right)^{\frac{2}{3}} - 1\right]^3 B_o^{'} + \left[\left(\frac{V_o}{V}\right)^{\frac{2}{3}} - 1\right]^2\left[6 - 4\left(\frac{V_o}{V}\right)^{\frac{2}{3}}\right]\right\}, \tag{4.4.8}$$

where V_o is the equilibrium volume of the system under study.

4.4.1 Non-spherical atom correction energy

In this study, in order to apply equation of state as expressed in equation (4.4.8), we had to subtract correction energy for non-spherical atoms manually from the total energy obtained in OSZICAR file for each atom for all volumes considered before plotting the equation of state. This is because by default, VASP calculates only the spherical contribution from the gradient corrections inside the PAW spheres. Thereafter, by fitting corrected volume-energy data onto the above Birch-Murnaghan equation of state, we obtained the equilibrium lattice parameters. Non-spherical atom correction energies used for PBE functional for each element considered in this study are provided in Table 4.1.

Table 4.1: Non-spherical atom correction energies

Element	Vanadium	Niobium	Sulphur	Phosphorus	Selenium	Tellurium
Correction energy (eV)	-3.3152551	-3.1171561	-1.0776041	-1.8895267	-0.89447059	-0.73063186

4.5 Phonons

A phonon is a quantized mode of vibration occurring in a rigid crystal lattice such as atomic lattice of a solid. Phonons play an important role in many of the physical properties of solids such as thermal and electrical conductivity [127]. At equilibrium, a crystal is dynamically stable if its potential energy always increases against any combinations of atomic displacements. In addition, vibrational properties of a crystal determine a wide range of macroscopic behaviour like specific heat, sound velocity and infrared and Raman absorption [128]. Analysis of the forces associated with a systematic set of displacements provides a series of phonon frequencies. In the harmonic approximation, this is equivalent to the condition that all phonons have real or positive frequencies. Presence of imaginary frequencies indicates instability hence phonon dispersion curves can also help us gauge dynamical stability of a material [129]. The problem of lattice dynamics is to find the normal modes of vibration of a crystal. It seeks to calculate the energies or frequencies (ω) of the phonons as a function of their wave vector. Even if the total energy of a structure can be minimized, its stability cannot be assured hence phonon calculation is done to provide test for dynamical stability of a given structure. Using *ab initio* approach, we can calculate vibrational frequencies of a material using either linear response method or finite displacement method.

4.5.1 Linear response method

In this technique, first order change in charge density and potential gives rise to second order change in energy. It is analogous to conventional DFT calculation but instead with derivatives of potential, wave-functions and charge expressed with respect to atomic displacements. It is computationally economical since it takes advantage of periodic perturbation by calculating force constant at a single wave vector (Γ), which is then fourier transformed to give projections for other wave vectors.

4.5.2 Finite displacement method

The convenience of this technique is that the number of displacements to be evaluated in order to construct dynamical matrix can be reduced by symmetry. This implies that only symmetry inequivalent displacements are considered and the remainder of the Hessian matrix [130] is filled using symmetry considerations. Displacements with a very small magnitude often give results that are similar to the linear response. Its advantage is that one can investigate phonon anharmonicity by increasing the amplitude of displacements. In most of the compounds considered in this study, phonon calculation was undertaken in high symmetry directions using $2 \times 2 \times 2$ supercell, with varying number of atoms for each compound. In varying the size of the cell, one needs to re-adjust the number of k-points in the irreducible part of the brillouin zone. In this regard, Aflow was used. Aflow is a method for high-throughput computational materials design, that automates calculations using ab initio electronic structure methods (such as setting density of k-point grid in VASP). It can calculate physical properties such as; relaxed geometries, electronic and phonon band structures, magnetic properties and thermodynamic properties [131] .

4.6 Cohesive and formation energy

4.6.1 Cohesive energy

This is the energy that must be supplied to the solid to separate its constituents into neutral free atoms at rest and at infinite separation. The calculation of the cohesive energy requires a value of the total energy for the solid and of the free atoms. The energy calculations for both product (compound) and reactants (constituent atoms) have to be performed at the same level of accuracy in order to attain precise value for cohesive energy (E_{coh}) [132].

$$E_{coh} = E_{MX_2}^{solid} - \left[E_M^{solid} + E_{2X}^{solid}\right], \tag{4.6.1}$$

where $E_{MX_2}^{solid}$ is energy of compound whereas E_M^{solid} and E_{2X}^{solid} are energies of constituents elements, that is transition metal and chalcogen or pnictogen respectively.

4.6.2 Formation energy

This is the difference between cohesive energy of products, E_{coh} (products) and cohesive energy of reactants, E_{coh} (reactants). Chemical reactivity equation of MX_2 compounds considered in this study is given by equation (4.6.2), where one mole of transition metal (M) reacts with two moles of either chalcogen or pnictogen (X);

$$M(s) + 2X(s) \longrightarrow MX_2(s). \tag{4.6.2}$$

Their formation energies can then be expressed as:

$$E_F = \sum E_{coh}(products) - \sum E_{coh}(reactants), \tag{4.6.3}$$

or

$$E_F(MX_2) = E_{coh}(MX_2) - \left[\frac{E_{coh}(M) + 2E_{coh}(X)}{3}\right]. \tag{4.6.4}$$

From equations (4.6.1) and (4.6.4), negative values cohesive and formation energies will indicate that the compound is stable against decomposition into its constituent atoms and elemental solids.

4.7 Ab initio calculation of elastic constants

Basis for elastic constant calculation relies on generalized Hooke's law (see Appendix A). Elastic costants are important for understanding the response of material when subjected to small strains and perceiving the relationship between crystal structure and bonding. They define the behaviour of a material that undergoes stress, deforms, and then recovers and returns to its original shape after stress ceases. Thus, the elastic behavior plays an important role in understanding the structural stability [133]. There is also a tendency towards correlation between elastic constants and melting temperature of a solid [134]. Elastic constants for single crystals are obtained by straining the lattice by distorting the primitive vectors and allowing it to relax all the internal parameters in order to minimize the total energy [135]. In principle, we can compute elastic constants using two ways in *ab initio* methods namely the energy-strain approach and the stress-strain approach.

4.7.1 Energy-strain approach

Energy-strain approach is based on the computed total energies of properly selected strain states of the crystal. The crystal is strained in order to obtain corresponding stiffness values preserving as much symmetry as possible. For each strain type, several magnitudes of strains are applied and the corresponding total energies computed. Stiffness is then derived from the curvature of energy-strain relation. Some of the imposed strains may be related to a single elastic constant while others are described as a linear combination from which elastic constant tensor is evaluated. The number of independent elastic constants in a material which depends as well on lattice symmetry and point type determines the number of neccesary distortions.

4.7.2 Stress-strain approach

Stress-strain approach relies on the feature of VASP to directly calculate the stress tensor. The elastic tensor is determined by performing six finite distortions of the relaxed unit cell and deriving elastic constants from the stress-strain relationship. A point worth noting is that, within the stress-strain approach, just one evaluation is in principle, sufficient to obtain elastic constants whereas within the energy-strain approach, several magnitudes of strain have to be evaluated in order to obtain elastic constants from an analytic fit to the total energy data. Moreover, the discussion above applies to single crystals (one single block where all the symmetry operations of the structure are valid for the whole block). For polycrystalline materials (those that consists of single crystals but of very small sizes of order of micrometers but randomly distributed such that there is no preferred orientation), we derive its elastic moduli by macroscopic averaging. There are several averaging schemes used to derive elastic moduli for polycrystalline materials from its single crystal elastic constants.

In this work, we used stress-strain approach. After extracting our stiffness matrix, it was analyzed using online elastic tensor analysis tool (ELATE) developed by Gaillac and Coudert [119] to obtain average properties (of bulk, Young's and shear modulus together with Poisson's ratio), eigenvalues of the stiffness matrix and variations of the elastic moduli among other mechanical properties. Elastic constants can also be used to gauge how mechanically stable a material is, to do so we applied the so called Born stability criteria [136] which are necccesary and sufficient conditions that a material has to fulfil for us to classify it as either stable or unstable. Moreover, Voight, Reuss and Hill averaging schemes (discussed in Appendix A) were used to calculate bulk modulus, shear modulus and Poisson's ratio among other mechanical properties of materials.

4.8 Optical constants

Optical properties of a material determine the interaction with electro-magnetic radiation in the visible range. Measurable quantities such as the index of refraction or the reflectivity and their spectral variations are used to characterize materials. Optical methods are among the most important tools for elucidating the electron structure of matter. After obtaining dielectric matrix at BSE level, we derived reflectivity R(ω), absorption $\alpha(\omega)$, refractive index n(ω), energy loss L(ω) and extinction coefficient k(ω) from real $\epsilon_1(\omega)$ and imaginary part $\epsilon_2(\omega)$ of the dielectric function as per the following equations [137];

$$n(\omega) = \frac{1}{\sqrt{2}} \left[\sqrt{\epsilon_1^2(w) + \epsilon_2^2(w)} + \epsilon_1(w) \right]^{\frac{1}{2}}. \tag{4.8.1}$$

$$\alpha(\omega) = \sqrt{2(w)}\left[\sqrt{\epsilon_1^2(w) + \epsilon_2^2(w)} - \epsilon_1(w)\right]^{\frac{1}{2}}. \tag{4.8.2}$$

$$k^2(\omega) = \frac{1}{2}\left[\sqrt{\epsilon_1^2(w) + \epsilon_2^2(w)} - \epsilon_1(w)\right]. \tag{4.8.3}$$

$$L(\omega) = \frac{\epsilon_2(w)}{\left[\epsilon_1^2(w) + \epsilon_2^2(w)\right]}. \tag{4.8.4}$$

$$R(\omega) = \left|\frac{\sqrt{\epsilon_1(w) + j\epsilon_2(w)} - 1}{\sqrt{\epsilon_1(w) + j\epsilon_2(w)} + 1}\right|. \tag{4.8.5}$$

Real part of dielectric function signifies polarization response whereas imaginary part denotes the optical loss. Reflectivity can also be written in terms of refractive index and extinction coefficient as;

$$R(\omega) = \frac{(n-1)^2 + k^2}{(n+1)^2 + k^2}. \tag{4.8.6}$$

In this study, equations (4.8.1), (4.8.2), (4.8.3) and (4.8.5) were applied. It should also be observed that these equations are only valid if measured at the same wavelength since they are wavelength dependent and can only represent optically isotropic material, in case of an anisotropic media, the dielectric constant becomes a matrix [138]. These constants are functions of wavelength, frequency, energy and physical states such as physical density, crystallinity, grain size and orientation.

As already stated in section 3.13, absorption coefficient $\alpha(\omega)$ determines how far into a material light of a particular wavelength can penetrate before it is absorbed. The refractive index n(ω) of a substance is the ratio of speed of light in vacuum to its speed in the material under study. In metals, free carrier effects are almost always studied by reflectivity techniques due to high optical absorption of metals at low frequencies. Energy loss in metals is attributed to electronic transitions. Extinction coefficient is given by the sum of scattering and absorption of the electromagnetic waves going through the sample. In semiconductors, free carrier effect is usually more accurately described using absorption techniques. Optical loss mechanisms are interband transitions, intraband transitions and scattering losses due to presence of defects. All these optical properties helps us determine if for instance, a material can be used in solar cell designs. Many device applications in semi-conductor lasers and light-emitting diodes (LEDs) rely on specific optical responses of a material.

5

RESULTS AND DISCUSSION

In this chapter, we report numerically obtained structural, mechanical, dynamical, electronic and optical properties of transition metal dipnictogenides (NbP_2 and VP_2) that are non-layered and transition metal dichalcogenides (NbS_2, $NbSe_2$, $NbTe_2$, VS_2, VSe_2 and VTe_2) that are layered. For layered TMDs, Grimme DFT-D2 and Tkatchenko-Scheffler (TS) were applied to account for interlayer van der Waals interaction.

5.1 Niobium diphosphide

Relative study of NbP_2 was not conducted since only one polymorph with a monoclinic configuration has been observed experimentally.

5.1.1 Structural properties of NbP_2

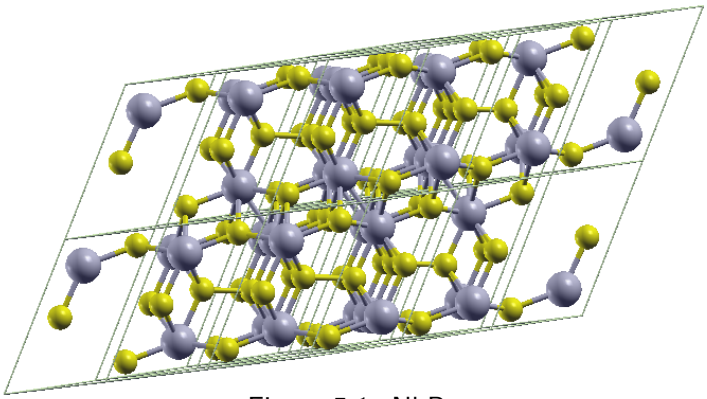


Figure 5.1: NbP_2

Figure 5.1 shows crystal structure niobium diphosphide, where larger atoms are niobium and the smaller ones phosphorus. VP_2 exhibit similar atomic arrangement as NbP_2. Acquired numerical values of lattice parameters and volume are shown in Table 5.1, symmetry check using AFLOW [131] was carried out which confirmed NbP_2 is monoclinic. Proper structural determination of a given material is critical for understanding its properties and functionalities.

Table 5.1: Structural and energetic properties of NbP_2

	a(Å)	b(Å)	c(Å)	$\alpha(^\circ)$	$\beta(^\circ)$	$\gamma(^\circ)$	$V_0(Å)^3$	E_{coh}(eV/atom)	E_{form}(eV/atom)	Z
Calc	8.963	3.297	7.601	90	119.13	90	196.24	-5.3525	-0.6827	4
Exp [35]	8.878	3.266	7.529	90	119.13	90	190.70	-	-	4

Calculation of the above structural, energetic parameters and other properties of NbP_2 were purely done using PBE since NbP_2 is not layered. Computed structural parameters were comparable to experimental ones as shown in Table 5.1. The cohesive and formation energies obtained were both negative, indicating that NbP_2 is stable against decomposition into its constituent atoms and elemental solids. Throughout this study, cohesive and formation energies are in eV per atom, values of mechanical properties are given in gigapascals (Gpa) and Z stands for the number of formula units per unit cell.

5.1.2 Mechanical properties of NbP_2

The Table 5.2 below shows the calculated values of independent elastic coefficients for NbP_2. Bulk modulus, Young's modulus, shear modulus and Poisson's ratio are expressed using B, E, G and ν notation respectively as presented in Table 5.3. Eigenvalues of stiffness matrix for all compounds considered are also available in Appendix B.

Table 5.2: Calculated values of independent elastic coefficients

C_{11}	C_{12}	C_{13}	C_{15}	C_{22}	C_{23}	C_{25}	C_{33}	C_{35}	C_{44}	C_{46}	C_{55}	C_{66}
382.83	60.70	105.80	-6.83	276.81	91.23	11.90	281.18	4.47	145.89	28.08	106.82	95.77

Table 5.3: Calculated B, E, G, ν and B/G

	B	E	G	ν	B/G
Voight (V)	161.81	279.39	115.24	0.2122	1.40
Reuss (R)	158.61	264.05	107.99	0.2225	1.47
Hill (H)	160.21	271.74	111.61	0.2173	1.44

Three averaging schemes were adopted in computing B, G, E and ν namely Voight, Reuss and Hill methods. They are significant for making comparison and checking accuracy of the computed values. Elastic constants of NbP_2 fulfilled all the Born Stability conditions for monoclinic structures and predicted eigenvalues were all positive implying that it is mechanically stable. Furthermore, from the elastic constants, Zener anisotropy factors (A_1, A_2, A_3) extracted [139] were all different from one, consistent with the anisotropy of NbP_2. Bulk, shear and Young's moduli were calculated via well-known combination of some specific elastic coefficients [140] which varies from one crystal system to another.

Bulk modulus (B), describes volumetric elastical tendency of an object to deform in all directions when uniformly loaded. We can loosly express it as an extension of Young's modulus in 3D. Young's modulus (E), is the tendency of an object to deform along an axis when opposing forces are applied along that

axis. Shear modulus (G), describes tendency of an object to shear (the deformation of shape at a constant volume) when acted upon by opposing forces.

From predicted bulk and shear moduli values, we can further extract information about materials' Poisson's ratio which is the ratio of transverse contraction strain to longitudinal extension strain in the direction of stretching force as well as calculated B/G ratio. Pugh proposed that if the B/G value is less than the critical value (1.75), the material is considered brittle [141], otherwise it is ductile. From calculated B/G values in Table 5.3, NbP_2 is brittle. Ductile materials have relatively small Young's modulus and can withstand large strains and large energy absorption before fracture as shown in Figure 5.2 i.e steel and aluminium. On the other hand, brittle materials have relatively large Young's modulus and fracture at much lower strains i.e glass and cast iron. Ductile fracture is preferred in most applications. However, brittle materials can be used to craft components for optical communication, computers and other technological devices.

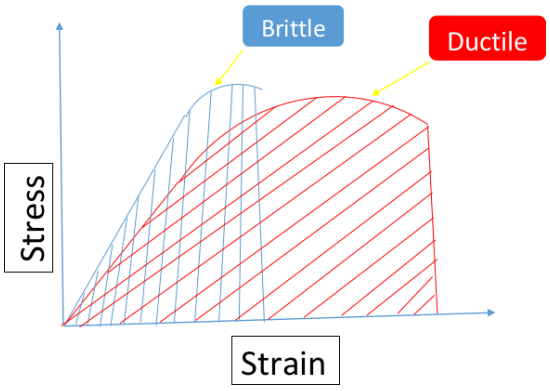


Figure 5.2: Ductile vs Brittle

5.1.3 Dynamical and electronic properties of NbP_2

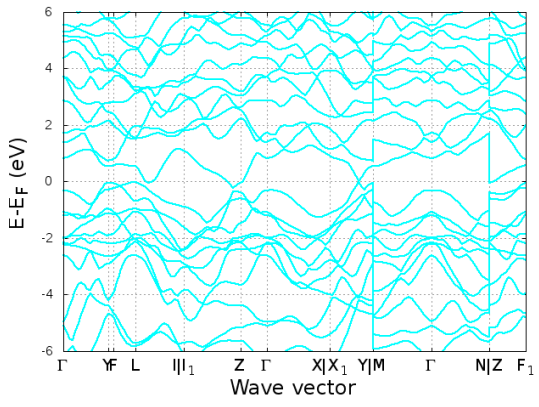


Figure 5.3: NbP_2 electronic Bands

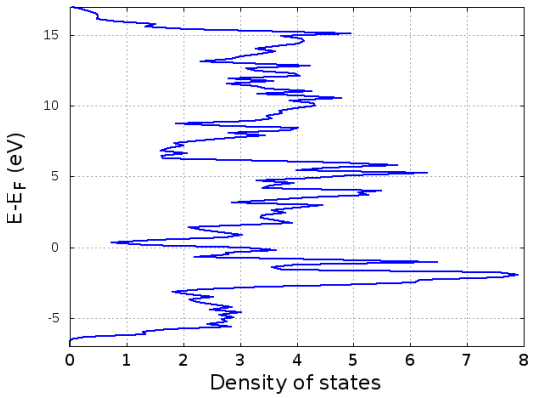


Figure 5.4: Electronic DOS

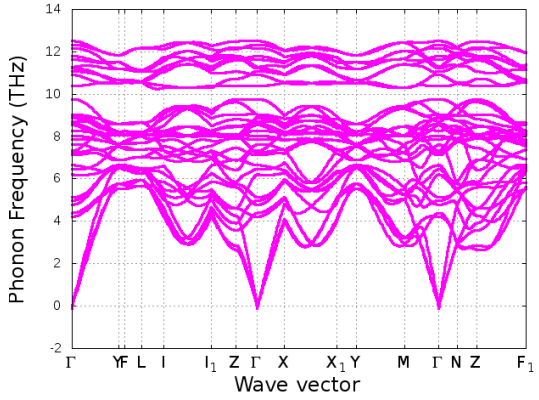


Figure 5.5: NbP_2 phonon Bands

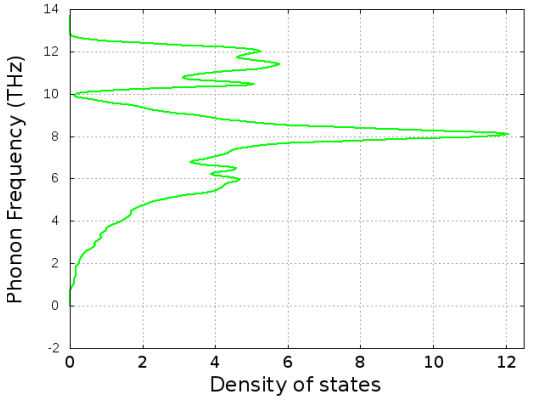


Figure 5.6: Phonon DOS

From Figure 5.5 and Figure 5.6 above, it is visible that NbP_2 is dynamically stable due to presence of only positive vibrational frequencies and is metallic in nature as per the calculated electronic band structure done along high symmetry points of the Brillouin zone and electronic density of states. Occurrence of bands at fermi level (indicated by zero mark) in Figure 5.3 and Figure 5.4 implies that valence bands and conduction bands overlap such that no appreciable amount of energy is required to excite an electron to jump from valence to conduction band.

5.1.4 Optical properties of NbP_2

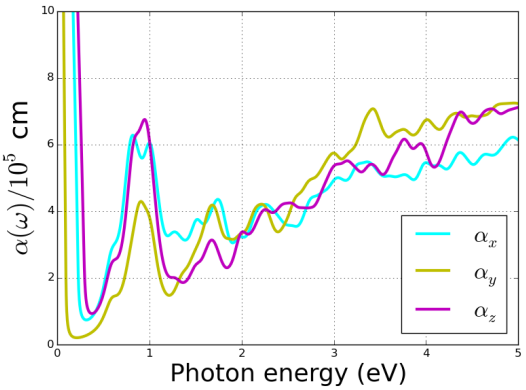


Figure 5.7: NbP_2 absorption coefficient

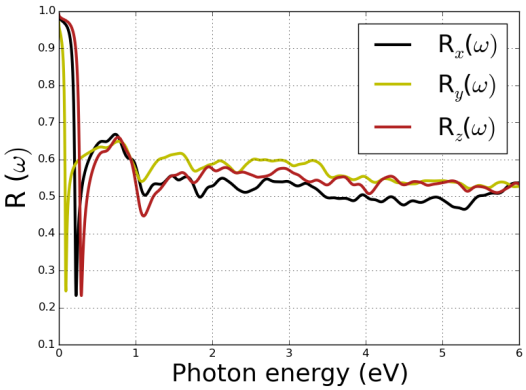


Figure 5.8: NbP_2 reflectivity

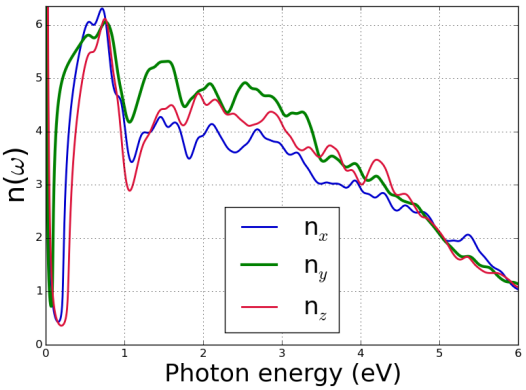


Figure 5.9: NbP_2 refractive index

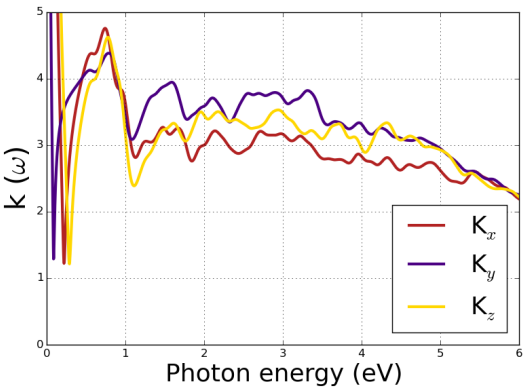


Figure 5.10: NbP_2 extinction coefficient

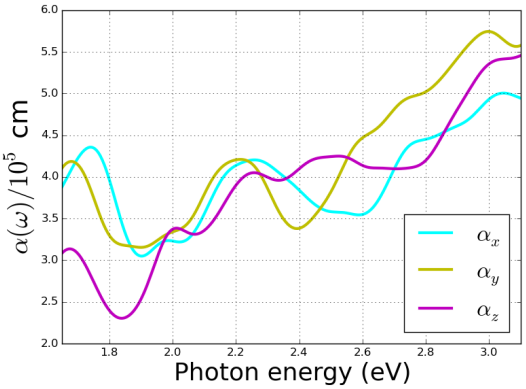


Figure 5.11: Absorption coefficient within the visible range

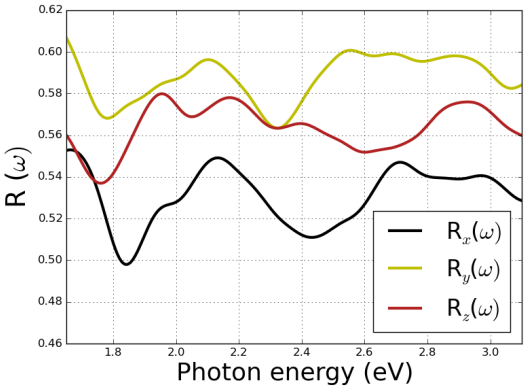


Figure 5.12: Reflectivity within the visible range

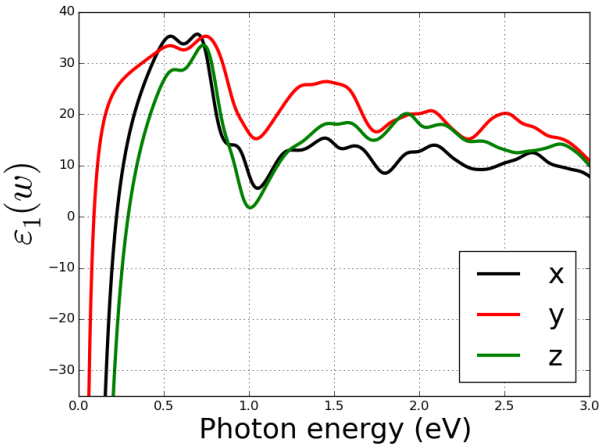


Figure 5.13: Real part of dielectric function

Within an energy range of 0 eV and 5 eV, pronounced absorption peaks occur in infrared region for all the directions and minimum reflectivity occur in infrared region. There is no distinct pattern of refractive index and extinction coefficient. Within the visible regime, maximum photon absorption occur at the edge of visible region for all directions. Since maximum absorption within visible range occur at the edge of visible region, we predict that NbP_2 is violet in colour. Reflectivity within the visible region shows a distinct pattern in that reflectivity in x is minimum, followed by y and maximum in z. From Figure 5.13, Plasma frequency occur in infrared region for all the three directions, hence NbP_2 is not a promising plasmonic material. A low plasma frequency reduces the applicability of NbP_2 to modern plasmonic applications, where high plasmonic quality in the UV-visible frequency regime is desired [142]. Recall that screened plasma frequency is located at the point whereby the total contribution of intraband and interband term of real part vanishes to zero .

5.2 Vanadium diphosphide

There exist only one polymorph of VP_2 that is monoclinic.

5.2.1 Structural and energetic properties of VP_2

Table 5.4: Structural and energetic properties of VP_2

	a(Å)	b(Å)	c(Å)	$\alpha(^\circ)$	$\beta(^\circ)$	$\gamma(^\circ)$	$V_0(Å)^3$	E_{coh}(eV/atom)	E_{form}(eV/atom)	Z
Calc	8.4560	3.1070	7.1730	90	117.23	90	164.60	-4.841	-0.617	4
Exp [37]	8.4641	3.1054	7.1698	90	119.17	90	164.55	-	-	4

Entire study of VP_2 was purely done using PBE only, this is because VP_2 is non-layered, calculated cell parameters were comparable to experimental ones, its space group is C 2/m and lattice type is base centered monoclinic cell. From the data in Table 5.4, VP_2 can be synthesized since it is energetically stable as indicated by negative cohesive and formation energy.

5.2.2 Mechanical properties of VP_2

Table 5.5: Calculated values of independent elastic coefficients

C_{11}	C_{12}	C_{13}	C_{22}	C_{23}	C_{33}	C_{44}	C_{55}	C_{66}
268.21	57.17	86.55	381.27	77.39	301.04	122.12	155.83	114.92

Note that C_{15}, C_{25}, C_{35} and C_{46} had zero values as expected from symmetry. Calculated elastic coefficients shown in Table 5.5 satisfied Born stability condition for monoclinic structures and all eigen values were positive which validates its mechanical stability.

Table 5.6: Calculated B, E, G, ν and B/G

	B	E	G	ν	B/G
Voight (V)	154.75	299.54	127.2	0.1774	1.22
Reuss (R)	152.32	287.29	121.15	0.1857	1.26
Hill (H)	153.53	293.43	124.18	0.1815	1.24

B/G values obtained using three averaging schemes are all less than 1.75 as shown in Table 5.6, hence we predict that VP_2 is a brittle material.

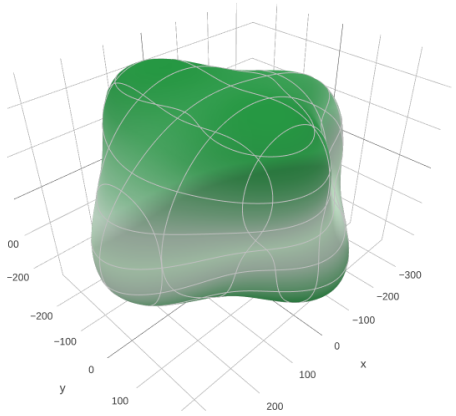


Figure 5.14: 3D directional Young's modulus

Figure 5.14 indicate VP_2 is 'softer' with respect to compression in certain directions which reinforces the fact that compounds under this study exhibit significant mechanical anisotropy.

5.2.3 Dynamical and electronic properties of VP_2

As mentioned before, VP_2 and NbP_2 are isostructural materials, phonon dispersion and electronic band structure of VP_2 are similar to those of NbP_2. From electronic and phonon bands and density of states beneath, it is indisputable that VP_2 is metallic and dynamically stable.

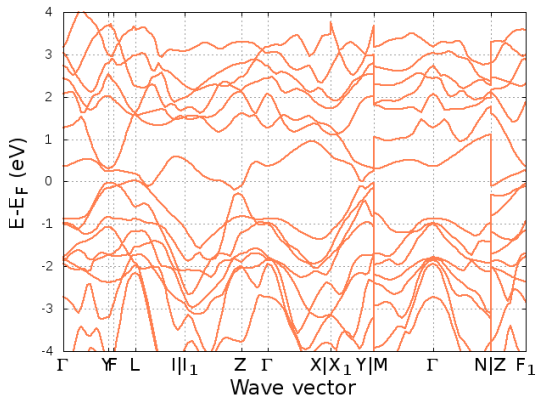


Figure 5.15: VP_2 electronic Bands

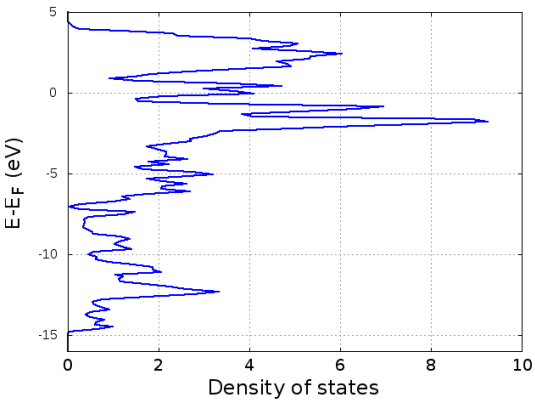


Figure 5.16: Electronic DOS

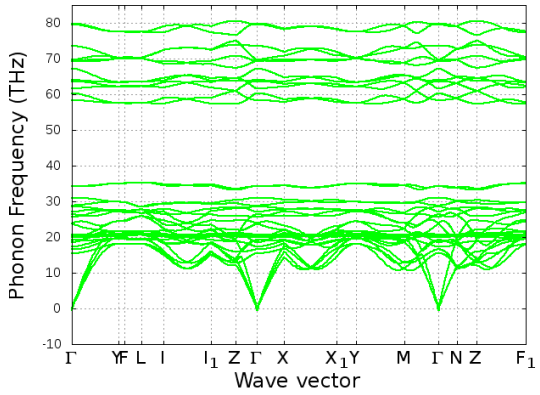


Figure 5.17: VP_2 phonon Bands

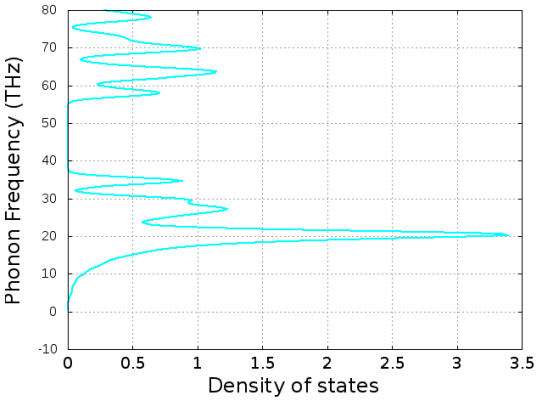


Figure 5.18: Phonon DOS

5.2.4 Optical properties of VP_2

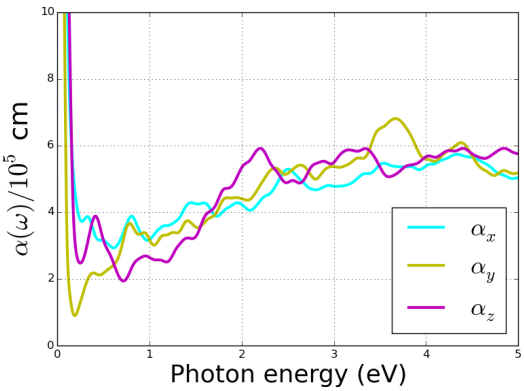


Figure 5.19: VP_2 absorption coefficient

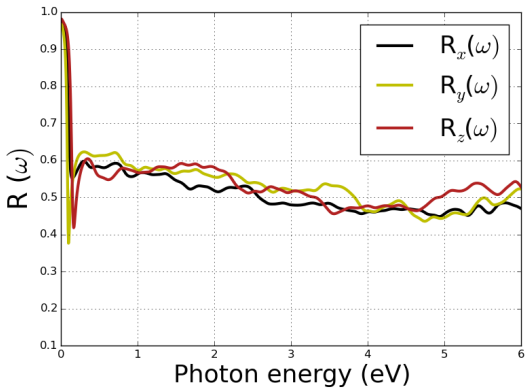


Figure 5.20: VP_2 reflectivity

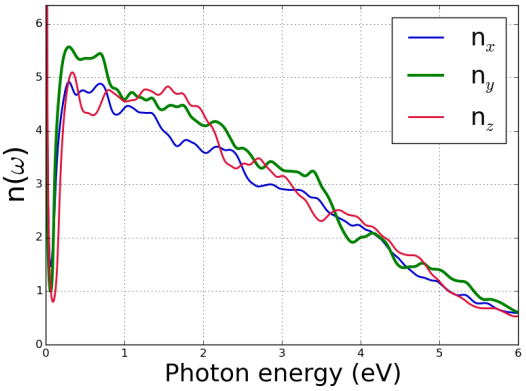


Figure 5.21: VP_2 refractive index

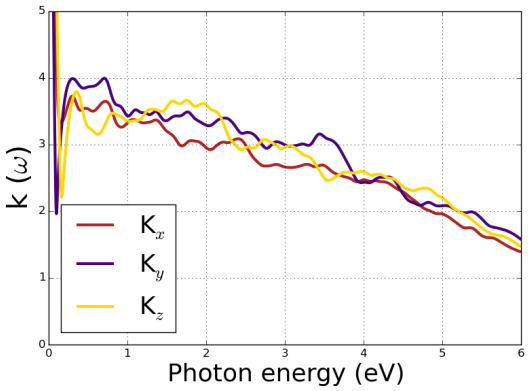


Figure 5.22: VP_2 extinction coefficient

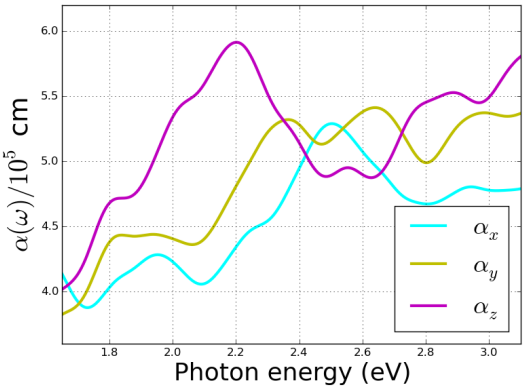


Figure 5.23: Absorption coefficient within the visible range

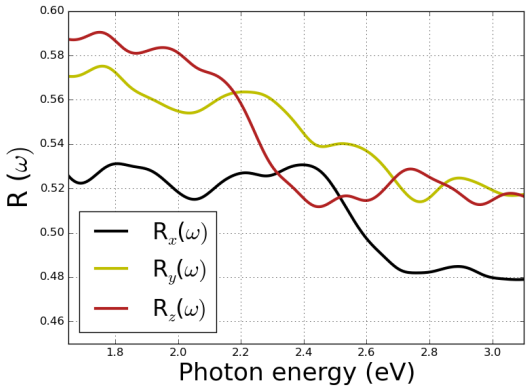


Figure 5.24: Reflectivity within the visible range

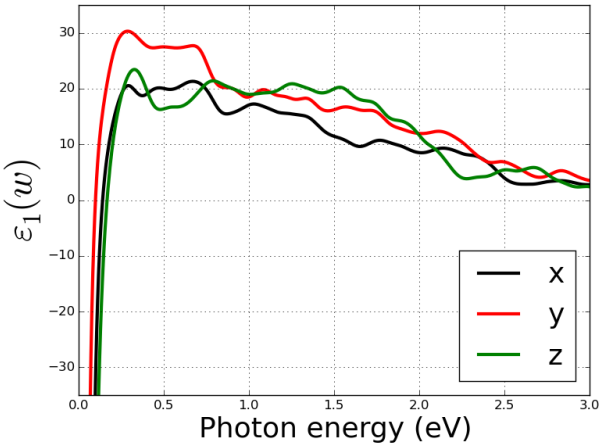


Figure 5.25: Real part of dielectric function

Like NbP_2, VP_2 also shows optical anisotropy in that behaviour of dielectric function is different in all directions. Within energy range of 0 eV and 5 eV, prominent absorption peaks occur within the visible regime for x and z whereas for y it occur outside the visible region. There is no distinct pattern of

reflectivity, refractive index and extinction coefficient. Within the visible regime, maximum absorption occur at around 2.5 eV, 2.64 eV and 2.2 eV for x, y and z directions respectively. Probably, when light shines onto VP_2 along x and y directions, it will appear blue whereas when incoming photon hits along the z-axis, it will appear green. For all directions, screened plasma frequency is located in the infrared region as shown in Figure 5.25 hence VP_2 is not a promising candidate for plasmonic related fields. The plasmon is a well established collective excitation of metals in the visible and near UV but at much lower frequencies, dissipation destroys all trace of the plasmon and typical drude behaviour sets in [143].

5.3 Vanadium diselenide (VSe_2)

VSe_2 had only one polymorph which is trigonal and of space group $P\bar{3}m1$.

5.3.1 EOS done with various functionals

The fact that VSe_2 is layered implies that PBE could not give accurate structural results, hence equation of state calculations was done using three functions i.e PBE, PBE+D2 and PBE+TS. Inclusion of ivdW term helps account for interlayer attraction that is dominated by van der Waals forces.

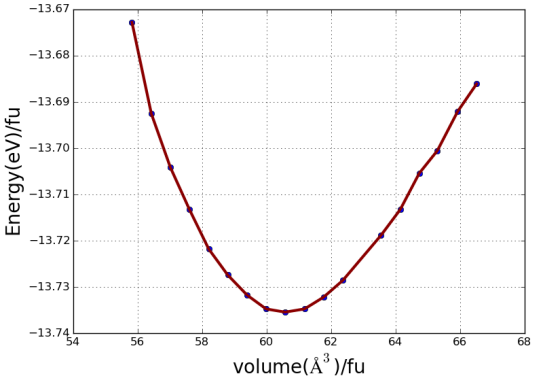


Figure 5.26: PBE+D2

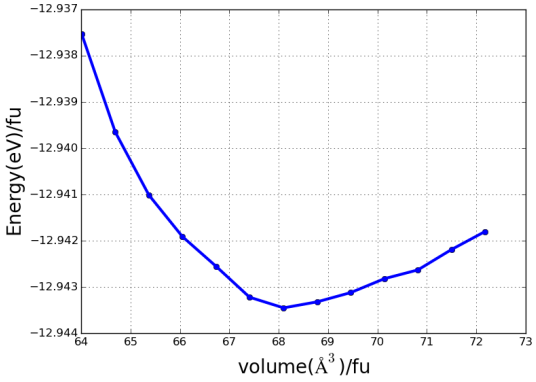


Figure 5.27: PBE

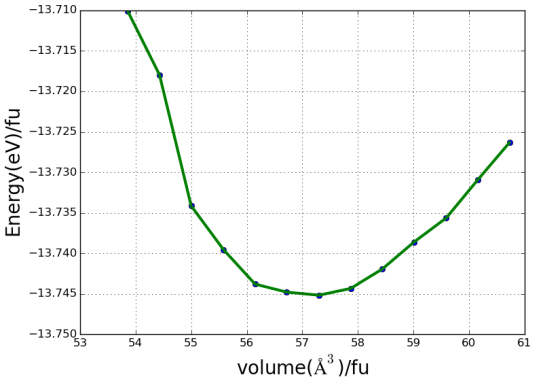


Figure 5.28: PBE+TS

Equilibrium volume obtained when PBE and PBE+TS were used shift towards the right and left of PBE+D2 respectively. Similar trend was observed in their lattice constants.

5.3.2 Structural and energetic properties of VSe_2

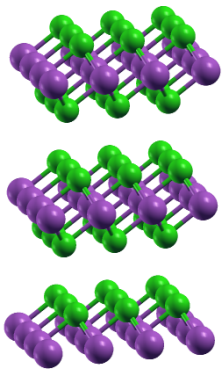


Figure 5.29: VSe_2

Figure 5.29 shows crystal structure of vanadium diselenide, where larger atoms are vanadium and the smaller ones selenium. Similar atomic arrangement existed for other layered TMDs considered in this work namely $NbSe_2$, VS_2, NbS_2, VSe_2, VTe_2 and $NbTe_2$.

From structural data in Table 5.7, though PBE predicted well the in-plane cell parameters, it overestimated the out-of-plane value. PBE+TS underestimated both in-plane and out-of-plane lattice constants which automatically translates to its volume being underestimated as compared to given experimental values. PBE+D2 on the other hand underestimated in-plane lattice parameters but overestimated out-of-plane lattice parameter hence compensating each other resulting in ground state volume that is closer to experimental. Therefore, PBE+D2 described better the structural parameters of VSe_2 and from calculated cohesive and formation energies, trigonal VSe_2 is energetically stable.

Table 5.7: Structural and energetic properties of VSe_2

Functional	a = b (Å)	c(Å)	V_0(Å)^3	$\alpha(^\circ)$	$\beta(^\circ)$	$\gamma(^\circ)$	E_{coh}(eV/atom)	E_{form}(eV/atom)	Z
PBE	3.3520	6.9970	68.10	90	90	120	-4.314	-0.694	1
PBE+TS	3.3350	5.9490	57.30	90	90	120	-4.582	-0.962	1
PBE+D2	3.2240	6.7300	60.58	90	90	120	-4.578	-0.958	1
Exp [34]	3.3480	6.1220	59.43	90	90	120	-	-	1
Exp [38]	3.3587	6.1075	59.67	90	90	120	-	-	1
Exp [144]	3.3400	6.1200	59.13	90	90	120	-	-	1

5.3.3 Mechanical properties of VSe_2

Table 5.8: Calculated values of independent elastic coefficients for VSe_2

	C_{11}	C_{12}	C_{13}	C_{14}	C_{33}	C_{44}
PBE	104.54	18.96	1.90	-0.21	4.03	1.46
PBE+D2	133.62	22.30	21.79	-6.76	58.39	18.60
PBE+TS	99.46	15.18	2.24	-0.69	9.96	2.88

Calculated elastic coefficients shown in Table 5.8 and eigenvalues obtained indicates that VSe_2 is mechanically stable since it fulfilled all Born stability criterion for trigonal structures. It is also worth noting that PBE+D2 predicted values of elastic coefficients of greater magnitude compared to other functionals especially C_{14}, C_{33} and C_{44}.

Table 5.9: Calculated B, E, G, ν and B/G

PBE	B	E	G	ν	B/G
Voight (V)	28.739	52.259	21.830	0.1970	1.32
Reuss (R)	3.959	6.841	2.822	0.2120	1.40
Hill (H)	16.349	29.552	12.326	0.1990	1.33
PBE+D2					
Voight (V)	50.819	87.152	35.890	0.2142	1.42
Reuss (R)	43.950	66.557	26.674	0.2476	1.65
Hill (H)	47.384	76.919	31.282	0.2295	1.51
PBE+TS					
Voight (V)	27.578	52.498	22.194	0.1830	1.24
Reuss (R)	9.008	13.933	5.608	0.2420	1.61
Hill (H)	18.293	33.274	13.901	0.1970	1.32

B/G values obtained using three functionals and all averaging schemes were less than 1.75 as shown in

Table 5.9 implying VSe_2 is brittle.

5.3.4 Dynamical and electronic properties of VSe_2

Since PBE+D2 mimicked well VSe_2 structural properties, further study of bands, phonons and optical properties was done using it. VSe_2 exhibits metallic character and is dynamically stable in its trigonal phase as backed by figures of electronic and phonon dispersion respectively.

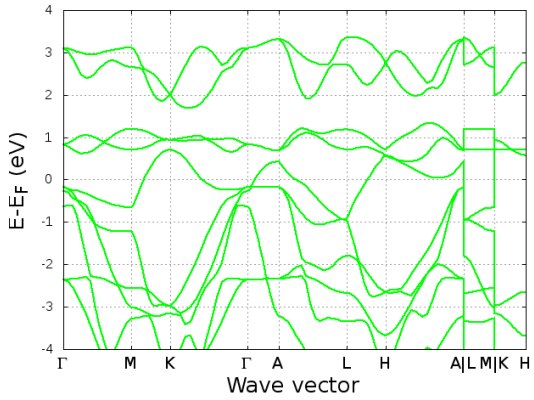


Figure 5.30: VSe_2 electronic Bands

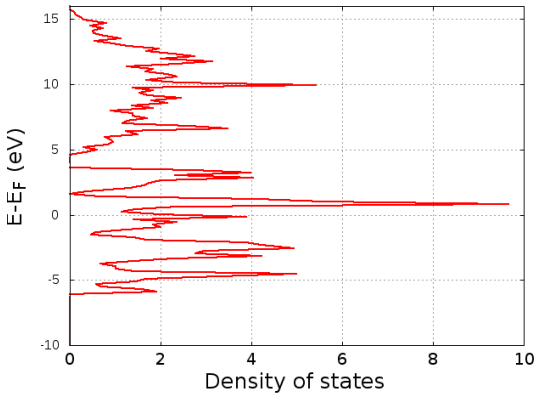


Figure 5.31: Electronic DOS

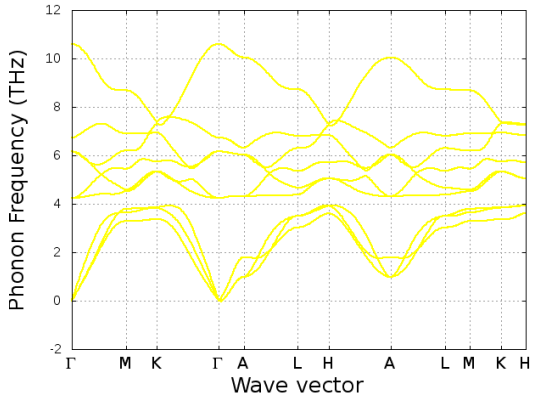


Figure 5.32: VSe_2 phonon Bands

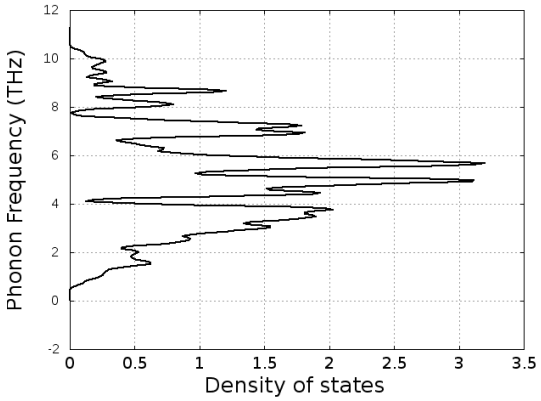


Figure 5.33: Phonon DOS

5.3.5 Optical properties of VSe_2

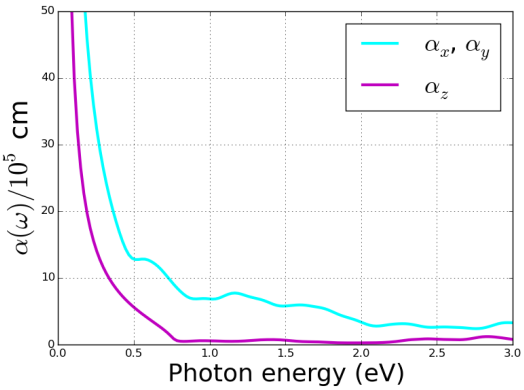


Figure 5.34: VSe_2 absorption coefficient

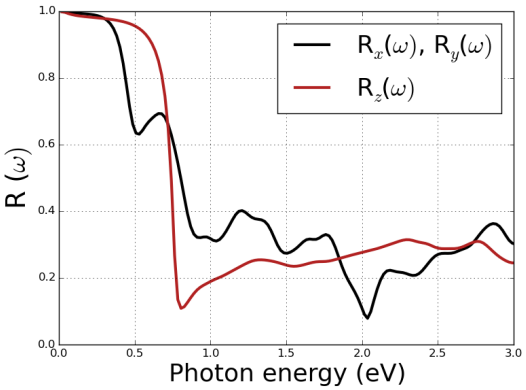


Figure 5.35: VSe_2 reflectivity

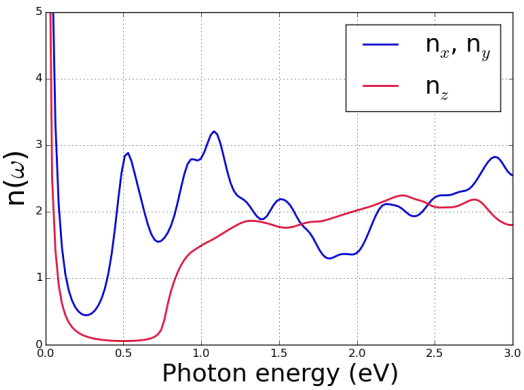


Figure 5.36: VSe_2 refractive index

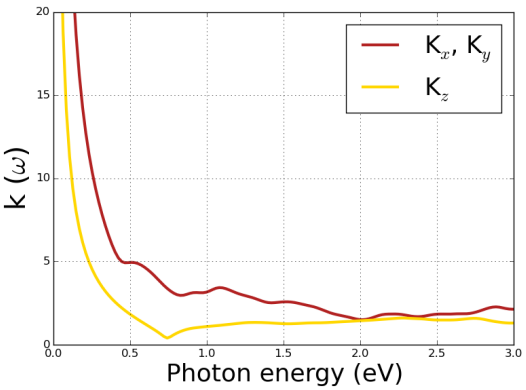


Figure 5.37: VSe_2 extinction coefficient

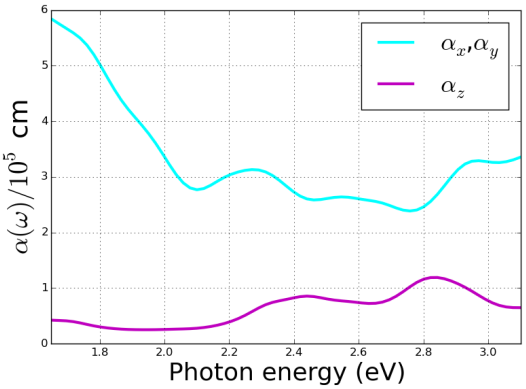


Figure 5.38: Absorption coefficient within the visible range

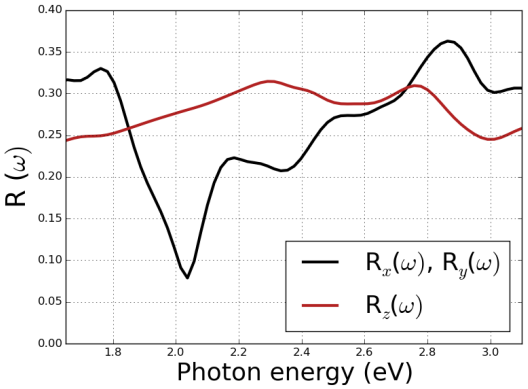


Figure 5.39: Reflectivity within the visible range

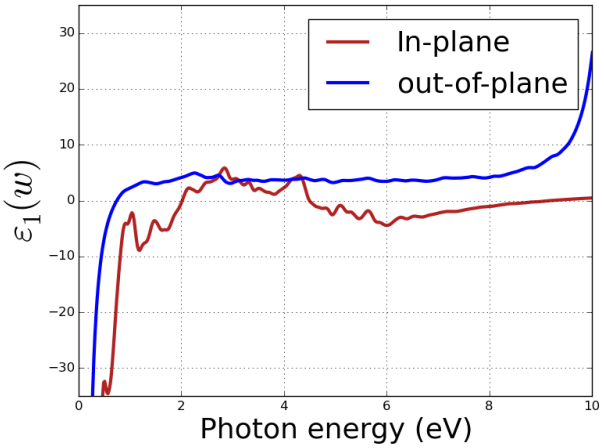


Figure 5.40: Real part of dielectric function

Behaviour of dielectric function is similar in x and y directions (in-plane). Within photon energy range of 0 eV and 3 eV, maximum absorption occur in-plane than out-of-plane as shown in Figure 5.34. There is no distinguished pattern for reflectivity and refractive index. Generally, in-plane extinction is higher than out-of-plane. Within visible range, maximum absorption peaks occur at around 2.97 eV and 2.83 eV for in-plane and out-of-plane respectively as shown in Figure 5.38, based on the obtained energy values, VSe_2 is violet in colour. Out-of-plane plasma frequency occur in infrared region at around 0.7 eV whereas in-plane occur at around 2 eV, 4.25 eV and 9 eV as shown in Figure 5.40. From the obtained values of screened plasma frequency, VSe_2 is a promising plasmonic material when light falls on it along the x and y axes (in-plane) because its in-plane screened plasma frequencies lies within the visible and ultraviolet region. The electromagnetic response of metals in the visible region and near ultraviolet is dominated by the negative epsilon concept [143].

5.4 Vanadium disulphide (VS_2)

5.4.1 Relative stability test of VS_2

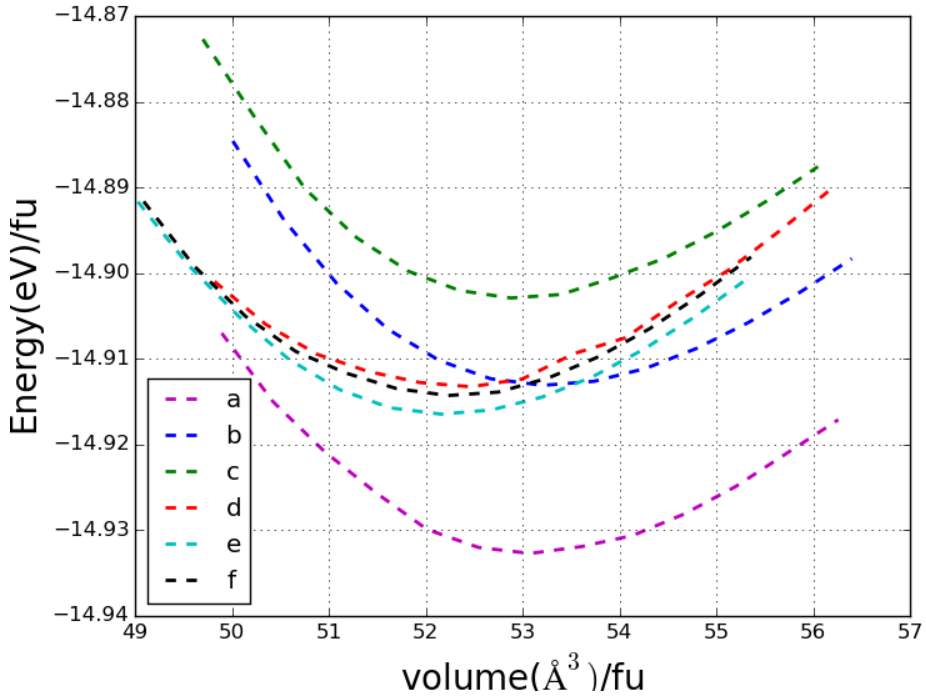


Figure 5.41: Relative stability

Table 5.10: crystal system information

Legend	m.p ID	space group	crystal system
a	1013525	$P6_3/mmc$	Hexagonal
b	849060	$P\bar{1}$	Triclinic
c	1013526	$R\bar{3}m$	Trigonal
d	9561	$P\bar{3}m1$	Trigonal
e	655446	P1	Triclinic
f	611224	P1	Triclinic

Out of nine possible polymorphs of VS_2, six were found competing based on Figure 5.41 above done using PBE+D2 functional. Hexagonal crystal system whose space group is $P6_3/mmc$ and m.p ID 1013525 as shown in Table 5.10 was found to be the energetically favoured ground state structure which is also backed up by Figure 5.42 which is a screen shot showing phase diagram of compounds composed of vanadium and sulphur taken from materials project database. Further studies was conducted for this specific polymorph.

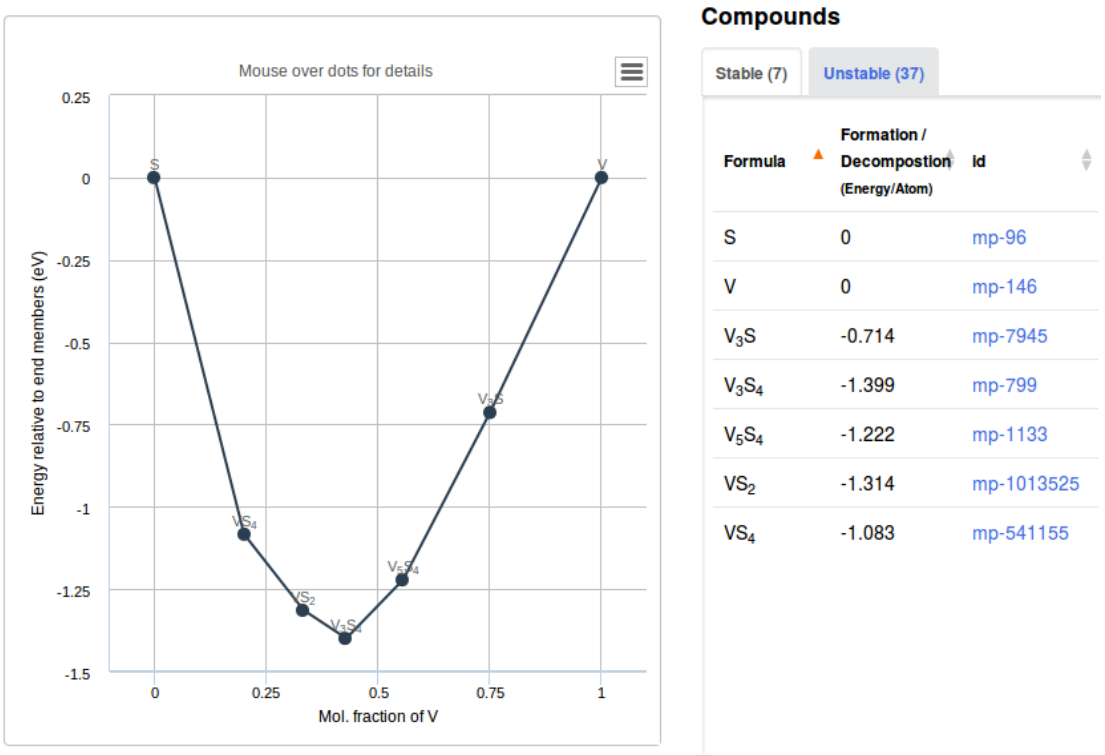


Figure 5.42: Phase diagram

5.4.2 EOS done with various functionals

As the case of VSe_2, structural properties of stable VS_2 was carried out using three functions giving the following EOS.

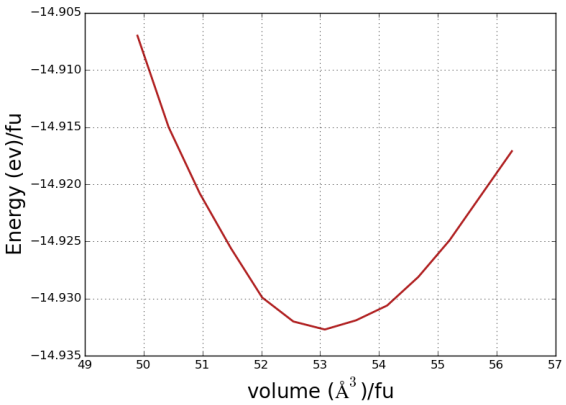


Figure 5.43: PBE+D2

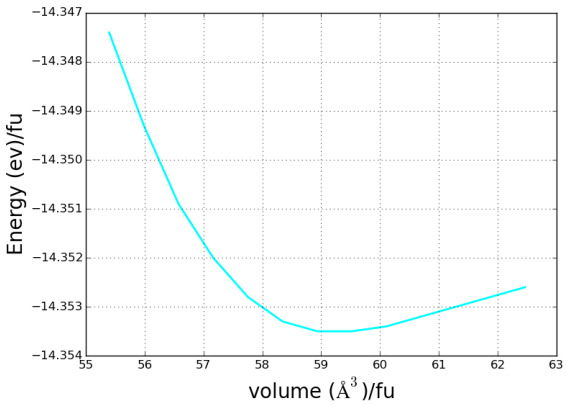


Figure 5.44: PBE

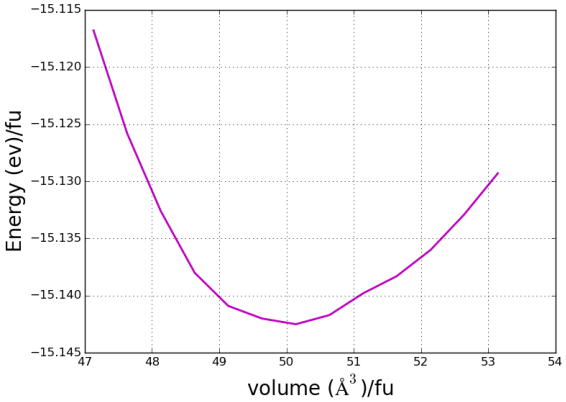


Figure 5.45: PBE+TS

5.4.3 Structural and thermal properties of VS_2

Table 5.11: Stable hexagonal VS_2

Functional	a = b (Å)	c (Å)	$\alpha(^\circ)$	$\beta(^\circ)$	$\gamma(^\circ)$	$V_0(Å)^3$	E_{coh}(eV/atom)	E_{form}(eV/atom)	Z
PBE	3.181	13.551	90	90	120	118.740	-4.784	-0.870	2
PBE+TS	3.143	11.696	90	90	120	100.080	-5.047	-1.133	2
PBE+D2	3.177	12.770	90	90	120	106.379	-4.977	-1.063	2
m.p (PBE)	3.180	14.43	90	90	120	126.389	-	- 1.314	2

The obtained values of equilibrium volume are of the following order from high to low; PBE, PBE+TS, PBE+D2. Structural results using PBE are comparable to those given in materials project. Since VS_2 is a layered material, further studies was done using PBE+D2 to account for ivdW correction.

5.4.4 Mechanical properties of hexagonal VS_2

Table 5.12: Calculated values of independent elastic coefficients

	C_{11}	C_{12}	C_{13}	C_{33}	C_{44}	C_{66}
PBE	191.03	69.76	3.41	15.15	5.73	60.64
PBE+D2	187.77	70.12	2.60	4.50	4.18	58.82
PBE+TS	182.01	66.14	2.34	5.67	5.10	57.94

From predicted mechanical characteristics given in Table 5.12, VS_2 fulfilled Born conditions for hexagonal structures hence mechanically stable.

Table 5.13: Calculated B, E, G, ν and B/G

PBE	B	E	G	ν	B/G
Voight (V)	61.150	89.850	35.794	0.25511	1.71
Reuss (R)	14.156	25.280	10.513	0.20236	1.35
Hill (H)	37.653	57.644	23.153	0.24485	1.63
PBE+D2					
Voight (V)	58.966	85.030	34.751	0.25967	1.70
Reuss (R)	4.473	12.571	6.093	0.03165	0.73
Hill (H)	31.720	49.419	19.922	0.24033	1.59
PBE+TS					
Voight (V)	56.815	84.106	33.555	0.25327	1.69
Reuss (R)	5.584	15.483	7.459	0.03789	0.75
Hill (H)	31.199	50.464	20.507	0.23042	1.52

All the three functionals and averaging schemes gave B/G ratio less than 1.75, implying VS_2 is a brittle material.

5.4.5 Dynamical properties of VS_2

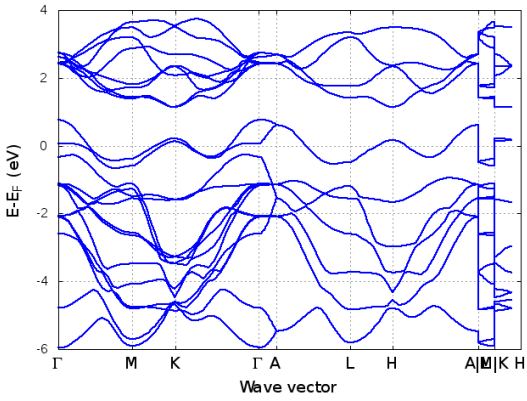


Figure 5.46: VS_2 electronic Bands

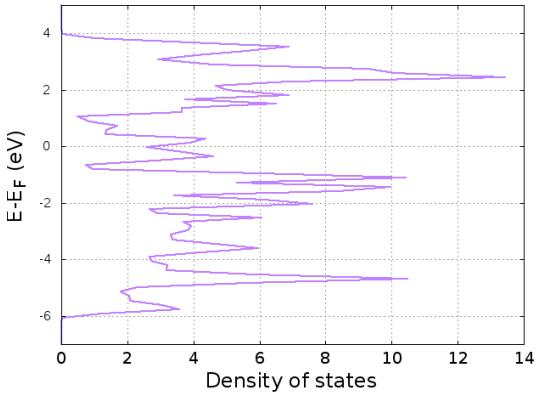


Figure 5.47: Electronic DOS

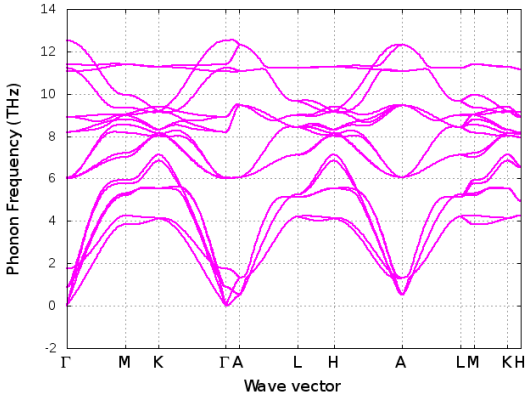


Figure 5.48: VS_2 phonon Bands

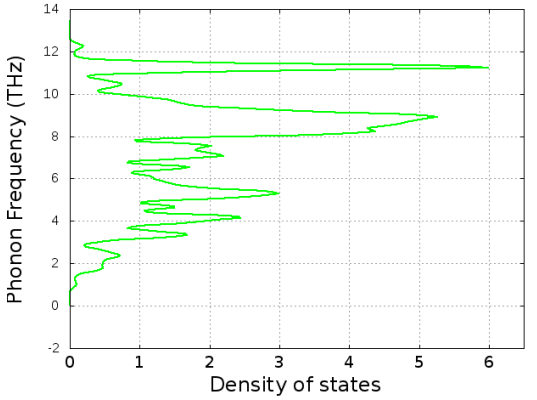


Figure 5.49: Phonon DOS

From Figure 5.48 and Figure 5.46, hexagonal VS_2 is dynamically stable and metallic. This is also supported by their phonon and electronic density of states.

5.4.6 Optical properties of VS_2

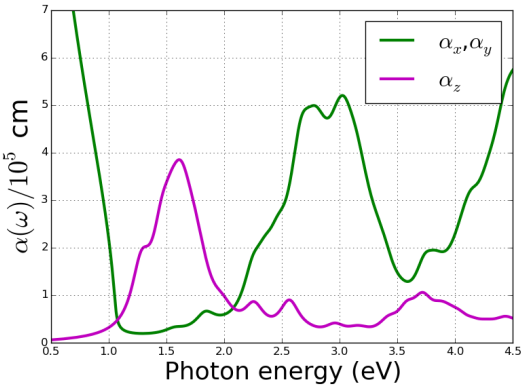


Figure 5.50: VS_2 absorption coefficient

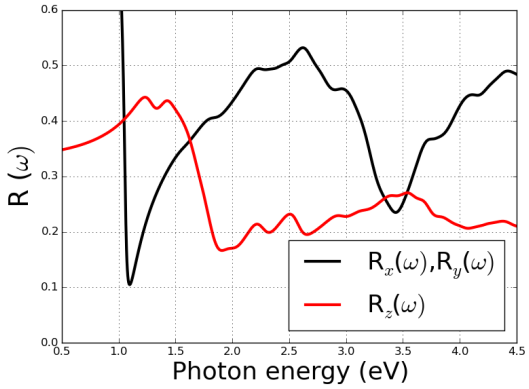


Figure 5.51: VS_2 reflectivity

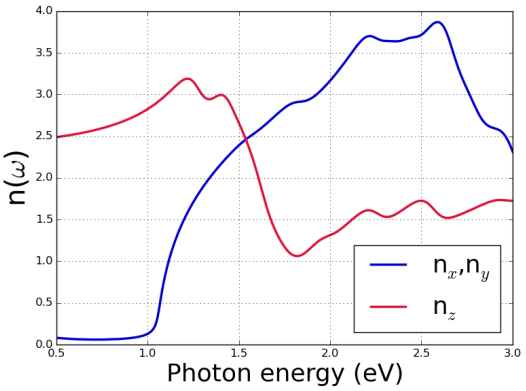


Figure 5.52: VS_2 refractive index

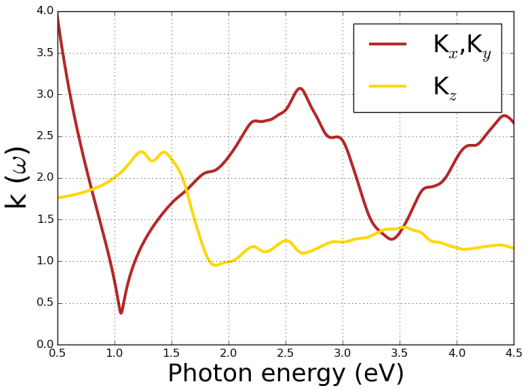


Figure 5.53: VS_2 extinction coefficient

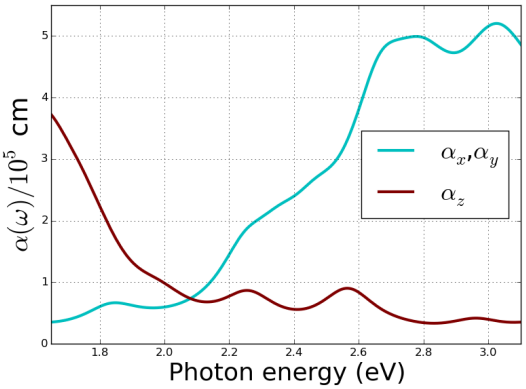


Figure 5.54: Absorption coefficient within the visible range

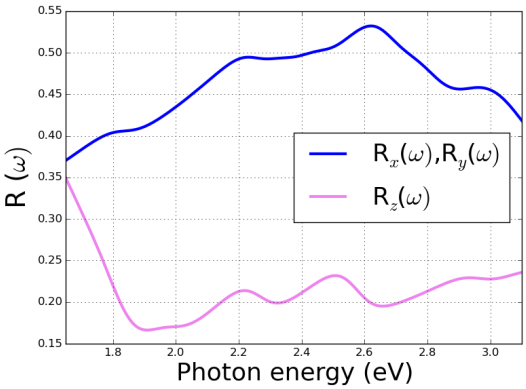


Figure 5.55: Reflectivity within the visible range

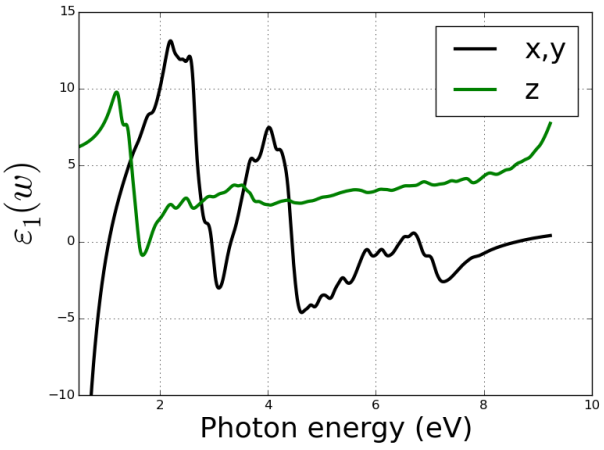


Figure 5.56: Real part of dielectric function

Behaviour of dielectric function is similar in x and y direction (in-plane) but different for z direction (out-of-plane). Out-of-plane absorption occur at onset of visible region whereas pronounced in-plane absorption peaks occur within the visible range. There is no distinct pattern of reflectivity and extinction

coefficient. Out-of-plane refractive index exceeded in-plane refractive index upto around 1.55 eV beyond which in-plane dominates. Within the visible regime, in-plane reflectivity exceeds out-of-plane reflectivity. On the other hand, still within the visible region, prominent wide absorption peak occur at around 2.7 eV and 2.55 eV for in-plane and out-of-plane respectively. This implies that if photon impinges on VS_2 in any direction, it will probably appear blue in colour because maximum in-plane and out-of plane absorption occur between 2.5 and 2.7 eV which corresponds to blue colour in the electromagnetic spectrum. Screened out-of-plane plasma frequencies occur at around 1.6 eV and 1.8 eV. Several in-plane plasma frequencies are noticeable at around 0.8 eV, 3.0 eV, 3.3 eV, 4.3 eV, 6.5 eV, 6.8 eV and 8.4 eV as shown in Figure 5.56 hence VS_2 is a promising material for plasmonic applications since plasmon frequencies lies within the visible and UV regime. At lower frequencies, from the near infrared downwards, dissipation asserts itself and the dielectric function is essentially imaginary [143].

5.5 Vanadium ditelluride (VTe_2)

VTe_2 had two possible structural polymorphs namely trigonal and monoclinic.

5.5.1 Relative stability test of VTe_2

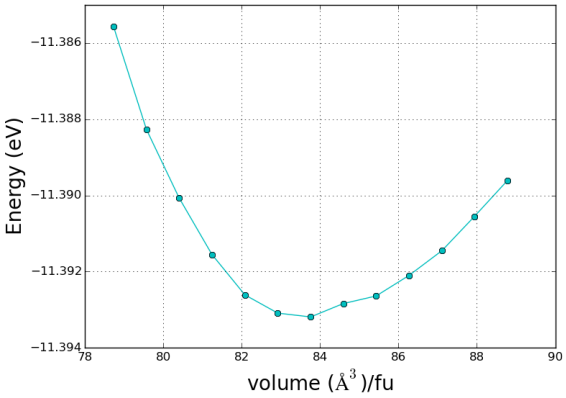


Figure 5.57: Trigonal

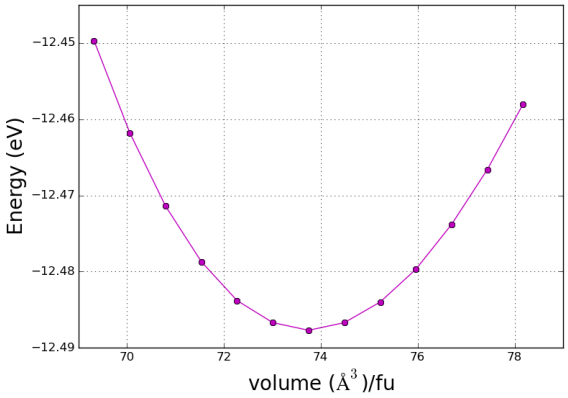


Figure 5.58: Monoclinic

Out of the two competing polymorphs, monoclinic phase of VTe_2 whose space group is C2/m is preferred ground state structure since its equilibrium energy is lower than that for trigonal phase as shown in Figure 5.57 and 5.58.

5.5.2 EOS of monoclinic VTe_2 for various functionals

EOS calculation of stable VTe_2 was carried out using four functionals as given below.

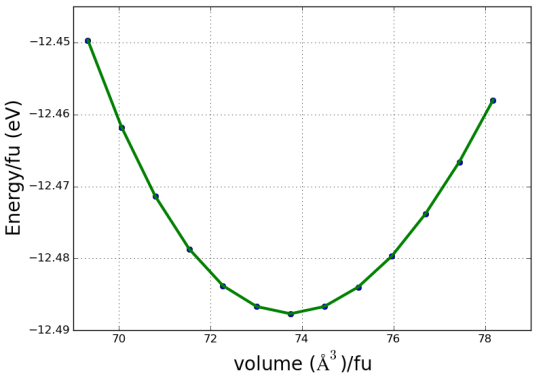


Figure 5.59: PBE+D2

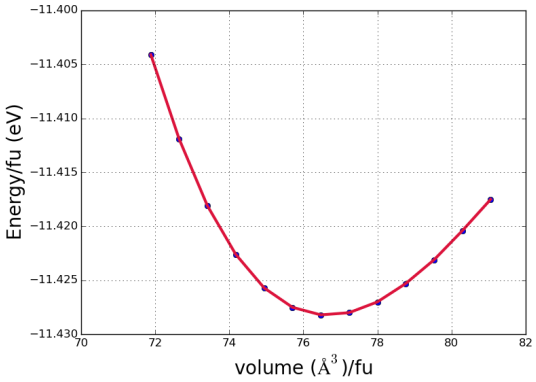


Figure 5.60: PBE

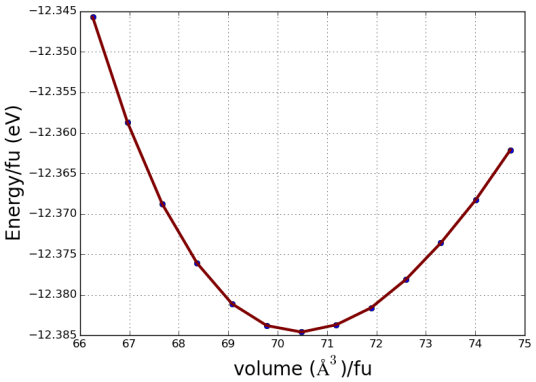


Figure 5.61: PBE+TS

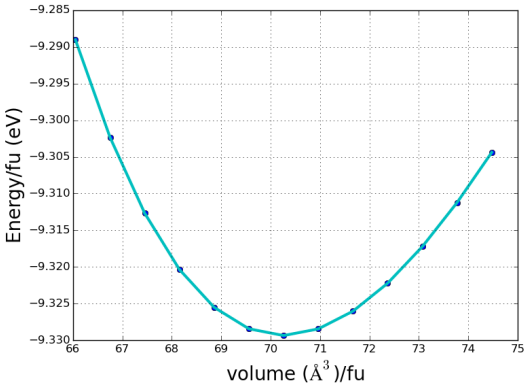


Figure 5.62: PBEsol

Optimization at fixed volume set was done using PBE, PBE+D2, PBE+TS and PBEsol. The order of equilibrium volumes per formula unit predicted using various functionals from high to low were PBE > PBE+D2 > PBE+TS > PBEsol. Note that PBEsol was applied for ditellurides since PBE, PBE+D2 and PBE+TS did not imitate well their structural properties especially for $NbTe_2$.

5.5.3 Structural and energetic properties of monoclinic VTe_2

Table 5.14: Structural and energetic properties VTe_2

	a(Å)	b(Å)	c(Å)	$\alpha(^\circ)$	$\beta(^\circ)$	$\gamma(^\circ)$	$V_0(Å)^3$	E_{coh}(eV/atom)	E_{form}(eV/atom)	Z
PBE+D2	3.543	14.691	9.293	67.529	90	90	446.93	-4.162	-0.674	6
PBE+TS	3.490	14.471	9.153	67.529	90	90	427.13	-4.128	-0.640	6
PBE	3.586	14.869	9.406	67.529	90	90	463.41	-3.809	-0.321	6
PBEsol	3.486	14.455	9.144	67.529	90	90	425.79	-3.110	-0.334	6
Exp [37]	3.595	14.341	9.069	70.430	90	90	440.51	-	-	6

From obtained structural data shown in Table 5.14, PBE+D2 gave computed volume that was closer to experimental though slightly overestimated. PBE overestimated by a larger margin whereas PBE+TS and PBEsol underestimated predicted volume by larger magnitude.

5.5.4 Mechanical properties of VTe_2

Table 5.15: Calculated values of independent elastic coefficients

	C_{11}	C_{12}	C_{13}	C_{22}	C_{23}	C_{33}	C_{44}	C_{55}	C_{66}
PBE	96.78	15.87	13.21	26.95	15.65	74.12	13.74	27.85	17.79
PBE+D2	93.67	21.68	15.27	46.32	14.08	80.95	14.66	30.33	23.85
PBE+TS	92.72	11.33	9.739	15.40	13.02	68.56	12.91	28.64	15.38
PBEsol	98.06	15.45	16.93	17.05	12.96	75.69	13.59	27.31	17.49

Note that C_{15}, C_{25}, C_{35} and C_{46} had zero values. From predicted numerical results of independent elastic coefficients given in Table 5.15, VTe_2 fulfilled Born stability conditions for monoclinic crystal systems and the obtained eigenvalues were all positive hence it is mechanically stable.

Table 5.16: Calculated B, E, G, ν and B/G

PBE	B	E	G	ν	B/G
Voight (V)	31.922	53.833	22.082	0.2190	1.45
Reuss (R)	19.498	29.967	12.046	0.2440	1.62
Hill (H)	25.71	41.918	17.064	0.2280	1.51
PBE+D2					
Voight (V)	35.889	61.057	25.096	0.2165	1.43
Reuss (R)	25.724	39.414	15.833	0.2446	1.62
Hill (H)	30.807	50.264	20.465	0.2281	1.50
PBE+TS					
Voight (V)	27.205	49.900	20.891	0.1940	1.30
Reuss (R)	12.819	21.839	8.979	0.2160	1.43
Hill (H)	20.012	35.880	14.935	0.2010	1.34
PBEsol					
Voight (V)	31.276	52.226	21.374	0.2217	1.46
Reuss (R)	11.215	23.020	9.941	0.1579	1.13
Hill (H)	21.246	37.709	15.657	0.2042	1.36

B/G values obtained using four functionals that were analyzed based on three averaging schemes gave values less than 1.75 as shown in Table 5.16, signifying VTe_2 is a brittle material.

5.5.5 Dynamical and electronic properties of VTe_2

Further study of VTe_2 was conducted using PBE+D2 since it reproduced well its structural properties better than other functionals. VTe_2 is metallic as shown in Figure 5.63 and Figure 5.64 and is dynamically stable as backed by Figure 5.65 and 5.66 respectively.

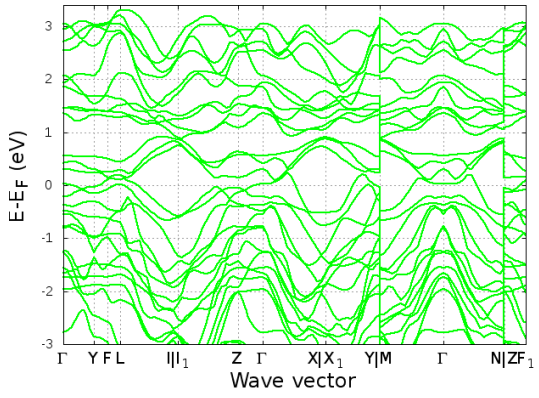


Figure 5.63: VTe_2 electronic Bands

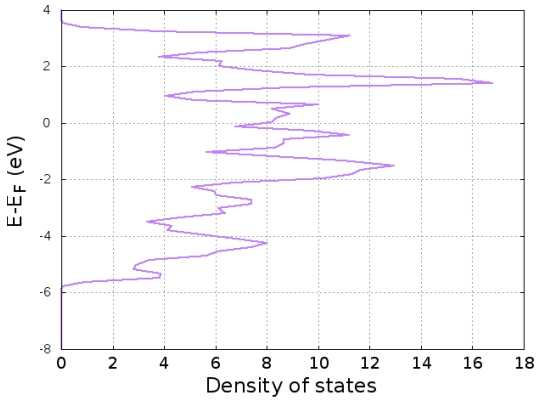


Figure 5.64: Electronic DOS

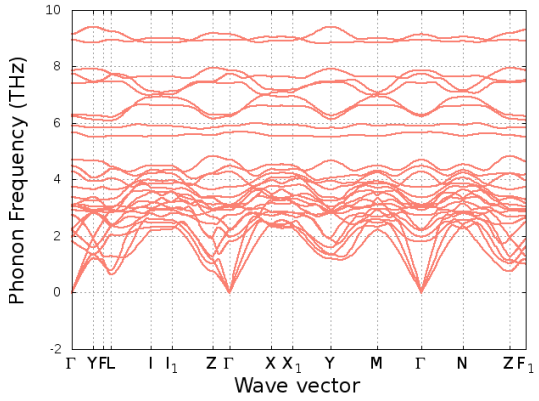


Figure 5.65: VTe_2 phonon Bands

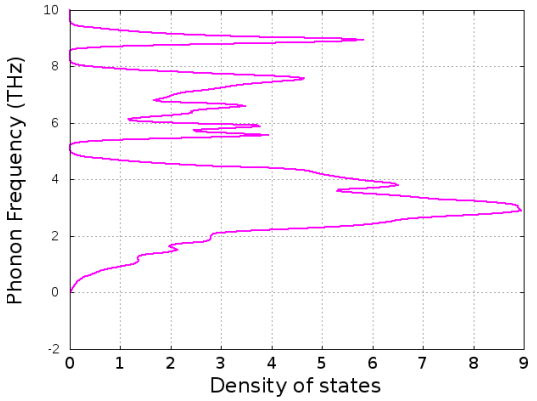


Figure 5.66: Phonon DOS

5.5.6 Optical properties of VTe_2

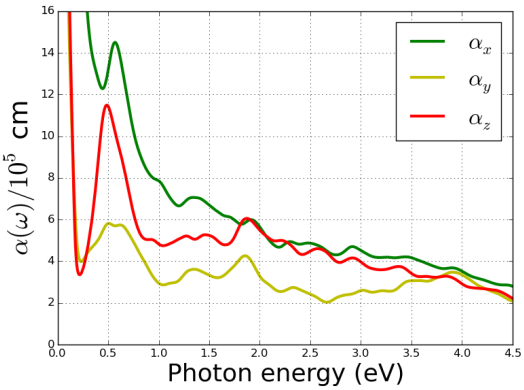


Figure 5.67: VTe_2 absorption coefficient

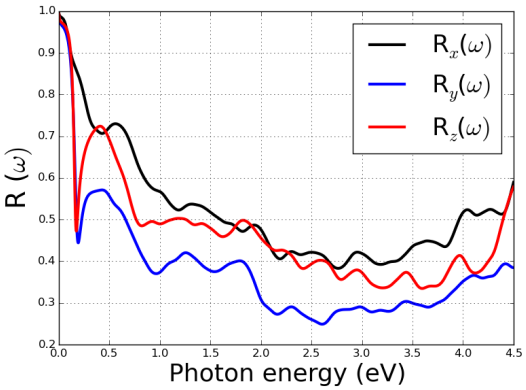


Figure 5.68: VTe_2 reflectivity

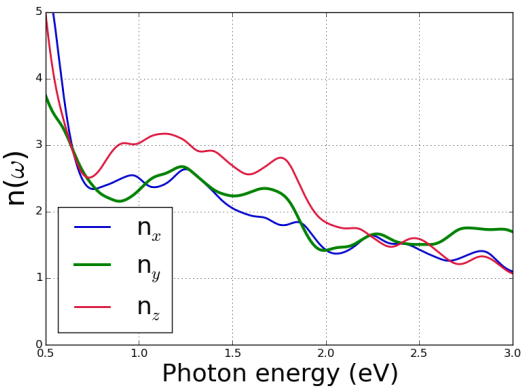


Figure 5.69: VTe_2 refractive index

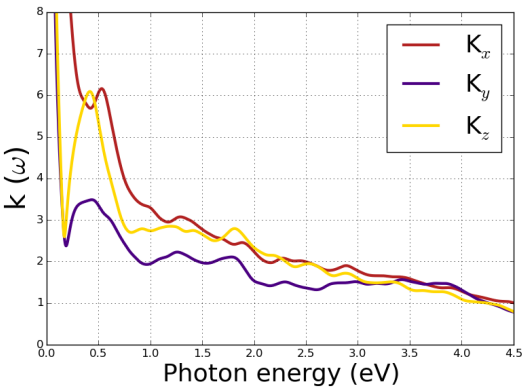


Figure 5.70: VTe_2 extinction coefficient

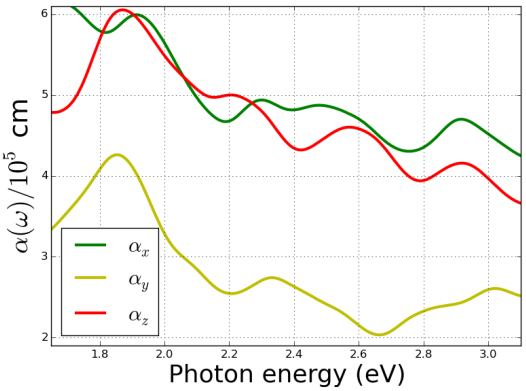


Figure 5.71: Absorption coefficient within the visible range

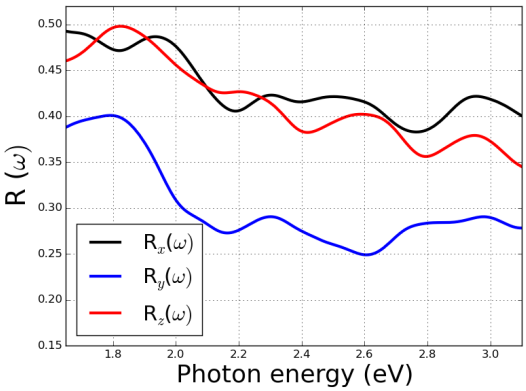


Figure 5.72: Reflectivity within the visible range

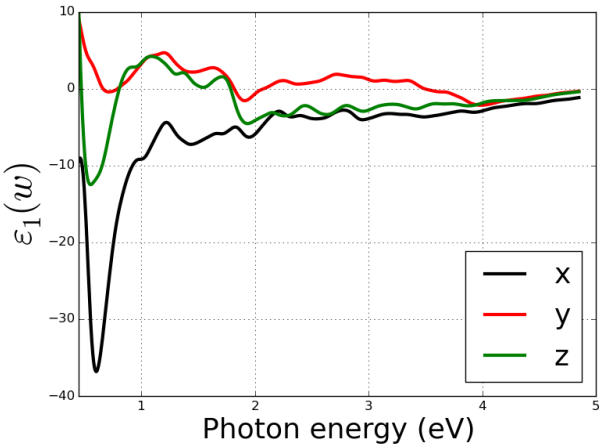


Figure 5.73: Real part of dielectric function

Generally, absorption and reflectivity is higher in x direction followed by z and y directions respectively within photon energy range of 0 eV and 4.5 eV as backed by Figure 5.67 and 5.68. Refractive indices as well extinction coefficients also depict optical anisotropy. From Figure 5.71, maximum absorption occur between 1.8 eV and 2.0 eV which corresponds to red colour in the electromagnetic spectrum hence we predict that VTe_2 is red in colour. Although absorption is minimum for y direction, its corresponding reflectivity is also minimum within visible region. Within energy range of 0 eV and 5 eV, screened plasma frequency occur at around 0.4 eV, 0.7 eV, 1.7 eV and 2.0 eV for y direction, 0.7 eV and 1.6 eV for z direction and no plasma frequency was predicted in x direction for given energy range. VTe_2 is not an efficient plasmonic material because its screened plasma frequencies occur in the visible regime for only y-direction as shown in Figure 5.73, most of plasmon excitations occur in the infrared region whereby very little signal can be transmitted. Below the plasma frequency, very little can be transmitted, above and especially in the visible region, the material is transparent [143].

5.6 Niobium ditelluride ($NbTe_2$)

$NbTe_2$ had just one polymorph belonging to monoclinic crystal system of space group C2/m.

5.6.1 EOS done with various functionals

Being a telluride, structural study was carried out using four functionals as in the case of VTe_2.

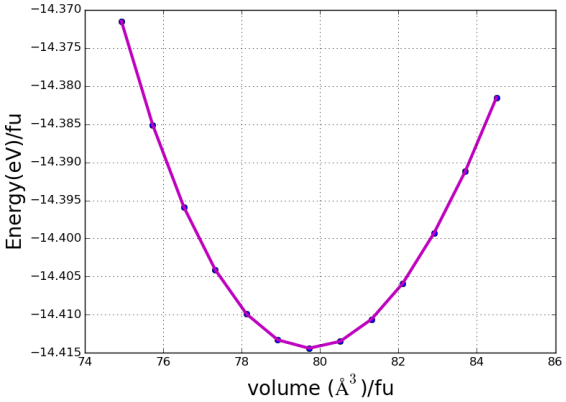


Figure 5.74: PBE+D2

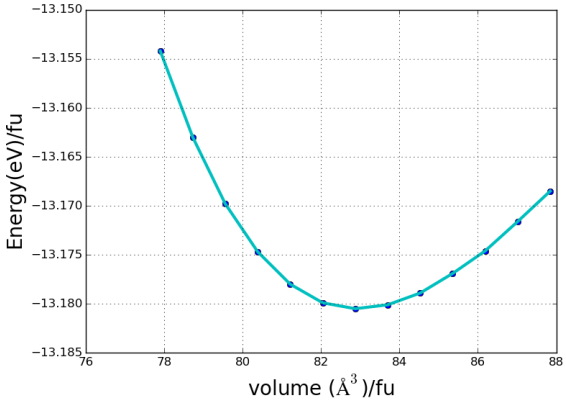


Figure 5.75: PBE

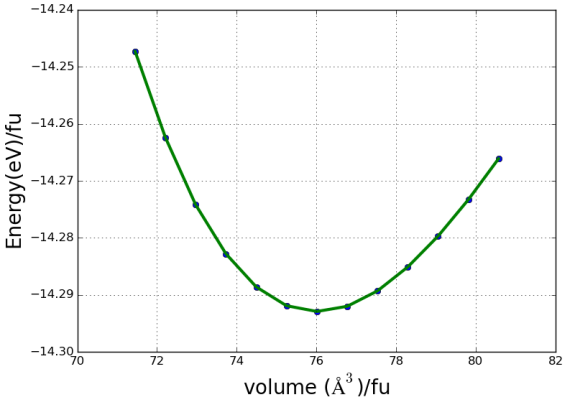


Figure 5.76: PBE+TS

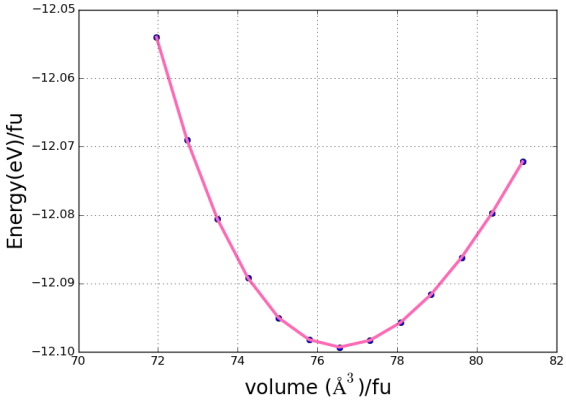


Figure 5.77: PBEsol

The trend of computed equilibrium volume per formula unit and lattice parameters predicted using four functionals was of the following order from functional that gave higher to lower values; PBE $>$ PBE+D2 $>$ PBEsol $>$ PBE+TS.

5.6.2 Structural and energetic properties of $NbTe_2$

Table 5.17: Structural and energetic properties of $NbTe_2$

	a(Å)	b(Å)	c(Å)	$\alpha(^\circ)$	$\beta(^\circ)$	$\gamma(^\circ)$	$V_0(Å)^3$	E_{coh}(eV/atom)	E_{form}(eV/atom)	Z
PBE+D2	3.633	15.028	9.525	68.253	90	90	483.022	-4.806	-0.873	6
PBE+TS	3.576	14.792	9.375	68.253	90	90	460.64	-4.765	-0.833	6
PBE	3.681	15.224	9.649	68.253	90	90	502.21	-4.394	-0.461	6
PBEsol	3.577	14.823	9.439	67.964	90	90	463.93	-4.034	-0.480	6
Exp [46]	3.642	14.736	9.375	69.586	90	90	471.56	-	-	6

From Table 5.17; PBE, PBE+D2 and PBE+TS gave predicted values of volume and consequently lattice constants that had larger magnitude of variation from experimental than when PBEsol was applied although it underestimated α by large margin as compared to experimental value. For $NbTe_2$,

PBEsol was used for further study as compared to other compounds under study where PBE+D2 was applied.

5.6.3 Mechanical properties of $NbTe_2$

Table 5.18: Calculated values of independent elastic coefficients for $NbTe_2$

	C_{11}	C_{12}	C_{13}	C_{22}	C_{23}	C_{33}	C_{44}	C_{55}	C_{66}
PBE	89.874	17.752	20.227	24.558	16.464	85.802	17.894	30.124	21.915
PBE+D2	96.600	25.701	25.489	42.744	21.244	102.240	21.181	33.814	28.193
PBE+TS	80.884	11.830	15.394	11.578	13.795	81.960	17.128	29.974	18.943
PBEsol	84.700	14.720	19.730	20.460	13.010	84.800	15.470	30.810	20.820

Note that C_{15}, C_{25}, C_{35} and C_{46} had zero values as expected from symmetry. From predicted values of independent elastic coefficients shown in Table 5.18, $NbTe_2$ is mechanically stable.

Table 5.19: Calculated B, E, G, ν and B/G

PBE	B	E	G	ν	B/G
Voight (V)	34.347	57.817	23.706	0.2195	1.45
Reuss (R)	19.197	34.268	14.249	0.2025	1.35
Hill (H)	26.772	46.051	18.977	0.2133	1.41
PBE+D2					
Voight (V)	42.939	68.827	27.914	0.2329	1.53
Reuss (R)	32.107	47.302	18.854	0.2545	1.70
Hill (H)	37.523	58.086	23.384	0.2420	1.60
PBE+TS					
Voight (V)	28.495	52.686	22.102	0.1919	1.29
Reuss (R)	9.207	21.552	9.709	0.1099	0.95
Hill (H)	18.851	37.243	15.906	0.1707	1.19
PBEsol					
Voight (V)	31.656	55.390	22.919	0.2084	1.38
Reuss (R)	13.757	28.286	12.221	0.1573	1.12
Hill (H)	22.707	41.902	17.57	0.1924	1.29

From B/G values given in Table 5.19, $NbTe_2$ is a brittle material.

5.6.4 Dynamical and electronic properties of $NbTe_2$

Dynamical, electronic and optical study of $NbTe_2$ was conducted using PBEsol as already stated in section 5.6.2.

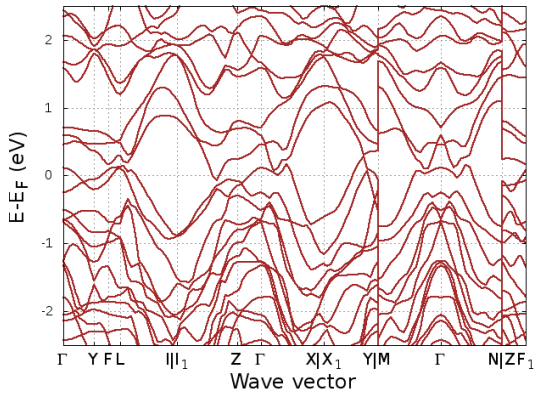


Figure 5.78: $NbTe_2$ electronic Bands

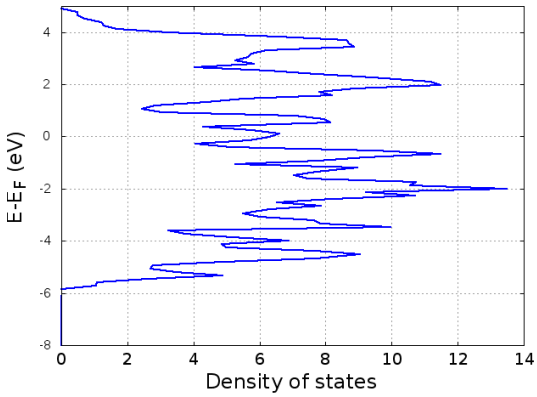


Figure 5.79: Electronic DOS

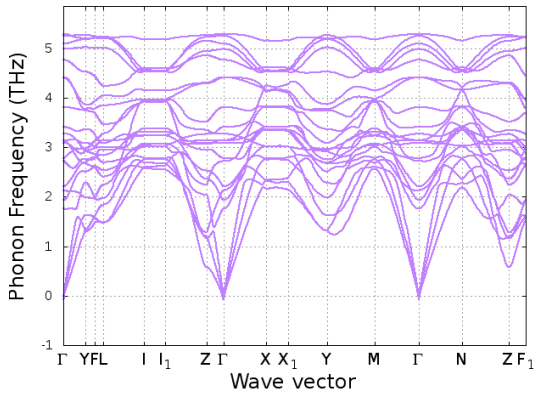


Figure 5.80: $NbTe_2$ phonon Bands

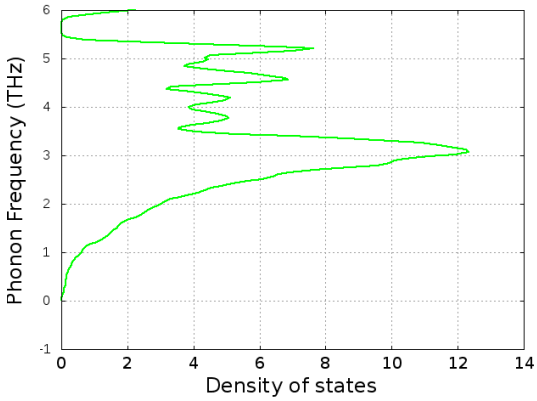


Figure 5.81: Phonon DOS

From the above plots of electronic bands and electronic density of states, $NbTe_2$ is metallic. Phonon bands and phonon density states shows that it is dynamically stable.

5.6.5 Optical properties of $NbTe_2$

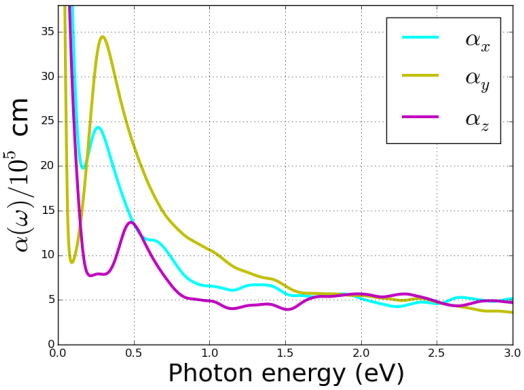


Figure 5.82: $NbTe_2$ absorption coefficient

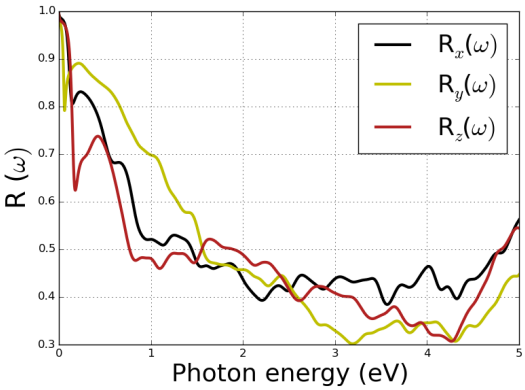


Figure 5.83: $NbTe_2$ reflectivity

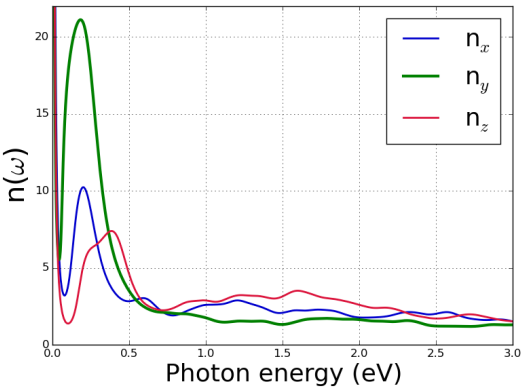


Figure 5.84: $NbTe_2$ refractive index

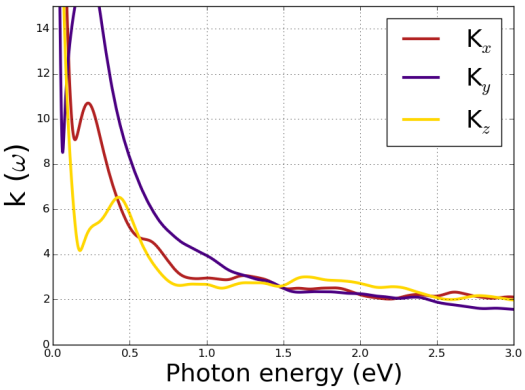


Figure 5.85: $NbTe_2$ extinction coefficient

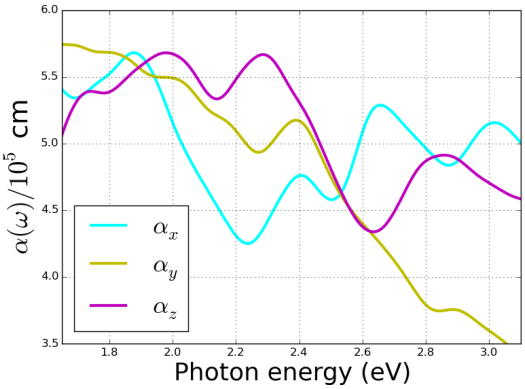


Figure 5.86: Absorption coefficient within the visible range

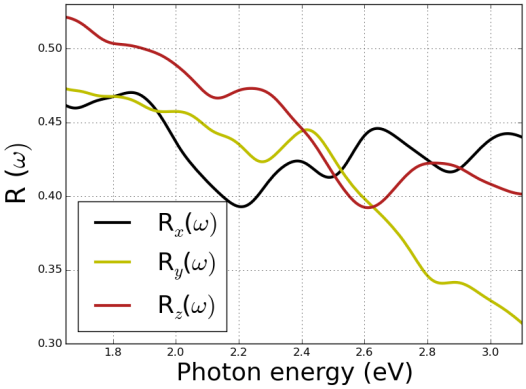


Figure 5.87: Reflectivity within the visible range

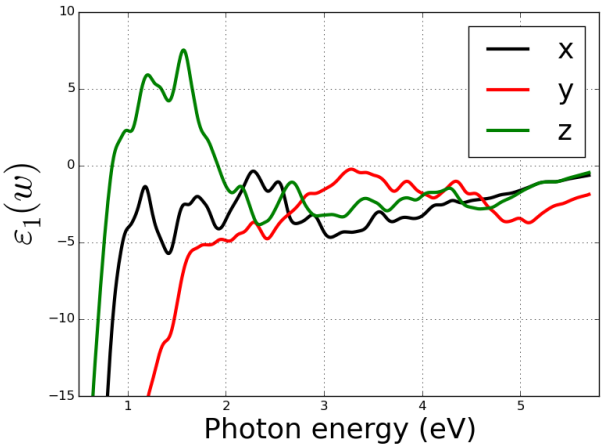


Figure 5.88: Real part of dielectric function

Absorption, reflectivity, refractive index and extinction coefficient shows optical anisotropy and there is no noticeable trend in its optical spectra. Within the visible range, maximum absorption peaks occur at around 1.87 eV, 2.38 eV and 2.30 eV. Hence when light is directed onto $NbTe_2$ in x direction, it will appear red in colour, when directed in y and z directions, it will appear green in colour. Predicted screened plasma frequency in z direction is 0.75 eV and 1.9 eV as given in Figure 5.88 whereas there is no plasma frequency in x and y directions. From the predicted values of screened plasma frequencies, $NbTe_2$ is not an efficient candidate for plasmonic applications since plasmon frequencies occur in the z-axis only partially within the infrared and visible region giving very low plasmon quality.

5.7 Niobium disulphide

For NbS_2, ten polymorphs were considered of which seven were competing.

5.7.1 Relative stability test of NbS_2

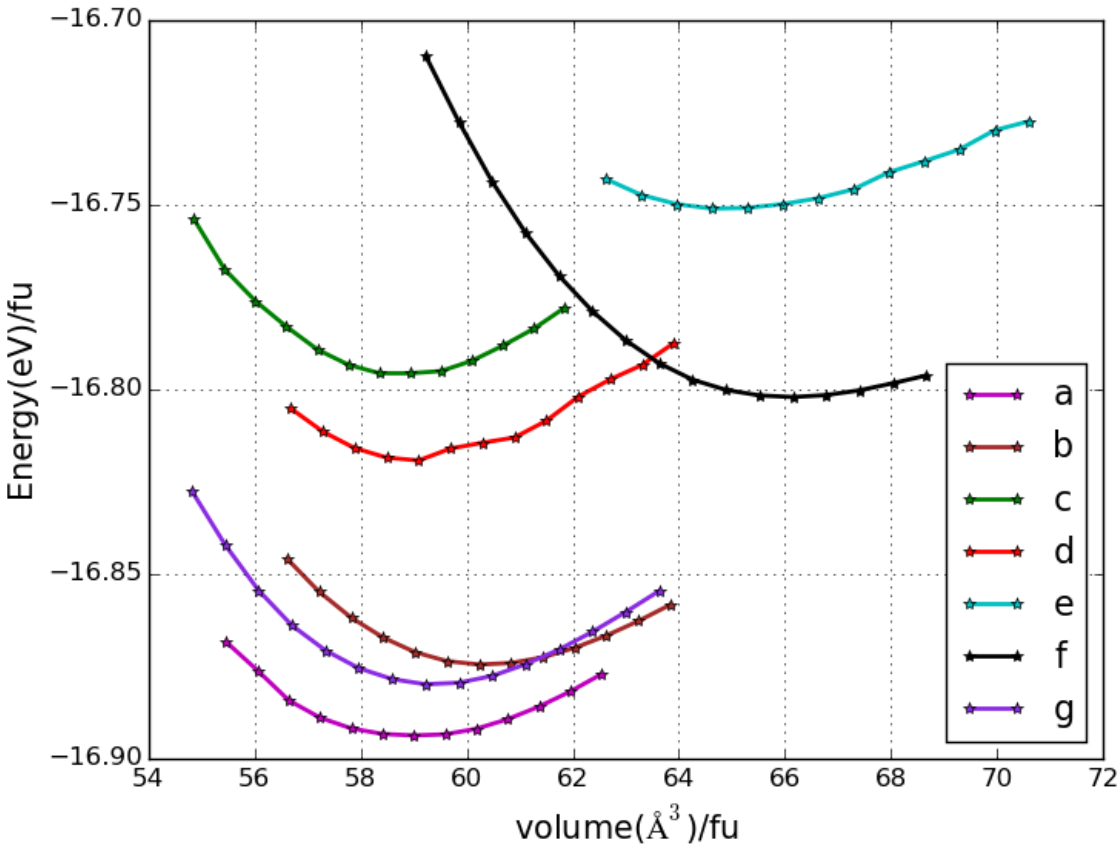


Figure 5.89: Relative stability

Table 5.20: crystal system information

Legend	m.p ID	space group	crystal system
a	10033	$P6_3/mmc$	Hexagonal
b	2648	Fm2m	Orthorhombic
c	554074	$Cmc2_1$	Orthorhombic
d	995122	$P\bar{3}m1$	Trigonal
e	774873	$P6_3/mmc$	Hexagonal
f	1874	$P\bar{6}m2$	Hexagonal
g	966	R3m	Trigonal

Structures of seven candidate polymorphs were optimized to check their relative stability. From the Figure 5.89, hexagonal NbS_2 whose materials project id is 10033 with space group $P6_3/mmc$ was

preferably the most stable polymorph. Since this is not the only parameter used to gauge its overall stability, vibrational and mechanical stability test were further explored for this specific polymorph.

5.7.2 EOS done with various functionals

For preferred ground state structure, structural study was conducted using three functionals as shown underneath.

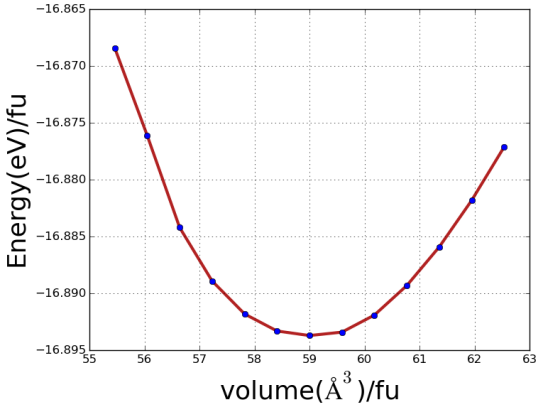


Figure 5.90: PBE+D2

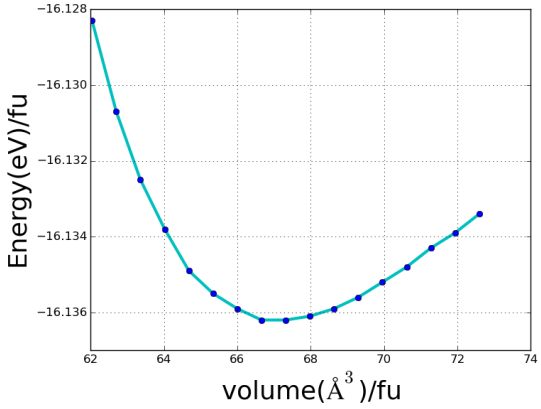


Figure 5.91: PBE

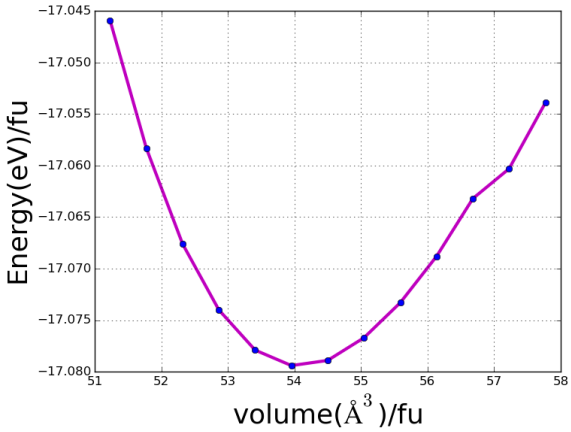


Figure 5.92: PBE+TS

Equilibrium volume obtained when PBE and PBE+TS were used shift towards the right and left of PBE+D2 respectively. Similar trend was observed in their lattice constants.

5.7.3 Structural and energetic properties of NbS_2

Table 5.21: Structural and energetic properties of NbS_2

Functional	a = b (Å)	c (Å)	$\alpha(^\circ)$	$\beta(^\circ)$	$\gamma(^\circ)$	$V_0(Å)^3$	E_{coh}(eV/atom)	E_{form}(eV/atom)	Z
PBE	3.500	12.692	90	90	120	134.64	-5.379	-1.020	2
PBE+D2	3.349	12.146	90	90	120	118.00	-5.631	-1.272	2
PBE+TS	3.251	11.789	90	90	120	107.91	-5.693	-1.334	2
Exp [145]	3.330	12.000	90	90	120	115.24	-	-	2
Exp [146]	3.160	12.290	90	90	120	106.28	-	-	2
Exp [147]	3.418	11.860	90	90	120	120.00	-	-	2
Exp [148]	3.330	11.950	90	90	120	114.76	-	-	2

From numerical data in Table 5.21, PBE+D2 functional mimics well the structural properties of NbS_2 than PBE and PBE+TS. PBE overestimates whereas PBE+TS underestimates as compared to given experimental data. From energies obtained, NbS_2 is energetically stable.

5.7.4 Mechanical properties of NbS_2

Table 5.22: Calculated values of independent elastic coefficients for NbS_2

	C_{11}	C_{12}	C_{13}	C_{33}	C_{44}
PBE	142.970	47.041	1.667	44.491	4.785
PBE+D2	191.890	66.856	11.580	35.924	10.644
PBE+TS	189.140	81.145	22.943	46.233	13.811

From numerical results of elastic coefficients given in Table 5.22, NbS_2 fulfilled all Born stability conditions for hexagonal crystal systems, hence it is mechanically stable.

Table 5.23: Calculated B, E, G, ν and B/G

PBE	B	E	G	ν	B/G
Voight (V)	47.909	74.823	30.178	0.2397	1.58
Reuss (R)	31.023	27.401	10.128	0.3528	3.06
Hill (H)	39.466	51.664	20.153	0.2818	1.96
PBE+D2					
Voight (V)	66.637	97.353	38.739	0.2565	1.72
Reuss (R)	31.755	47.369	18.927	0.2514	1.68
Hill (H)	49.196	72.362	28.833	0.2549	1.71
PBE+TS					
Voight (V)	75.397	93.520	36.156	0.2933	2.08
Reuss (R)	42.230	57.504	22.585	0.2731	1.87
Hill (H)	58.813	75.538	29.371	0.2859	2.00

Three averaging schemes gave B/G values ranging between 1.58 and 3.06 as shown in Table 5.23. This shows that NbS_2 is probably mechanically anisotropic ductile material.

5.7.5 Dynamical and electronic properties of NbS_2

Further study of bands, phonons and optical properties of NbS_2 was done using PBE+D2 since it gave structural data that was much comparable to experimental values.

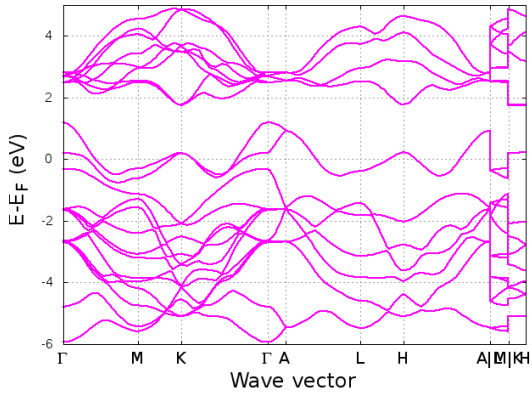


Figure 5.93: NbS_2 electronic Bands

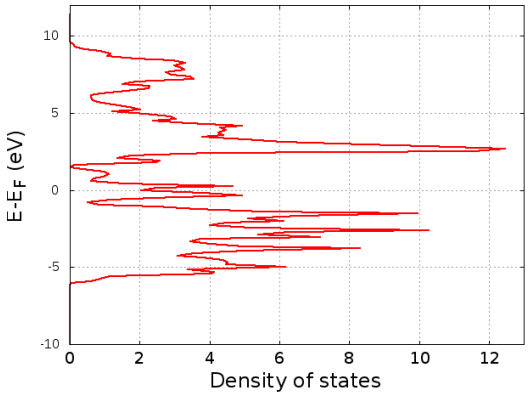


Figure 5.94: Electronic DOS

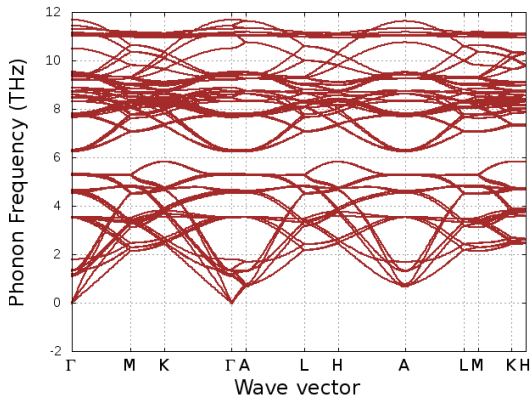


Figure 5.95: NbS_2 phonon Bands

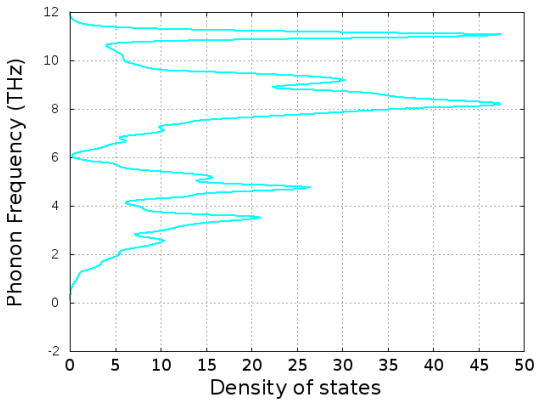


Figure 5.96: Phonon DOS

From Figure 5.93 and Figure 5.94, NbS_2 is metallic in nature. Occurrence of a small gap at about 2 eV above the Fermi level implies that n-doping can be applied to achieve band engineering in NbS_2. Its phonon band structure and phonon density of states depicts that it is dynamically stable as shown in Figure 5.95 and Figure 5.96.

5.7.6 Optical properties of NbS_2

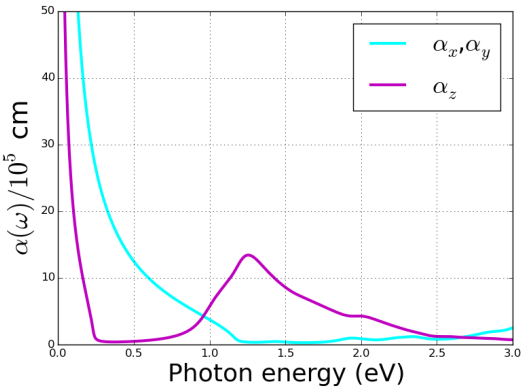


Figure 5.97: NbS_2 absorption coefficient

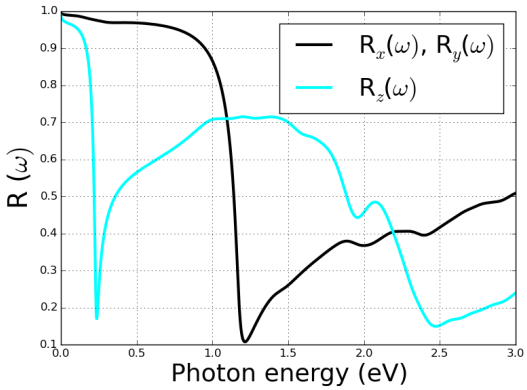


Figure 5.98: NbS_2 reflectivity

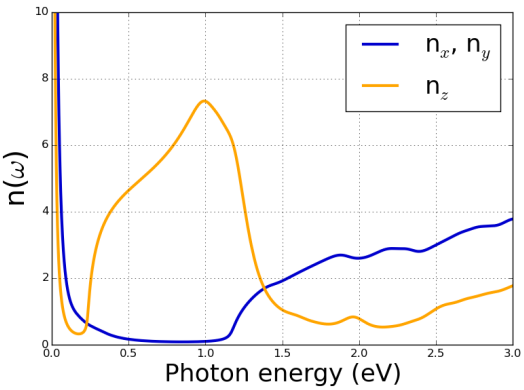


Figure 5.99: NbS_2 refractive index

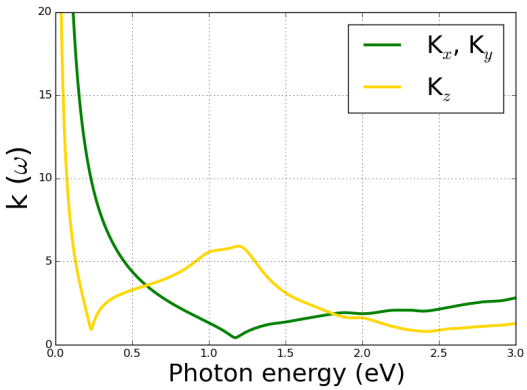


Figure 5.100: NbS_2 extinction coefficient

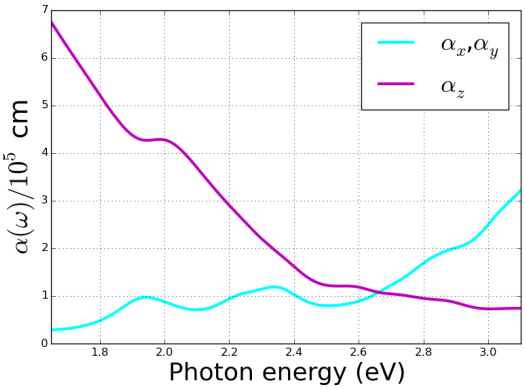


Figure 5.101: Absorption coefficient within the visible range

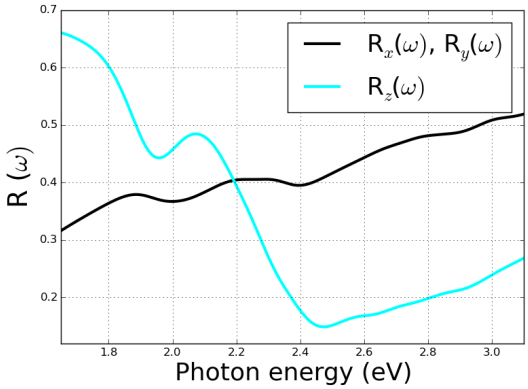


Figure 5.102: Reflectivity within the visible range

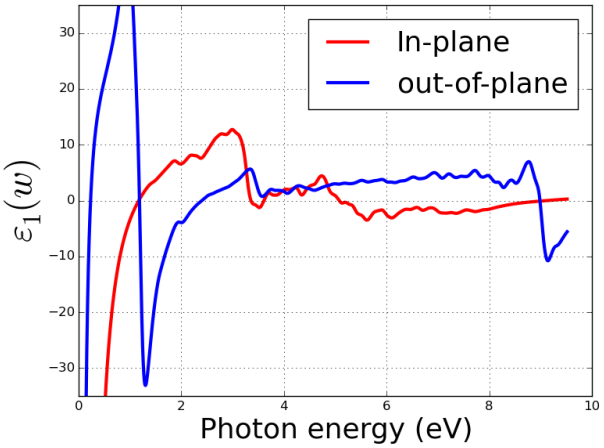


Figure 5.103: Real part of dielectric function

NbS_2 possess some degree of optical isotropy in that behaviour of dielectric function is similar in x and y direction (in-plane) but different for z direction (out-of-plane) which results in identical optical functions in x and y axis. There is no distinct pattern in refractive index and extinction coefficient. Within the visible regime, maximum absorption occur out-of-plane between photon range of 1.65 eV and around 2.63 eV beyond which in-plane absorption exceeds out-of-plane absorption. Between energy range of 1.65 eV and 2.2 eV, maximum reflectivity occur out-of-plane than in-plane beyond which in-plane reflectivity exceeds out-of-plane reflectivity. Within the visible range, wide absorption peaks occur at around 2.0 eV and 2.35 eV for out-of-plane and in-plane respectively. This implies that when incoming photon hits NbS_2 along x and y axis, it will appear orange in colour whereas when it strikes along z axis, it will appear green in colour. Screened in-plane plasma frequency occur at around 1.2 eV, 3.6 eV, 3,8 eV, 5.0 eV and 9.0 eV whereas out-of-plane plasma frequency occur at around 0.3 eV, 1.2 eV, 2.2 eV and 9.0 eV as shown in Figure 5.103. From the predicted values of plasma frequencies, NbS_2 is a promising plasmonic material since plasmon excitations occur in the visible and UV region giving high plasmon quality.

5.8 Niobium diselenide

5.8.1 Relative stability test for $NbSe_2$

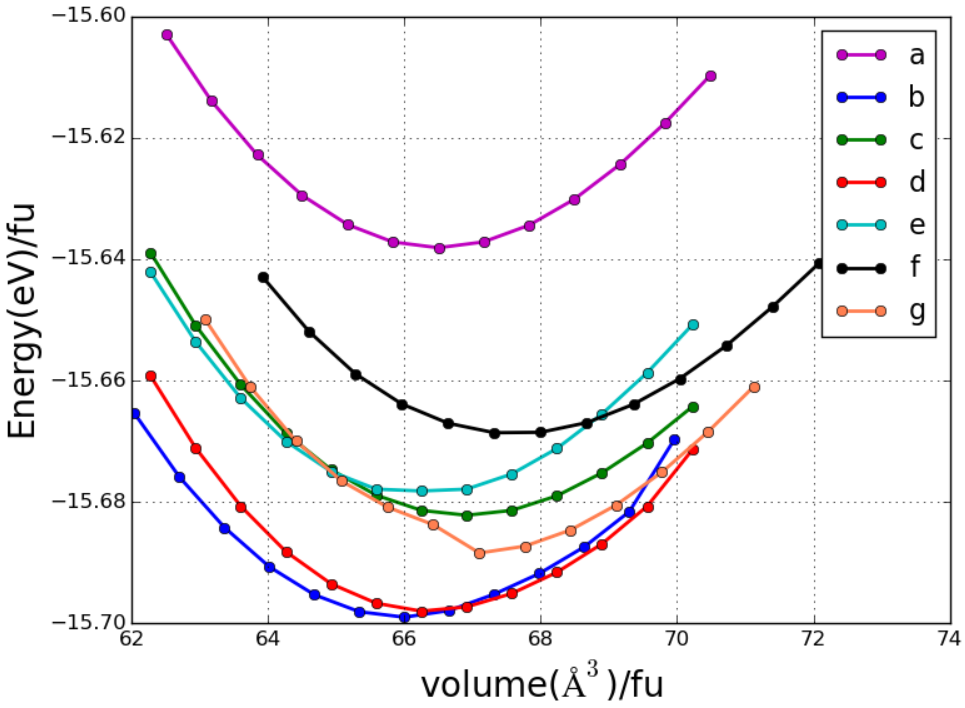


Figure 5.104: Relative stability

Table 5.24: crystal system information

Legend	m.p ID	space group	crystal system
a	10228	$P\bar{3}m1$	Trigonal
b	2207	$P6_3/mmc$	Hexagonal
c	568347	$C222_1$	Orthorhombic
d	571133	$P\bar{6}m2$	Hexagonal
e	571270	$P\bar{6}m2$	Hexagonal
f	7007	Fm2m	Orthorhombic
g	7597	R3m	Trigonal

From Figure 5.104, out of seven competing polymorphs, hexagonal $NbSe_2$ whose materials project id is 2207 and space group $P6_3/mmc$ is the energetically favoured stable structure.

5.8.2 Structural and energetic properties of $NbSe_2$

Table 5.25: Structural and energetic properties of hexagonal $NbSe_2$

Functional	a = b (Å)	c(Å)	$V_0(Å)^3$	$\alpha(°)$	$\beta(°)$	$\gamma(°)$	E_{coh}(eV/atom)	E_{form}(eV/atom)	Z
PBE	3.5120	13.8450	147.89	90	90	120	-5.233	-1.168	2
PBE+TS	3.3110	13.0540	123.94	90	90	120	-5.237	-1.172	2
PBE+D2	3.3810	13.3310	132.00	90	90	120	-4.910	-0.845	2
Exp [149]	3.4425	12.5470	128.77	90	90	120	-	-	2
Exp [150]	3.4446	12.5444	128.90	90	90	120	-	-	2

From predicted structural parameters in Table 5.25, PBE+D2 mimics well $NbSe_2$ in that its numerical values are more comparable to experimental ones than when PBE or PBE+TS are used. It is also energetically stable.

5.8.3 Mechanical properties of $NbSe_2$

Table 5.26: Calculated values of independent elastic coefficients

	C_{11}	C_{12}	C_{13}	C_{33}	C_{44}	C_{66}
PBE	156.010	49.174	14.317	17.585	16.598	53.418
PBE+D2	173.280	56.948	18.992	37.992	21.291	58.164
PBE+TS	138.740	38.520	10.310	18.560	7.400	50.110

From predicted mechanical characteristics given in Table 5.26, $NbSe_2$ is mechanically stable.

Table 5.27: Calculated B, E, G, ν and B/G

PBE	B	E	G	ν	B/G
Voight (V)	53.913	84.507	34.109	0.2388	1.58
Reuss (R)	17.468	42.314	19.299	0.0963	0.91
Hill (H)	35.691	64.121	26.704	0.2006	1.34
PBE+D2					
Voight (V)	63.823	98.145	39.457	0.2437	1.62
Reuss (R)	34.856	67.007	28.403	0.1796	1.23
Hill (H)	49.340	82.807	33.930	0.2203	1.34
PBE+TS					
Voight (V)	46.036	71.441	28.775	0.2414	1.60
Reuss (R)	17.770	30.380	12.501	0.2151	1.42
Hill (H)	31.903	50.932	20.638	0.2339	1.54

For three functionals and averaging schemes, predicted B/G ratio is less than critical value of 1.75, hence $NbSe_2$ is a brittle material.

5.8.4 Dynamical and electronic properties of $NbSe_2$

Electronic band structure, vibrational and optical properties of $NbSe_2$ were carried out using PBE+D2 since it was suitable than other functionals.

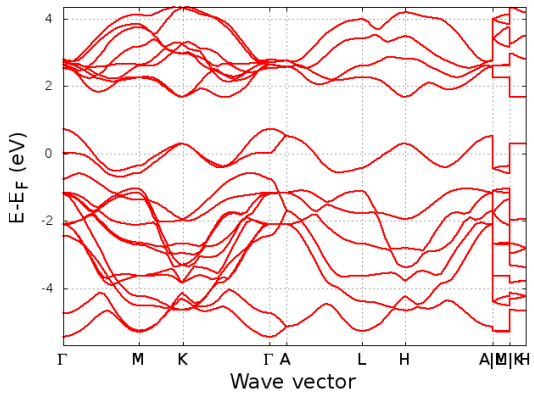


Figure 5.105: $NbSe_2$ electronic Bands

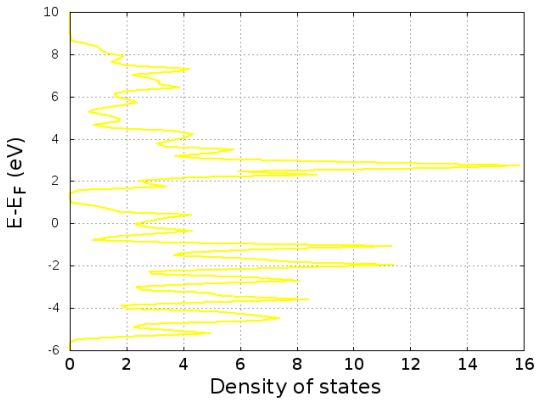


Figure 5.106: Electronic DOS

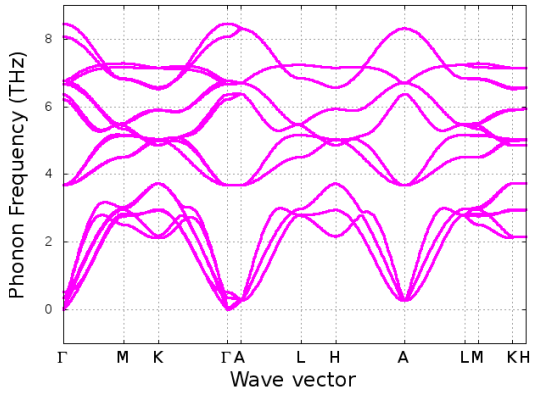


Figure 5.107: $NbSe_2$ phonon Bands

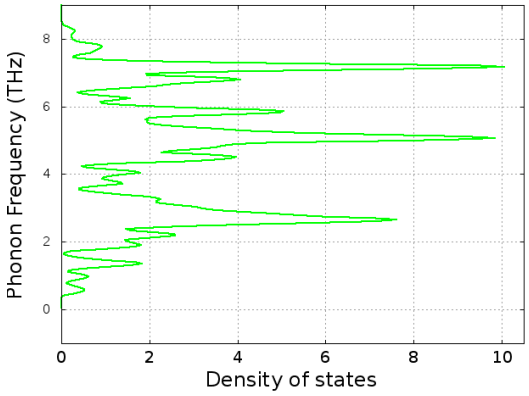


Figure 5.108: Phonon DOS

$NbSe_2$ is metallic as backed by Figure 5.105 and Figure 5.106. Occurrence of a gap at around 1.5 eV above Fermi level shows that possibly, $NbSe_2$ can be doped using donor impurities in order to get n-type semiconductor. Its phonon bands and phonon density of states shows that it is dynamically stable as supported by Figure 5.107 and Figure 5.108.

5.8.5 Optical properties of $NbSe_2$

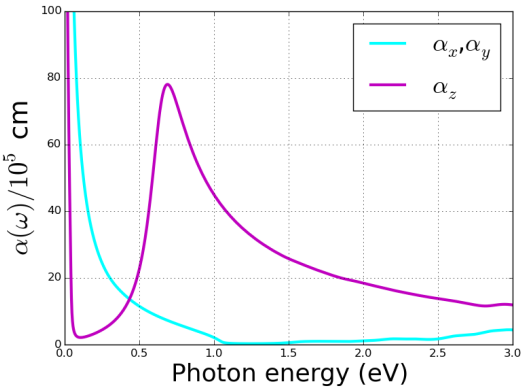


Figure 5.109: $NbSe_2$ absorption coefficient

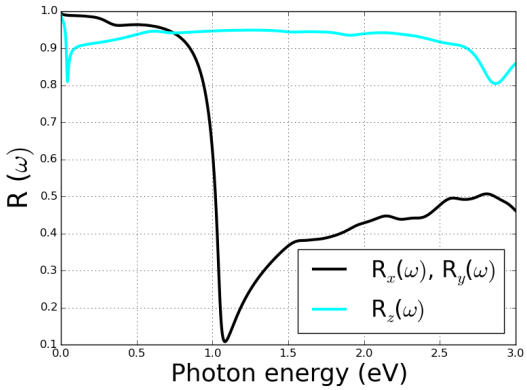


Figure 5.110: $NbSe_2$ reflectivity

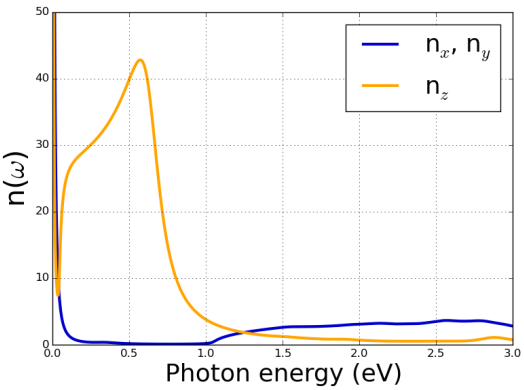


Figure 5.111: $NbSe_2$ refractive index

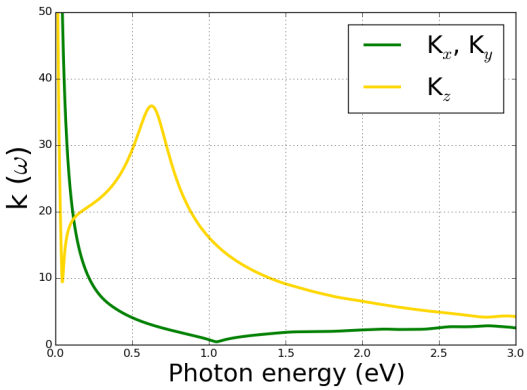


Figure 5.112: $NbSe_2$ extinction coefficient

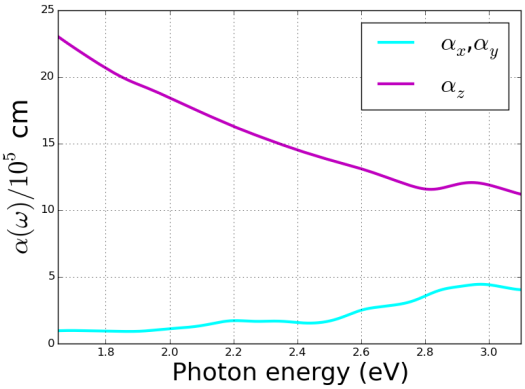


Figure 5.113: Absorption coefficient within the visible range

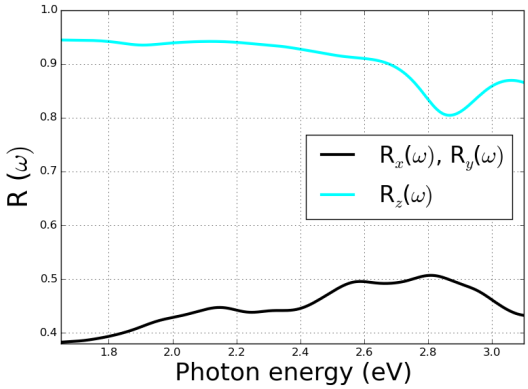


Figure 5.114: Reflectivity within the visible range

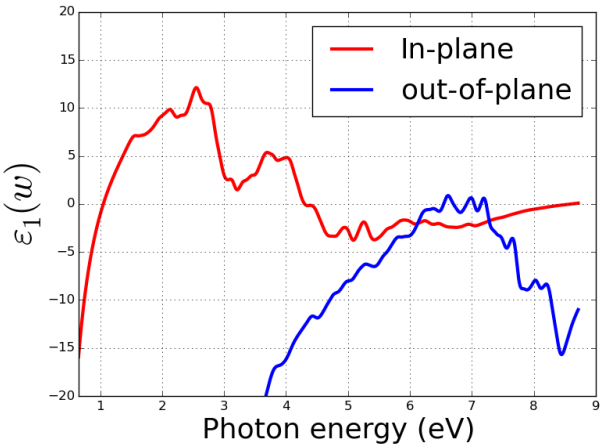


Figure 5.115: Real part of dielectric function

$NbSe_2$ possess similar optical properties to those of NbS_2. Khan *et al* [151] pointed out that for any material, there is no possibility of advancement in photonic devices for optical communication without proper understanding of its optcal properties. For $NbSe_2$, magnitude of in-plane absorption exceeds out-of-plane absorption upto 0.4 eV beyond which out-of-plane dominates. Intensity of in-plane reflectivity exceeds out-of-plane reflectivity upto 0.75 eV beyond which out-of-plane reflectivity exceeds in-plane reflectivity. In-plane refractive index and in-plane extinction coefficient exceeds corresponding out-of-plane counterparts upto around 1.25 eV and 0.2 eV respectively beyond which out-of-plane refractive index and extinction coefficient dominates. Within the visible range, out-of-plane absorption and reflectivity exceeds in-plane ones. Wide absorption peaks occur at the edge of the visible region hence we predict that when $NbSe_2$ is illuminated with light, it will appear violet in colour irrespective of the interface light shines on. Screened in-plane plasma frequency occur at around 1.0 eV, 4.4 eV and 8.5 eV whereas several out-of-plane plasma frequencies were predicted at around 6.5 eV, 6.7 eV, 6.9 eV, 7.1 eV and 7.2 eV. Its screened plasma frequencies occur at infrared and ultraviolet region as shown in Figure 5.115 hence a promising material for plasmonic related applications.

5.9 Summary

This work was intended at exploring structural, electronic, dynamical and optical properties of transition metal dichalcogenides and transition metal dipnictogenides based on first principles investigations using VASP code. Although structural and electronic properties of most materials under this study were previously performed as discussed briefly in chapter 2, analysis of their mechanical, dynamical and optical properties at either ab initio or experimental level are not currently available to the best of our knowledge. This study therefore tries to fill this information gap as well as pave way for further studies.

6

Conclusion and Future work

6.1 Conclusion

We investigated the structural, electronic, mechanical, dynamical and optical properties of transition metal dichalcogenides ($NbSe_2$, NbS_2, $NbTe_2$, VSe_2, VS_2 and VTe_2) as well as transition metal dipnictogenides (NbP_2 and VP_2). For layered transition metal dichalcogenides, PBE+DFT-D2 exchange correlation functional was found to be most appropriate since predicted structural data were comparable to experimental than when other functionals were applied except for $NbTe_2$ where PBEsol was found to mimic its structural properties better. For transition metal dipnictogenides, PBE functional was used with no van der Waals correction since they are non-layered. VP_2, NbP_2, VSe_2 and $NbTe_2$ had only one polymorph that has been exploited experimentally whereas VS_2,NbS_2, VTe_2 and $NbSe_2$ had several competing polymorphs whose energy difference were a few meV per atom as supported by their relative stability plots suggesting that if we subject them to pressure, it may undergo structural phase transition whereby those phases that were unstable at zero pressure may become more relatively stable. For all the compounds considered, phonon dispersion curves had only positive frequencies throughout the Brillouin zone implying that they are dynamically stable. Calculated cohesive and formation energies were all negative implying that the compounds of interest are energetically stable in their ground state against chemical decomposition onto their constituent atoms hence can be easily synthesized. They also fulfilled their respective Born stability conditions hence mechanically stable. Apart from NbS_2 which was found to be anisotropic ductile material, all the others were predicted to be brittle. From their electronic band structure plots, all compounds under this study are metallic in their bulk form. From electronic structure of VSe_2, $NbSe_2$ and NbS_2, band engineering via introduction of donor impurities can aid in obtaining semiconducting compounds which can be applied in designing optoelectronic devices. We predict that $NbSe_2$, NbS_2, VSe_2 and VS_2 are promising plasmonic materials in their bulk form whereas NbP_2, VP_2, $NbTe_2$ and VTe_2 are not.

6.2 Future work

The following questions have to be exploited in future in order to fill the gaps that were beyond the scope of the current study.

1. If bulk crystal of macroscopic dimensions is thinned down to one atomic layer, will monolayers of

layered TMDs studied transform from being metallic to semi-conducting?

2. Can band engineering i.e via application of strain or doping help improve electronic properties of compounds under study?
3. How will their optical spectra behave at their monolayer or bilayer level?

Appendix A

Generalized Hooke's law

Hooke's law is a principle of physics that states that the force needed to stretch or compress a spring is proportional to extension provided the elastic limit is not exceeded. It is a first order linear approximation to real response of spring or other elastic bodies to the applied forces. If the amount of stress is infinitesimally small then the amount of strain, which is also infinitesimal, is linearly proportional to the stress. It is an appropriate approximation for most solid bodies, as long as forces and deformations are small enough. Modern theory of elasticity generalizes Hooke's law to say that strain (deformation) of an elastic material is proportional to applied stress. However, since general stresses and strains may have multiple independent components, the proportionality factor may no longer be valid as just a single real number, but rather a linear map (tensor) that can be represented by a matrix of real numbers. In index notation, the general equation of Hooke's law can be expressed as:

$$\varepsilon_{ij} = S_{ijkl}\sigma_{kl} \tag{.0.1}$$

where ε_{ij} is the strain tensor, S_{ijkl} is forth order compliance tensor and σ_{kl} the stress tensor. For anisotropic materials, Cauchy's postulate can be applied which states that every component of the stress tensor is coupled linearly with every component of strain tensor which can then be expressed in matrix form as [152, 153];

$$\begin{bmatrix} \varepsilon_{11} \\ \varepsilon_{22} \\ \varepsilon_{33} \\ \varepsilon_{23} \\ \varepsilon_{13} \\ \varepsilon_{12} \\ \varepsilon_{32} \\ \varepsilon_{31} \\ \varepsilon_{21} \end{bmatrix} = \begin{bmatrix} S_{1111} & S_{1122} & S_{1133} & S_{1123} & S_{1113} & S_{1112} & S_{1132} & S_{1131} & S_{1121} \\ S_{2211} & S_{2222} & S_{2233} & S_{2223} & S_{2213} & S_{2212} & S_{2232} & S_{2231} & S_{2221} \\ S_{3311} & S_{3322} & S_{3333} & S_{3323} & S_{3313} & S_{3312} & S_{3332} & S_{3331} & S_{3321} \\ S_{2311} & S_{2322} & S_{2333} & S_{2323} & S_{2313} & S_{2312} & S_{2332} & S_{2331} & S_{2321} \\ S_{1311} & S_{1322} & S_{1333} & S_{1323} & S_{1313} & S_{1312} & S_{1332} & S_{1331} & S_{1321} \\ S_{1211} & S_{1222} & S_{1233} & S_{1223} & S_{1213} & S_{1212} & S_{1232} & S_{1231} & S_{1221} \\ S_{3211} & S_{3222} & S_{3233} & S_{3223} & S_{3213} & S_{3212} & S_{3232} & S_{3231} & S_{3221} \\ S_{3111} & S_{3122} & S_{3133} & S_{3123} & S_{3113} & S_{3112} & S_{3132} & S_{3131} & S_{3121} \\ S_{2111} & S_{2122} & S_{2133} & S_{2123} & S_{2113} & S_{2112} & S_{2132} & S_{2131} & S_{2121} \end{bmatrix} \begin{bmatrix} \sigma_{11} \\ \sigma_{22} \\ \sigma_{33} \\ \sigma_{23} \\ \sigma_{13} \\ \sigma_{12} \\ \sigma_{32} \\ \sigma_{31} \\ \sigma_{21} \end{bmatrix} \tag{.0.2}$$

Normally, to characterize a given homogenous system we need the above 81 independent compliance coefficients. If we invert the above equation, we obtain;

$$\begin{bmatrix} \sigma_{11} \\ \sigma_{22} \\ \sigma_{33} \\ \sigma_{23} \\ \sigma_{13} \\ \sigma_{12} \\ \sigma_{32} \\ \sigma_{31} \\ \sigma_{21} \end{bmatrix} = \begin{bmatrix} C_{1111} & C_{1122} & C_{1133} & C_{1123} & C_{1113} & C_{1112} & C_{1132} & C_{1131} & C_{1121} \\ C_{2211} & C_{2222} & C_{2233} & C_{2223} & C_{2213} & C_{2212} & C_{2232} & C_{2231} & C_{2221} \\ C_{3311} & C_{3322} & C_{3333} & C_{3323} & C_{3313} & C_{3312} & C_{3332} & C_{3331} & C_{3321} \\ C_{2311} & C_{2322} & C_{2333} & C_{2323} & C_{2313} & C_{2312} & C_{2332} & C_{2331} & C_{2321} \\ C_{1311} & C_{1322} & C_{1333} & C_{1323} & C_{1313} & C_{1312} & C_{1332} & C_{1331} & C_{1321} \\ C_{1211} & C_{1222} & S_{1233} & C_{1223} & C_{1213} & C_{1212} & C_{1232} & C_{1231} & C_{1221} \\ C_{3211} & C_{3222} & C_{3233} & C_{3223} & C_{3213} & C_{3212} & C_{3232} & C_{3231} & C_{3221} \\ C_{3111} & C_{3122} & C_{3133} & C_{3123} & C_{3113} & C_{3112} & C_{3132} & C_{3131} & C_{3121} \\ C_{2111} & C_{2122} & C_{2133} & C_{2123} & C_{2113} & C_{2112} & C_{2132} & C_{2131} & C_{2121} \end{bmatrix} \begin{bmatrix} \varepsilon_{11} \\ \varepsilon_{22} \\ \varepsilon_{33} \\ \varepsilon_{23} \\ \varepsilon_{13} \\ \varepsilon_{12} \\ \varepsilon_{32} \\ \varepsilon_{31} \\ \varepsilon_{21} \end{bmatrix} \tag{.0.3}$$

This equation can be expressed in index notation as;

$$\sigma_{ij} = C_{ijkl}\varepsilon_{kl} \tag{.0.4}$$

C_{ijkl} are components of elasticity/stiffness tensor. For anisotropic materials, the symmetry of the Cauchy stress tensor ($\sigma_{ij} = \sigma_{ji}$) and the generalized Hooke's law $\sigma_{ij} = C_{ijkl}\ \varepsilon_{kl}$ implies that $C_{ijkl} = C_{jikl}$. Similarly, the symmetry of infinitesimal strain tensor implies that $C_{ijkl} = C_{ijlk}$. These symmetries are called the minor symetries of stiffness tensor. All these conditions reduces the number of elastic constants from 81 to 36.

$$\begin{bmatrix} \sigma_{11} \\ \sigma_{22} \\ \sigma_{33} \\ \sigma_{23} \\ \sigma_{13} \\ \sigma_{12} \end{bmatrix} = \begin{bmatrix} C_{1111} & C_{1122} & C_{1133} & C_{1123} & C_{1113} & C_{1112} \\ C_{2211} & C_{2222} & C_{2233} & C_{2223} & C_{2213} & C_{2212} \\ C_{3311} & C_{3322} & C_{3333} & C_{3323} & C_{3313} & C_{3312} \\ C_{2311} & C_{2322} & C_{2333} & C_{2323} & C_{2313} & C_{2312} \\ C_{1311} & C_{1322} & C_{1333} & C_{1323} & C_{1313} & C_{1312} \\ C_{1211} & C_{1222} & S_{1233} & C_{1223} & C_{1213} & C_{1212} \end{bmatrix} \begin{bmatrix} \varepsilon_{11} \\ \varepsilon_{22} \\ \varepsilon_{33} \\ \varepsilon_{23} \\ \varepsilon_{13} \\ \varepsilon_{12} \end{bmatrix} \tag{.0.5}$$

The relationship of shear components ij = ji reduces it further. In principle, we can see that the six diagonal components in reduced 6 x 6 matrix are related to the normal stress and strains. It is customary to use Voigt notation in order to reduce the number of indices. $11 \mapsto 1, 22 \mapsto 2, 33 \mapsto 3, 23 \mapsto 4, 13 \mapsto 5, 12 \mapsto 6$. The remaining 30 components can be divided by two (due to shear relationship). Thus, 6+15 components of the original matrix results to 21 independent components of the compliance matrix for anisotropic materials. This results in 21 independent elastic constants [154, 155].

$$C_{ij} = \begin{pmatrix} C_{11} & C_{12} & C_{13} & C_{14} & C_{15} & C_{16} \\ & C_{22} & C_{23} & C_{24} & C_{25} & C_{26} \\ & & C_{33} & C_{34} & C_{35} & C_{36} \\ & Symmetric & & C_{44} & C_{45} & C_{46} \\ & & & & C_{55} & C_{56} \\ & & & & & C_{66} \end{pmatrix} \tag{.0.6}$$

Born stability criteria in various crystal systems

These conditions varies from one crystal system to another. The following table gives information about each crystal system with their respective point groups and Born stability conditions [136, 156].

crystal system	no of independent EC_s	point groups	mechanical stability criteria
Cubic	3	432, $\bar{4}$3m, m$\bar{3}$m,23,m$\bar{3}$	$C_{11} - C_{12} > 0; C_{44} > 0; C_{11} + 2C_{12} > 0$ (.0.7)
Hexagonal and Tetragonal (I)	5	6mm, 622,$\bar{6}$2m,6/mmm,6,$\bar{6}$,6/m	$C_{11} >\mid C_{12} \mid; C_{44} > 0; C_{66} > 0; 2C_{13}^2 < C_{33}(C_{11} + C_{12})$ (.0.8)
Tetragonal (II)	6	4,$\bar{4}$,4/m	$C_{11} >\mid C_{12} \mid; C_{44} > 0; 2C_{13}^2 < C_{33}(C_{11} + C_{12}); 2C_{16}^2 < C_{66}(C_{11} - C_{12})$ (.0.9)
Rhombohedral (I)	6	32,3m,$\bar{3}$m	$C_{11} >\mid C_{12} \mid; C_{44} > 0; C_{14}^2 < \frac{1}{2}C_{44}(C_{11} - C_{12}) = C_{44}C_{66}; C_{13}^2 < \frac{1}{2}C_{33}(C_{11} + C_{12})$ (.0.10)
Rhombohedral (II)	7	3,$\bar{3}$	$C_{11} >\mid C_{12} \mid; C_{44} > 0; C_{14}^2 + C_{15}^2 < \frac{1}{2}C_{44}(C_{11} - C_{12}) = C_{44}C_{66}; C_{13}^2 < \frac{1}{2}C_{33}(C_{11} + C_{12})$ (.0.11)
Orthorhombic	9	2mm, mmm, 222	$C_{11} > 0; C_{11}C_{22} > C_{12}^2; C_{11}C_{22}C_{33} + 2C_{12}C_{13}C_{23} - C_{11}C_{23}^2 - C_{22}C_{13}^2 - C_{33}C_{12}^2 > 0;$ $C_{44} > 0; C_{55} > 0; C_{66} > 0$ (.0.12)
Monoclinic	13	2/m	$C_{11} > 0; C_{22} > 0; C_{33} > 0; C_{44} > 0; C_{55} > 0; C_{66} > 0; (C_{33}C_{55} - C_{35}^2) > 0;$ $(C_{44}C_{66} - C_{46}^2) > 0; (C_{22} + C_{33} - 2C_{23}) > 0;$ $[C_{11} + C_{22} + C_{33} + 2(C_{12} + C_{13}C_{23})] > 0;$ $[C_{22}(C_{33}C_{55} - C_{35}^2 + 2C_{23}C_{25}C_{35} - C_{23}^2C_{55} - C_{25}^2C_{33}] > 0;$ $\{2[C_{15}C_{25}(C_{33}C_{12} - C_{13}C_{23}) + C_{15}C_{35}(C_{22}C_{13} - C_{12}C_{23})$ $+C_{25}C_{35}(C_{11}C_{23} - C_{12}C_{13})] - [C_{15}^2(C_{22}C_{23} - C_{23}^2)$ $+C_{25}^2(C_{11}C_{33} - C_{13}^2) + C_{35}^2(C_{11}C_{22} - C_{12}^2)] + C_{55}g\} > 0$ *where* g $= C_{11}C_{22}C_{33} - C_{11}C_{23}^2 - C_{22}C_{13}^2$ $-C_{33}C_{12}^2 + 2C_{12}C_{13}C_{23}$ (.0.13)

Voight, Reuss and Hill Averaging schemes

Basically Voight method assumes a uniform strain giving values that are often upper limit numerical data whereas Reuss method assumes a uniform stress giving lower limit numerical data. On the other hand, Hill method is an average between the Voight and Reuss [157, 158]. Voight bulk and shear moduli are given by;

$$B_V = \frac{2}{9}[C_{11} + C_{12} + 2C_{13} + \frac{1}{2}C_{33}] \tag{.0.14}$$

$$G_V = \frac{1}{30}[C_{11} + C_{12} + 2C_{33} - 4C_{13} + 12C_{55} + 12C_{66}] \tag{.0.15}$$

Reuss bulk and shear modulus are given by;

$$B_R = \frac{\left[5C_{55}C_{66}(C_{11} + C_{12})C_{33} - 2C_{12}^2\right]}{C_{11} + C_{12} + 2C_{33} - 4C_{12}} \tag{.0.16}$$

$$G_R = \frac{\left[5C_{55}C_{66}(C_{11} + C_{12})C_{33} - 2C_{12}^2\right]}{2\{3B_VC_{55}C_{66} + \left[(C_{11} + C_{12})C_{33} - 2C_{12}^2\right](C_{55} + C_{66})\}} \tag{.0.17}$$

Hill bulk and shear modulus are given by;

$$B_H = \frac{1}{2}(B_V + B_R) \tag{.0.18}$$

$$G_H = \frac{1}{2}(G_V + G_R) \tag{.0.19}$$

Materials project

This is a scientific online database that provide material researchers with information i.e band structures, elastic tensors, piezzo-electric tensors among other properties for inorganic compounds, nanoporous materials, molecules, intercalation electrons, conversion electrodes etc. It also provides ICSD (Inorganic Crystal Structure Database) number which can be used to access existing experimental data of a material of choice since each has unique number. In this study, input files were obtained from materials project whereas POTCAR files were generated using Python Materials Genomics (pymatgen) [159].

Appendix B

Eigenvalues of the stiffness matrix

Table 1: Calculated eigenvalues in Gpa obtained from elastic constants calculation for all compounds considered in this study

Compound	Functional	λ_1	λ_2	λ_3	λ_4	λ_5	λ_6
NbP_2	PBE	83.184	105.500	158.480	180.580	265.140	496.440
VP_2	PBE	108.190	113.930	162.560	204.510	281.010	473.210
NbS_2	PBE	4.785	4.785	44.453	47.965	95.930	190.050
	PBE+TS	13.811	13.811	41.629	53.998	108.000	274.890
	PBE+D2	10.644	10.644	34.727	62.515	125.030	259.940
VS_2	PBE	5.727	5.727	15.056	60.635	121.270	260.880
	PBE+TS	5.105	5.105	5.628	57.938	115.880	248.190
	PBE+D2	4.181	4.181	4.448	58.824	117.650	257.940
$NbSe_2$	PBE	15.424	16.598	16.598	53.418	106.840	207.340
	PBE+TS	7.400	7.400	17.226	50.110	100.220	178.590
	PBE+D2	21.291	21.291	34.310	58.164	116.330	233.910
VSe_2	PBE	1.456	1.456	3.972	42.790	85.579	123.560
	PBE+TS	2.8658	2.8662	9.862	42.151	84.289	114.740
	PBE+D2	17.410	17.629	49.472	56.856	112.290	164.830
$NbTe_2$	PBE	9.813	10.469	18.112	41.570	70.236	119.970
	PBE+TS	7.252	7.612	9.370	41.305	68.097	106.83
	PBE+D2	11.935	14.394	31.957	47.613	76.597	142.270
	PBEsol	6.877	9.571	16.148	42.057	67.100	115.310
VTe_2	PBE	7.214	7.682	20.582	37.953	73.338	110.450
	PBE+TS	4.965	6.801	11.464	39.050	70.834	100.490
	PBE+D2	7.609	13.048	36.664	41.135	74.828	116.500
	PBEsol	5.458	7.606	12.851	37.194	71.550	114.530

Drude term

Table 2: convergence of Drude plasma frequency squared with respect to k-points at DFT level in various directions

Compound	x-axis	y-axis	z-axis	k-points	k-point density
NbP_2	1.679	0.241	2.762	10 10 5	18000
VP_2	0.788	0.341	1.007	10 10 4	14000
VSe_2	16.095	16.095	2.954	16 16 7	16000
$NbSe_2$	10.077	10.077	1.558	12 12 3	14000
NbS_2	11.104	11.104	1.271	12 12 3	14000
VS_2	9.776	9.776	0.003	12 12 2	10000
$NbTe_2$	5.220	1.701	2.624	8 8 3	14000
VTe_2	5.866	1.101	1.697	7 7 3	10000

References

[1] A. C. Neto, F. Guinea, N. Peres, K. S. Novoselov, and A. K. Geim, "The electronic properties of graphene," *Reviews of Modern Physics*, vol. 81, no. 1, p. 109, 2009.

[2] M. Katsnelson and M. Iosifovich, *Graphene: Carbon in two dimensions*. Cambridge University Press, 2012.

[3] P. Zhu, B. G. Sumpter, and V. Meunier, "Electronic, thermal, and structural properties of graphene oxide frameworks," *The Journal of Physical Chemistry C*, vol. 117, no. 16, pp. 8276–8281, 2013.

[4] J.-N. Fuchs and M. Oliver, "Introduction to the physical properties of graphene," *Lecture Notes*, 2008.

[5] Y. Wu, P. Ye, M. A. Capano, Y. Xuan, Y. Sui, M. Qi, and J. A. Cooper, "Top-gated graphene field-effect-transistors formed by decomposition of SiC," *arXiv preprint arXiv:0802.4103*, 2008.

[6] B. Radisavljevic, A. Radenovic, J. Brivio, V. Giacometti, and A. Kis, "Single-layer MoS_2 transistors," *Nature Nanotechnology*, vol. 6, no. 3, pp. 147–150, 2011.

[7] W. Koch, M. C. Holthausen, and M. C. Holthausen, *A Chemist's guide to density functional theory*, vol. 2. Wiley-Vch Weinheim, 2001.

[8] C. Geantet, J. Afonso, M. Breysse, N. Allali, and M. Danot, "Niobium sulfides as catalysts for hydrotreating reactions," *Catalysis today*, vol. 28, no. 1, pp. 23–30, 1996.

[9] N. Kumagai and K. Tanno, "Kinetic and structural characteristics of 3R-niobium disulfide as a positive material for secondary lithium batteries," *Electrochimica acta*, vol. 36, no. 5, pp. 935–941, 1991.

[10] W. Ge, K. Kawahara, M. Tsuji, and H. Ago, "Large-scale synthesis of NbS_2 nanosheets with controlled orientation on graphene by ambient pressure CVD," *Nanoscale*, vol. 5, no. 13, pp. 5773–5778, 2013.

[11] W. Divigalpitiya, R. Frindt, and S. Morrison, "Effect of humidity on spread NbS_2 films," *Journal of Physics D: Applied Physics*, vol. 23, no. 7, p. 966, 1990.

[12] F. Gillot, M. Ménétrier, E. Bekaert, L. Dupont, M. Morcrette, L. Monconduit, and J.-M. Tarascon, "Vanadium diphosphides as negative electrodes for secondary Li-ion batteries," *Journal of Power Sources*, vol. 172, no. 2, pp. 877–885, 2007.

[13] D. J. Late, C. S. Rout, D. Chakravarty, and S. Ratha, "Emerging energy applications of two-dimensional layered materials,"

[14] L. Ponomarenko, F. Schedin, M. Katsnelson, R. Yang, E. Hill, K. Novoselov, and A. Geim, "Chaotic dirac billiard in graphene quantum dots," *Science*, vol. 320, no. 5874, pp. 356–358, 2008.

[15] X. Wang, X. Li, L. Zhang, Y. Yoon, P. K. Weber, H. Wang, J. Guo, and H. Dai, "N-doping of graphene through electrothermal reactions with ammonia," *Science*, vol. 324, no. 5928, pp. 768–771, 2009.

[16] X. Wang, L. Zhi, and K. Müllen, "Transparent, conductive graphene electrodes for dye-sensitized solar cells," *Nano Letters*, vol. 8, no. 1, pp. 323–327, 2008.

[17] P. D. Fleischauer and R. Bauer, "Chemical and structural effects on the lubrication properties of sputtered MoS_2 films," *Tribology Transactions*, vol. 31, no. 2, pp. 239–250, 1988.

[18] M. Chhowalla, H. S. Shin, G. Eda, L.-J. Li, K. P. Loh, and H. Zhang, "The chemistry of two-dimensional layered transition metal dichalcogenide nanosheets," *Nature chemistry*, vol. 5, no. 4, pp. 263–275, 2013.

[19] K. F. Mak, C. Lee, J. Hone, J. Shan, and T. F. Heinz, "Atomically thin MoS_2: a new direct-gap semiconductor," *Physical Review Letters*, vol. 105, no. 13, p. 136805, 2010.

[20] H. Wang and Y. H. Hu, "Graphene as a counter electrode material for dye-sensitized solar cells," *Energy & Environmental Science*, vol. 5, no. 8, pp. 8182–8188, 2012.

[21] T. Cao, G. Wang, W. Han, H. Ye, C. Zhu, J. Shi, Q. Niu, P. Tan, E. Wang, and B. Liu, "Valley-selective circular dichroism of monolayer molybdenum disulphide," *Nature Communications*, vol. 3, p. 887, 2012.

[22] A. Kormányos, V. Zólyomi, N. D. Drummond, and G. Burkard, "Spin-orbit coupling, quantum dots, and qubits in monolayer transition metal dichalcogenides," *Physical Review X*, vol. 4, no. 1, p. 011034, 2014.

[23] T. Sekine, C. Julien, I. Samaras, M. Jouanne, and M. Balkanski, "Vibrational modifications on lithium intercalation in MoS_2," *Materials Science and Engineering: B*, vol. 3, no. 1-2, pp. 153–158, 1989.

[24] A. Kuc and T. Heine, "The electronic structure calculations of two-dimensional transition-metal dichalcogenides in the presence of external electric and magnetic fields," *Chemical Society Reviews*, vol. 44, no. 9, pp. 2603–2614, 2015.

[25] A.-J. Cho, K. C. Park, and J.-Y. Kwon, "A high-performance complementary inverter based on transition metal dichalcogenide field-effect transistors," *Nanoscale Research Letters*, vol. 10, no. 1, pp. 1–6, 2015.

[26] X. Chia, A. Y. S. Eng, A. Ambrosi, S. M. Tan, and M. Pumera, "Electrochemistry of nanostructured layered transition-metal dichalcogenides," *Chemical reviews*, vol. 115, no. 21, pp. 11941–11966, 2015.

[27] D. Voiry, A. Mohite, and M. Chhowalla, "Phase engineering of transition metal dichalcogenides," *Chemical Society reviews*, vol. 44, no. 9, pp. 2702–2712, 2015.

[28] N. R. Bandaru, "Structure and optical properties of transition metal dichalcogenides (TMDs)–MX_2 (M= Mo, W & X= S, Se) under high pressure and high temperature conditions," 2015.

[29] X. Luo, X. Lu, C. Cong, T. Yu, Q. Xiong, and S. Y. Quek, "Stacking sequence determines raman intensities of observed interlayer shear modes in 2D layered materials–a general bond polarizability model," *Scientific reports*, vol. 5, 2015.

[30] J. Wilson and A. Yoffe, "The transition metal dichalcogenides discussion and interpretation of the observed optical, electrical and structural properties," *Advances in Physics*, vol. 18, no. 73, pp. 193–335, 1969.

[31] A. D. Yoffe, "Electronic properties of two dimensional solids: The layer type transition metal dichalcogenides," in *Festkörperprobleme 13*, pp. 1–29, Springer, 1973.

[32] R. Lieth, *Preparation and crystal growth of materials with layered structures*, vol. 1. Springer Science & Business Media, 1977.

[33] A. Balchin, "Growth and the crystal characteristics of dichalcogenides having layer structures," in *Crystallography and Crystal Chemistry of Materials with Layered Structures*, pp. 1–50, Springer, 1976.

[34] F. Lévy and Y. Froidevaux, "Structural and electrical properties of layered transition metal selenides $V_xTi_{1-x}Se_2$ and $Ta_xTi_{1-x}Se_2$," *Journal of Physics C: Solid State Physics*, vol. 12, no. 3, p. 473, 1979.

[35] H. F, "New representatives of the $NbAs_2$ and $ZrAs_2$ structures," *Nature*, vol. 204, p. 775, 1964.

[36] M. Zumbusch and B. W, "Anorg. allg.," *chem*, vol. 249, no. 1, 1942.

[37] M. Gglin, B. Carlsson, and S. Rundqvist, "Refinement of the crystal structure of VP_2," *Acta Chem. Scand. A*, vol. 29, no. 7, 1975.

[38] G. Wiegers, "Physical properties of first-row transition metal dichalcogenides and their intercalates," *Physica B+ C*, vol. 99, no. 1, pp. 151–165, 1980.

[39] K. Bronsema, G. Bus, and G. Wiegers, "The crystal structure of vanadium ditelluride, $V_{1+x}Te_2$," *Journal of Solid State Chemistry*, vol. 53, no. 3, pp. 415–421, 1984.

[40] D. W. Murphy, C. Cros, F. J. Di Salvo, and J. Waszczak, "Preparation and properties of Li_xVS_2 ($0 \leq x \leq 1$)," *Inorganic Chemistry*, vol. 16, no. 12, pp. 3027–3031, 1977.

[41] H. Zhang, L.-M. Liu, and W.-M. Lau, "Dimension-dependent phase transition and magnetic properties of VS_2," *Journal of Materials Chemistry A*, vol. 1, no. 36, pp. 10821–10828, 2013.

[42] C. Song, K. Yu, H. Yin, H. Fu, Z. Zhang, N. Zhang, and Z. Zhu, "Highly efficient field emission properties of a novel layered VS_2/ZnO nanocomposite and flexible VS_2 nanosheet," *Journal of Materials Chemistry C*, vol. 2, no. 21, pp. 4196–4202, 2014.

[43] J. Feng, L. Peng, C. Wu, X. Sun, S. Hu, C. Lin, J. Dai, J. Yang, and Y. Xie, "Giant moisture responsiveness of VS_2 ultrathin nanosheets for novel touchless positioning interface," *Advanced materials*, vol. 24, no. 15, pp. 1969–1974, 2012.

[44] W. G. Fisher and M. Sienko, "Stoichiometry, structure, and physical properties of niobium disulfide," *Inorganic Chemistry*, vol. 19, no. 1, pp. 39–43, 1980.

[45] R. Nitsche, H. Bölsterli, and M. Lichtensteiger, "Crystal growth by chemical transport reactions-I: Binary, ternary, and mixed-crystal chalcogenides," *Journal of Physics and Chemistry of Solids*, vol. 21, no. 3-4, pp. 199–205, 1961.

[46] N. Bhatt, R. Vaidya, S. Patel, and A. Jani, "X-ray diffraction studies of $NbTe_2$ single crystal," *Bulletin of Materials Science*, vol. 27, no. 1, pp. 23–25, 2004.

[47] J. Van Landuyt, G. Van Tendeloo, and S. Amelinckx, "Electron diffraction study of inter-and intrapolytypic phase transitions in transition metal dichalcogenides.III. Complementary diffraction studies and lattice imaging of the deformation waves," *physica status solidi (a)*, vol. 36, no. 2, pp. 757–777, 1976.

[48] S. Nagata, T. Abe, S. Ebisu, Y. Ishihara, and K. Tsutsumi, "Superconductivity in the metallic layered compound $NbTe_2$," *Journal of Physics and Chemistry of Solids*, vol. 54, no. 8, pp. 895–899, 1993.

[49] H. Erdogan and R. D. Kirby, "Raman spectrum and lattice dynamics of $NbTe_2$," *Solid state communications*, vol. 70, no. 7, pp. 713–715, 1989.

[50] R. Kershaw, M. Vlasse, and A. Wold, "The preparation of and electrical properties of niobium selenide and tungsten selenide," *Inorganic Chemistry*, vol. 6, no. 8, pp. 1599–1602, 1967.

[51] E. Revolinsky, G. Spiering, and D. Beerntsen, "Superconductivity in the niobium-selenium system," *Journal of Physics and Chemistry of Solids*, vol. 26, no. 6, pp. 1029–1034, 1965.

[52] D. Huntley and R. Frindt, "Transport properties of $NbSe_2$," *Canadian Journal of Physics*, vol. 52, no. 10, pp. 861–867, 1974.

[53] F. Gamble, J. H. Osiecki, and F. DiSalvo, "Some superconducting intercalation complexes of TaS_2 and substituted pyridines," *The Journal of Chemical Physics*, vol. 55, no. 7, pp. 3525–3530, 1971.

[54] R. Schöllhorn, H. Zagefka, T. Butz, and A. Lerf, "Ionic bonding model of the pyridine intercalation compounds of layered transition metal dichalcogenides," *Materials Research Bulletin*, vol. 14, no. 3, pp. 369–376, 1979.

[55] H. Lee, H. McKinzie, D. Tannhauser, and A. Wold, "The low-temperature transport properties of $NbSe_2$," *Journal of Applied Physics*, vol. 40, no. 2, pp. 602–604, 1969.

[56] D. Jerome, A. Grant, and A. Yoffe, "Pressure enhanced superconductivity in $NbSe_2$," *Solid State Communications*, vol. 9, no. 24, pp. 2183–2185, 1971.

[57] R. M. Martin, *Electronic structure: Basic theory and practical methods*. Cambridge University Press, 2004.

[58] P. Hohenberg and W. Kohn, "Inhomogeneous electron gas," *Physical Review*, vol. 136, no. 3B, p. B864, 1964.

[59] D. Sholl and J. A. Steckel, *Density functional theory: a practical introduction*. John Wiley & Sons, 2011.

[60] V. Sahni, "Derivation and reinterpretation of approximations in Schrödinger and Kohn-Sham theory via a hierarchy within the work formalism," *International Journal of Quantum Chemistry*, vol. 53, no. 6, pp. 591–606, 1995.

[61] K. Burke and L. Wagner, "ABC of ground-state DFT," 2014.

[62] C. Fiolhais, F. Nogueira, and M. A. Marques, *A primer in density functional theory*, vol. 620. Springer Science & Business Media, 2003.

[63] X.-M. Tong and S.-I. Chu, "Density-functional theory with optimized effective potential and self-interaction correction for ground states and autoionizing resonances," *Physical Review A*, vol. 55, no. 5, p. 3406, 1997.

[64] K. Capelle, "A bird's-eye view of density-functional theory," *Brazilian Journal of Physics*, vol. 36, no. 4A, pp. 1318–1343, 2006.

[65] W. Johnson, S. Blundell, and J. Sapirstein, "Many-body perturbation-theory calculations of energy levels along the lithium isoelectronic sequence," *Physical Review A*, vol. 37, no. 8, p. 2764, 1988.

[66] J. Inkson and D. Ter Haar, "Many-body theory of solids: An introduction," *Physics Today*, vol. 38, no. 5, pp. 85–86, 2008.

[67] G. Teschl, *Mathematical methods in Quantum Mechanics*, vol. 157. American Mathematical Society, 2014.

[68] A. Seidl, A. Görling, P. Vogl, J. Majewski, and M. Levy, "Generalized Kohn-Sham schemes and the band-gap problem," *Physical Review B*, vol. 53, no. 7, p. 3764, 1996.

[69] C. Adamo, M. Ernzerhof, and G. E. Scuseria, "The meta-gga functional: Thermochemistry with a kinetic energy density dependent exchange-correlation functional," *The Journal of Chemical Physics*, vol. 112, no. 6, pp. 2643–2649, 2000.

[70] F. Tran and P. Blaha, "Accurate band gaps of semiconductors and insulators with a semilocal exchange-correlation potential," *Physical review letters*, vol. 102, no. 22, p. 226401, 2009.

[71] C. J. Cramer and F. Bickelhaupt, "Essentials of computational chemistry," *ANGEWANDTE CHEMIE-INTERNATIONAL EDITION IN ENGLISH-*, vol. 42, no. 4, pp. 381–381, 2003.

[72] V. N. Staroverov, "Density-functional approximations for exchange and correlation," *A Matter of Density: Exploring the Electron Density Concept in the Chemical, Biological, and Materials Sciences*, pp. 125–156, 2012.

[73] C. D. Sherrill, "The Born-Oppenheimer approximation," *School of Chemistry and Biochemistry, Georgia Institute of Technology*, 2005.

[74] J. P. Perdew, K. Burke, and Y. Wang, "Generalized gradient approximation for the exchange-correlation hole of a many-electron system," *Physical Review B*, vol. 54, no. 23, p. 16533, 1996.

[75] V. Brosco, Z.-J. Ying, and J. Lorenzana, "Exact exchange-correlation potential of an ionic hubbard model with a free surface," *Scientific Reports*, vol. 3, 2013.

[76] T. Bučko, S. Lebègue, J. Hafner, and J. Ángyán, "Tkatchenko-Scheffler van der Waals correction method with and without self-consistent screening applied to solids," *Physical Review B*, vol. 87, no. 6, p. 064110, 2013.

[77] S. Grimme, "Semiempirical GGA-type density functional constructed with a long-range dispersion correction," *Journal of computational chemistry*, vol. 27, no. 15, pp. 1787–1799, 2006.

[78] S. Refaely-Abramson, R. Baer, and L. Kronik, "Fundamental and excitation gaps in molecules of relevance for organic photovoltaics from an optimally tuned range-separated hybrid functional," *Physical Review B*, vol. 84, no. 7, p. 075144, 2011.

[79] E. Baerends, O. Gritsenko, and R. Van Meer, "The Kohn–Sham gap, the fundamental gap and the optical gap: the physical meaning of occupied and virtual Kohn-Sham orbital energies," *Physical Chemistry Chemical Physics*, vol. 15, no. 39, pp. 16408–16425, 2013.

[80] M. Ashbaugh, "The fundamental gap," in *Workshop on Low Eigenvalues of Laplace and Schrödinger Operators, American Institute of Mathematics, Palo Alto, California*, 2006.

[81] C. Friedrich and A. Schindlmayr, "Many-body perturbation theory: The GW approximation," *NIC Series*, vol. 31, p. 335, 2006.

[82] F. Aryasetiawan and O. Gunnarsson, "The GW method," *Reports on Progress in Physics*, vol. 61, no. 3, p. 237, 1998.

[83] L. Hedin, "New method for calculating the one-particle green's function with application to the electron-gas problem," *Physical Review*, vol. 139, no. 3A, p. A796, 1965.

[84] W. Hittinger, "Solid state physics: Advances in research & applications, vol. 16," *Proceedings of the IEEE*, vol. 53, no. 11, pp. 1811–1811, 1965.

[85] F. Bruneval, F. Sottile, V. Olevano, R. Del Sole, and L. Reining, "Many-body perturbation theory using the density-functional concept: Beyond the GW approximation," *Physical Review Letters*, vol. 94, no. 18, p. 186402, 2005.

[86] L. Hedin, A. Johansson, B. Lundqvist, S. Lundqvist, and V. Samathiyakanit, "Effects of electron-electron interaction on the one-electron properties of atoms and solids," tech. rep., Inst. of Theoretical Physics, Goteborg, 1969.

[87] C.-M. Liegener, "Derivation of Rowe's renormalized random phase approximation from the Bethe-Salpeter Equation," *Physics Letters A*, vol. 85, no. 6, pp. 324–326, 1981.

[88] T. Sander, E. Maggio, and G. Kresse, "Beyond the Tamm-Dancoff approximation for extended systems using exact diagonalization," *Physical Review B*, vol. 92, no. 4, p. 045209, 2015.

[89] L. Khriachtchev, *Silicon Nanophotonics: Basic Principles, Current Status and Perspectives*. Pan Stanford Publishing, 2009.

[90] A. S. Blazev, *Photovoltaics for commercial and utilities power generation*. Lulu Press, Inc, 2013.

[91] A. Srivani, V. R. Murthy, and G. V. Raghavaiah, "Research in physical properties of $Al_xGa_{1-x}As$ III-V Arsenide ternary semiconductor alloys," *International Journal of Physical Sciences*, vol. 9, no. 12, pp. 281–291, 2014.

[92] J. Kim, S.-H. Jhi, and K. R. Lee, "Color of TiN and ZrN from first-principles calculations," *Journal of Applied Physics*, vol. 110, no. 8, p. 083501, 2011.

[93] F. Mehmood, R. Pachter, N. R. Murphy, and W. E. Johnson, "Electronic and optical properties of titanium nitride bulk and surfaces from first principles calculations," *Journal of Applied Physics*, vol. 118, no. 19, p. 195302, 2015.

[94] M. J. van Setten, S. Er, G. Brocks, R. A. de Groot, and G. A. de Wijs, "First-principles study of the optical properties of $Mg_xTi_{1-x}H_2$," *Physical Review B*, vol. 79, no. 12, p. 125117, 2009.

[95] S. A. Maier, *Plasmonics: fundamentals and applications*. Springer Science & Business Media, 2007.

[96] D. K. Gramotnev and S. I. Bozhevolnyi, "Plasmonics beyond the diffraction limit," *Nature photonics*, vol. 4, no. 2, pp. 83–91, 2010.

[97] E. Ozbay, "Plasmonics: merging photonics and electronics at nanoscale dimensions," *science*, vol. 311, no. 5758, pp. 189–193, 2006.

[98] W. A. Murray and W. L. Barnes, "Plasmonic materials," *Advanced materials*, vol. 19, no. 22, pp. 3771–3782, 2007.

[99] M. G. Blaber, M. D. Arnold, and M. J. Ford, "A review of the optical properties of alloys and intermetallics for plasmonics," *Journal of Physics: Condensed Matter*, vol. 22, no. 14, p. 143201, 2010.

[100] H. A. Atwater, "The promise of plasmonics," *Scientific American*, vol. 296, no. 4, pp. 56–62, 2007.

[101] M. Dresselhaus, "Solid state physics part II optical properties of solids," 1999.

[102] D. B. Tanner, "Optical effects in solids," *Department of Physics, University of Florida, USA*, 2013.

[103] P. R. West, S. Ishii, G. V. Naik, N. K. Emani, V. M. Shalaev, and A. Boltasseva, "Searching for better plasmonic materials," *Laser & Photonics Reviews*, vol. 4, no. 6, pp. 795–808, 2010.

[104] G. V. Naik, V. M. Shalaev, and A. Boltasseva, "Alternative plasmonic materials: beyond gold and silver," *Advanced Materials*, vol. 25, no. 24, pp. 3264–3294, 2013.

[105] M. Blaber, M. Arnold, and M. Ford, "Optical properties of intermetallic compounds from first principles calculations: a search for the ideal plasmonic material," *Journal of Physics: Condensed Matter*, vol. 21, no. 14, p. 144211, 2009.

[106] M. D. Arnold and M. G. Blaber, "Optical performance and metallic absorption in nanoplasmonic systems," *Optics express*, vol. 17, no. 5, pp. 3835–3847, 2009.

[107] J. Hafner, "Ab-initio simulations of materials using VASP: Density-functional theory and beyond," *Journal of Computational Chemistry*, vol. 29, no. 13, pp. 2044–2078, 2008.

[108] Z. Wu and R. E. Cohen, "More accurate generalized gradient approximation for solids," *Physical Review B*, vol. 73, no. 23, p. 235116, 2006.

[109] I. Štich, R. Car, M. Parrinello, and S. Baroni, "Conjugate gradient minimization of the energy functional: A new method for electronic structure calculation," *Physical Review B*, vol. 39, no. 8, p. 4997, 1989.

[110] T. Bučko, S. Lebègue, J. G. Ángyán, and J. Hafner, "Extending the applicability of the Tkatchenko-Scheffler dispersion correction via iterative hirshfeld partitioning," *The Journal of chemical physics*, vol. 141, no. 3, p. 034114, 2014.

[111] Z.-L. Liu, L.-C. Cai, and X.-L. Zhang, "Novel high pressure structures and superconductivity of niobium disulfide," *Journal of Alloys and Compounds*, vol. 610, pp. 472–477, 2014.

[112] A. Togo, F. Oba, and I. Tanaka, "First-principles calculations of the ferroelastic transition between rutile-type and $CaCl_2$-type SiO_2 at high pressures," *Physical Review B*, vol. 78, no. 13, p. 134106, 2008.

[113] G. Kresse and J. Hafner, "Ab initio molecular dynamics for liquid metals," *Physical Review B*, vol. 47, no. 1, p. 558, 1993.

[114] G. Kresse and J. Furthmüller, "Efficiency of ab-initio total energy calculations for metals and semiconductors using a plane-wave basis set," *Computational Materials Science*, vol. 6, no. 1, pp. 15–50, 1996.

[115] G. Kresse and D. Joubert, "From ultrasoft pseudopotentials to the projector augmented-wave method," *Physical Review B*, vol. 59, no. 3, p. 1758, 1999.

[116] S. P. Ong, W. D. Richards, A. Jain, G. Hautier, M. Kocher, S. Cholia, D. Gunter, V. L. Chevrier, K. A. Persson, and G. Ceder, "Python materials genomics (pymatgen): A robust, open-source python library for materials analysis," *Computational Materials Science*, vol. 68, pp. 314–319, 2013.

[117] T. Bučko, J. Hafner, and J. G. Ángyán, "Geometry optimization of periodic systems using internal coordinates," *The Journal of Chemical Physics*, vol. 122, no. 12, p. 124508, 2005.

[118] R. E. Cohen, O. Gülseren, and R. J. Hemley, "Accuracy of equation-of-state formulations," *American Mineralogist*, vol. 85, no. 2, pp. 338–344, 2000.

[119] A. U. Ortiz, A. Boutin, A. H. Fuchs, and F.-X. Coudert, "Metal-organic frameworks with wine-rack motif:what determines their flexibility and elastic properties?," *The Journal of chemical physics*, vol. 138, no. 17, p. 174703, 2013.

[120] V. Lucarini, J. J. Saarinen, K.-E. Peiponen, and E. M. Vartiainen, *Kramers-Kronig relations in optical materials research*, vol. 110. Springer Science & Business Media, 2005.

[121] J. D. Pack and H. J. Monkhorst, ""special points for brillouin-zone integrations"—a reply," *Physical Review B*, vol. 16, no. 4, p. 1748, 1977.

[122] H. J. Monkhorst and J. D. Pack, "Special points for brillouin-zone integrations," *Physical review B*, vol. 13, no. 12, p. 5188, 1976.

[123] J. Paier, M. Marsman, K. Hummer, G. Kresse, I. C. Gerber, and J. G. Ángyán, "Screened hybrid density functionals applied to solids," *The Journal of chemical physics*, vol. 124, no. 15, p. 154709, 2006.

[124] J. Garai, "Universal equation of states are derived from the isothermal relationships of elastic solids," *arXiv preprint arXiv:0804.2929*, 2008.

[125] C. Kittel, *Introduction to solid state physics*. Wiley, 2005.

[126] J. Garai, "Semi-empirical pressure-volume-temperature equation of state; $MgSiO_3$ perovskite is an example," *arXiv preprint arXiv:0706.0291*, 2007.

[127] R. J. B. Balaguru and B. Jeyaprakash, "Lattice vibrations, phonons, specific heat capacity, thermal conductivity,"

[128] G. Ackland, M. Warren, and S. Clark, "Practical methods in ab initio lattice dynamics," *Journal of Physics: Condensed Matter*, vol. 9, no. 37, p. 7861, 1997.

[129] A. Togo and I. Tanaka, "First principles phonon calculations in materials science," *Scripta Materialia*, vol. 108, pp. 1–5, 2015.

[130] L. Chaput, A. Togo, I. Tanaka, and G. Hug, "Phonon-phonon interactions in transition metals," *Physical Review B*, vol. 84, no. 9, p. 094302, 2011.

[131] C. *et al*, "AFLOW: an automatic framework for high-throughput materials discovery," *Computational Materials Science*, vol. 58, pp. 218–226, 2012.

[132] R. Ahmed, S. J. Hashemifar, H. Akbarzadeh, M. Ahmed, *et al.*, "Ab initio study of structural and electronic properties of III-arsenide binary compounds," *Computational materials science*, vol. 39, no. 3, pp. 580–586, 2007.

[133] Y. Li, L. Zhang, T. Cui, Y. Li, Y. Wang, Y. Ma, and G. Zou, "First-principles studies of phonon instabilities in AgI under high pressure," *Journal of Physics: Condensed Matter*, vol. 20, no. 19, p. 195218, 2008.

[134] D. Terzopoulos, J. Platt, and K. Fleischer, "Heating and melting deformable models," *The Journal of Visualization and Computer Animation*, vol. 2, no. 2, pp. 68–73, 1991.

[135] M. J. Mehl, B. M. Klein, D. A. Papaconstantopoulos, *et al.*, *First principles calculations of elastic properties of metals*, vol. 1. Citeseer, 1994.

[136] F. Mouhat and F.-X. Coudert, "Necessary and sufficient elastic stability conditions in various crystal systems," *Physical Review B*, vol. 90, no. 22, p. 224104, 2014.

[137] J. Sun, H.-T. Wang, J. He, and Y. Tian, "Ab initio investigations of optical properties of the high-pressure phases of ZnO," *Physical Review B*, vol. 71, no. 12, p. 125132, 2005.

[138] A. Gültekin, M. K. Öztürk, M. Tamer, Y. Baş, and S. Özçelik, "The study of structural, electronic, elastic and optical properties in $Be_{1-x}Zn_xSe$ alloys," *Gazi University Journal of Science*, vol. 28, no. 4, pp. 577–586, 2015.

[139] S. Yu, R. D. Schmidt, R. Garcia-Mendez, E. Herbert, N. J. Dudney, J. B. Wolfenstine, J. Sakamoto, and D. J. Siegel, "Elastic properties of the solid electrolyte $Li_7La_3Zr_2O_{12}$ (LLZO)," *Chemistry of Materials*, vol. 28, no. 1, pp. 197–206, 2015.

[140] L. Qi-Jun, Z. Ning-Chao, L. Fu-Sheng, and L. Zheng-Tang, "Structural, electronic, optical, elastic properties and born effective charges of monoclinic HfO_2 from first-principles calculations," *Chinese Physics B*, vol. 23, no. 4, p. 047101, 2014.

[141] S. Pugh, "XCII. relations between the elastic moduli and the plastic properties of polycrystalline pure metals," *The London, Edinburgh, and Dublin Philosophical Magazine and Journal of Science*, vol. 45, no. 367, pp. 823–843, 1954.

[142] M. G. Blaber, M. D. Arnold, and M. J. Ford, "Designing materials for plasmonic systems," *arXiv preprint arXiv:0908.3707*, 2009.

[143] J. Pendry, A. Holden, W. Stewart, and I. Youngs, "Extremely low frequency plasmons in metallic mesostructures," *Physical review letters*, vol. 76, no. 25, p. 4773, 1996.

[144] K. Hayashi and M. Nakahira, "Stability and the equilibrium selenium vapor pressure of the VSe_2 phase," *Journal of Solid State Chemistry*, vol. 24, no. 2, pp. 153–161, 1978.

[145] B. Pfalzgraf, H. Spreckels, W. Paulus, and R. Schollhorn, "Order-disorder phase transition in layered $Cu_{1/2}NbS_2$ observed by electrical resistivity measurements," *Journal of Physics F: Metal Physics*, vol. 17, no. 4, p. 857, 1987.

[146] F. Jellinek, G. Brauer, and H. Müller, "Molybdenum and niobium sulphides," 1960.

[147] C. J. Carmalt, E. S. Peters, I. P. Parkin, T. D. Manning, and A. L. Hector, "Chemical vapor deposition of niobium disulfide thin films," *European Journal of Inorganic Chemistry*, vol. 2004, no. 22, pp. 4470–4476, 2004.

[148] M. Leroux, M. Le Tacon, M. Calandra, L. Cario, M. A. Measson, P. Diener, E. Borrissenko, A. Bosak, and P. Rodiere, "Anharmonic suppression of charge density waves in 2H-NbS_2," *Physical Review B*, vol. 86, no. 15, p. 155125, 2012.

[149] A. Meerschaut and C. Deudon, "Crystal structure studies of the 3R-$Nb_{1.09}$ S_2 and the 2H-$NbSe_2$ compounds: correlation between nonstoichiometry and stacking type (= polytypism)," *Materials Research Bulletin*, vol. 36, no. 9, pp. 1721–1727, 2001.

[150] M. Marezio, P. Dernier, A. Menth, and G. Hull, "The crystal structure of $NbSe_2$ at 15 k," *Journal of Solid State Chemistry*, vol. 4, no. 3, pp. 425–429, 1972.

[151] S. A. Khan and A. Reshak, "First principle study of electronic structure, chemical bonding and optical properties of 5-azido-1H-tetrazole," *Int. J. Electrochem. Sci*, vol. 8, pp. 9459–9473, 2013.

[152] E. N. Glass and J. Winicour, "A geometric generalization of Hooke's law," *Journal of Mathematical Physics*, vol. 14, no. 9, pp. 1285–1290, 1973.

[153] M. P. Nemeth, "An in-depth tutorial on constitutive equations for elastic anisotropic materials," 2011.

[154] E. Menéndez-Proupin, S. Cervantes-Rodríguez, R. Osorio-Pulgar, M. Franco-Cisterna, H. Camacho-Montes, and M. Fuentes, "Computer simulation of elastic constants of hydroxyapatite and fluorapatite," *Journal of the Mechanical Behavior of Biomedical Materials*, vol. 4, no. 7, pp. 1011–1020, 2011.

[155] C. Jiang, S. Srinivasan, A. Caro, and S. Maloy, "Structural, elastic, and electronic properties of Fe_3C from first principles," *Journal of Applied Physics*, vol. 103, no. 4, p. 043502, 2008.

[156] Z.-j. Wu, E.-j. Zhao, H.-p. Xiang, X.-f. Hao, X.-j. Liu, and J. Meng, "Crystal structures and elastic properties of superhard IrN_2 and $IrN_3$from first principles," *Physical Review B*, vol. 76, no. 5, p. 054115, 2007.

[157] I. R. Shein and A. L. Ivanovskii, "Elastic properties of mono-and polycrystalline hexagonal AlB_2-like diborides of s, p and d metals from first-principles calculations," *Journal of Physics: Condensed Matter*, vol. 20, no. 41, p. 415218, 2008.

[158] W. Ching, P. Rulis, and A. Misra, "Ab initio elastic properties and tensile strength of crystalline hydroxyapatite," *Acta Biomaterialia*, vol. 5, no. 8, pp. 3067–3075, 2009.

[159] A. Jain, S. P. Ong, G. Hautier, W. Chen, W. D. Richards, S. Dacek, S. Cholia, D. Gunter, D. Skinner, G. Ceder, and K. a. Persson, "The Materials Project: A materials genome approach to accelerating materials innovation," *APL Materials*, vol. 1, no. 1, p. 011002, 2013.